SCUOLA DI DOTTORATO

UNIVERSITÀ DEGLI STUDI DI MILANO-BICOCCA

Dipartimento di / Department of

Scienza dei Materiali

Dottorato di Ricerca in / PhD program Scienza e Nanotecnologia dei Materiali Ciclo /Cycle XXXII

Functional Porous Materials: Tailored Adsorption Properties, Flexibility and Advanced Optical Applications

Cognome / Surname Perego Nome / Name Jacopo

Matricola / Registration number 728719

Tutore / Tutor: Prof.ssa Angiolina Comotti

Coordinatore / Coordinator: Prof. Marco Bernasconi

ANNO ACCADEMICO / ACADEMIC YEAR 2018/2019

1. Thesis highlights

1.1. Thesis moltivation

In the last 20 years researches about novel classes of microporous materials flourished. At first, the unprecedented available surface areas and pore sizes boosted researches towards the development of effective and selective adsorbents that can be scaled up to meet the requirements of industrial processes. Today, the principles that govern adsorption processes in ultra-high surface area materials are well understood and the technological transfer from university laboratories to real-world applications seems impending. Along with the improvement of adsorptive properties, the outstanding synthetic versatility of microporous materials allow engineering advanced properties and functions that are not even displayed by "traditional" materials.

This Ph.D. thesis has two main focuses.

1. Understanding gas adsorption processes and developing materials with tailored properties for gas capture and separation or gas storage.

2. Developing the design, synthesis and characterization of different porous materials that can accomplish advanced tasks and display peculiar properties thank to a proper design at the molecular level.

1.2. Results

Chapter 3 illustrates the synthesis and the measurements of adsorption properties towards CO_2 and CH_4 of a family of triphenylmethane-based porous organic polymers (TPAFs). The sorptive properties are modulated by the functional group installed on the central carbon atom. Specifically, aliphatic amines improve the interactions with carbon dioxide resulting in an isosteric heat of adsorption as high as 54 kJ/mol at low loadings. 2D ^{1}H –^{13}C heterocorrelated solid state MAS NMR spectroscopy provides

clear evidences of the close-contact interactions between amines and CO_2 guest molecules. CH_4 interacts strongly with the polar hydroxyl groups on pore walls at pressure up to 10 bar and room temperature and the generation of lithium alkoxyde moieties inside the structure increases the isosteric heat of adsorption up to 25 kJ/mol.

Chapter 4 deals with metal organic frameworks built up by bicyclo [1.1.1] pentane-1,3-dicarboxylic acid (BCP). Two metal organic frameworks have been synthetized with the organic struts bicyclo [1.1.1] pentane-1,3-dicarboxylic acid (BCP) and zinc or zirconium ions, ZnBCP and ZrBCP, respectively. These materials have been extensively characterized from a chemical and structural point of view. Different properties have been studied:

- Adsorptive properties. CO_2 adsorption is strongly affected by the different structures of ZnBCP and ZrBCP.
- Thermal properties and solid state reactivity. The inclusion of BCP moieties in a solid skeleton allows the observation of a thermally activated reaction.

Chapter 5 develops the theme of soft or flexible metal organic frameworks (FMOFs) and their complex behavior under gas stimuli. This work has been partially conducted during a period (6 months) spent at Bernal Institute, university of Limerick, Ireland under the guidance of Prof. M. J. Zaworotko. A flexible MOF has been synthesized ($Zn_2(TPA)_2$(bpAN); TPA = terephtalic acid; bpAN = 1,2 *bis*(4-pyridyl) acrylonitrile). It shows a two-fold interpenetrated **pcu** network generated by square lattice layers of dinuclear Zn(II) tetracarboxylate paddlewheels linked by terephtalic acid and pillared by bpAN moieties along c axis. Upon solvent removal, the solid undergoes a phase transition to a close phase driven by the coordination isomerism of Zn(II) cations. Surprisingly, low pressures (70 mbar) of CO_2 at 195 K triggers a close to open phase transition and generates a switching adsorption isotherm. Functionalized terephtalic acid can be exploited to control the switching threshold pressure for CO_2 and even suppress or enable the phase transition with other gases. Further measurements and analyses are still ongoing to clarify the phase change mechanism: understanding these

dynamical phenomena can be valuable to develop materials for gas storage and stimuli-responsive solids.

In chapter 6 optically emitting porous aromatic frameworks (*e*PAF) for triplet-triplet annihilation up-conversion (sTTA-UC) have been developed. Porous aromatic frameworks have been synthesized from rigid pore generating tetraphenylmethane (TPM) monomers and highly luminescent diphenylanthracene moieties (DPA). The three dimensional networks display high porosity and preserve the optical properties of the DPA unit, providing highly luminescent nanoparticles. Thus, ePAF nanoparticles have been tested as annihilator for sTTA up-conversion by suspending the nanoparticles with the triplet sensitizer platinum octaethylporphyrin (PtOEP) in deoxygenated benzene. Porphyrin molecules can diffuse within the porous structure and sensitize the up-conversion process with an effective energy transfer towards the DPA molecules (emitters). Under optical excitation of the porphyrin moiety at 532 nm the upconverted emission generated from DPA can be detected at 430 nm even at low powers and a record conversion efficiency of 15% in a covalently linked framework of emitters is achieved. Moreover, thank to the high accessibility of the internal surface area, a post-synthetic reaction between an emitting porous aromatic framework bearing hydroxyl functional groups (*e*PEF-OH) and a suitable sensitizer (palladium mesoporphyrin IX) have been exploited to produce self-standing autonomous upconverting nanoparticles containing both sensitizer and emitter molecular species.

Finally, chapter 7 displays the modulated synthesis of fluorescent and radioluminescent zirconium based MOF nanocrystals (ZrDPA) and their encapsulation in polymer matrixes for the generation of solid state scintillators. Metal organic frameworks based on zirconium ions oxo-hydroxo clusters and highly fluorescent ligand 4,4'-carboxylphenyl-(9,10)anthracen-dioic acid ($DPA(COOH)_2$) have been synthesized *via* a modulated approach to generate 4 samples of nanometer-sized crystals that display sharp particle size distributions centered between 70 and 360 nm. The samples have been extensively characterized with N_2 and CO_2 adsorption isotherms, infrared and solid-state NMR spectroscopy, thermogravimetric analyses and SEM microscopy. Optical spectroscopic techniques shows high photoluminescence quantum yield that increased along with crystal sizes dimensions due to decrease in the number of surface-related defects and radioluminescent

properties under x-ray irradiation. Nanocrystals of ZrDPA have been embedded in two different polymeric matrixes, polymethyl methacrylate (PMMA) and polydimethyl siloxane (PDMS) to obtain self-standing bulk scintillating materials. These nanocomposites display photoluminescence quantum yield up to 70% and display a high radioluminescence quantum yield coupled with a fast response in the nanosecond domain under irradiation with soft x-rays and γ-rays.

1.3. Publications and contributions

1. Perego, J.; Pedrini, J.; Bezuidenhout, C. X.; Sozzani, P.; Meinardi, F.; Bracco, S.; Comotti, A. and Monguzzi, A.; *Adv. Mater*., **2019**, *31*, 1903309.

2. Comotti, A.; Castiglioni, F.; Bracco, S.; Perego, J.; Pedrini, A.; Negroni, M. and Sozzani, P.; *Chem. Commun*., **2019**, *55*, 8999 - 9002.

3. Perego, J; Piga, D.; Bracco, S.; Sozzani P. and Comotti A.; *Chem. Commun*., **2018**, *54*, 9321 - 9324.

4. Bracco, S., Piga, D., Bassanetti, I., Perego, J., Comotti, A. and Sozzani, P.; *J. Mater. Chem. A*, **2017**, *5*, 10328 – 10337.

5. Comotti, A.; Bracco, S.; Beretta, M.; Perego, J.; Gemmi, M. and Sozzani, P.; *Chem. Eur.J*, **2015**, *21(50)*, 18209 - 18217. (Master thesis)

Manuscript in preparation:

6. Perego, J., Crapanzano, R.; Villa, I.; Pedrini, A.; Bezuidenhout, C. X.; Bracco, S.; Sozzani, P.; Comotti, A.; Vedda, A.; Monguzzi, A.; "Composite Fast Scintillators based on High-Z Fluorescent Metal-Organic Frameworks Nanocrystals", manuscript in preparation.

7. Perego, J.; Shivanna, M.; Bezuidenhout, C. X.; Bracco, S.; Sozzani, P.; Comotti, A.; Zaworotko, M. J.; "Switching metal organic framework driven by coordination isomerism", manuscript in preparation.

Oral presentations, posters and other contributions.

Posters:

"Triphenylmethane Aromatic Frameworks (TAFs): Engineered Pore Chemistry for Targeted Gas Adsorption"

Authors: J. Perego*, D. Piga, S. Bracco, P. Sozzani and A. Comotti.

Conference: POPs 2019, 2nd international symposium on porous organic polymers.
09/09-12/2019, Heidelberg.

"Porous Organic Polymers for high-pressure methane uptake and storage"

Authors: J. Perego*, D. Piga, I. Bassanetti, S. Bracco, A. Comotti and P. Sozzani.

Conference: mc^2 Materials, Characterization, Catalysis.

01/15-16/2018, Zurich.

Oral presentations:

"Polimeri 3D porosi funzionalizzati"

Workshop: "Nanospugne e macchine molecolari: materiali innovativi per la produzione di biometano".

02/18/2019, Milan.

"Highly Porous Organic 3D Polymers for carbon dioxide capture and high-pressure methane storage"

Autumn School: "From waste to microalgae: an example of circular economy".

10/22-23/2019, Gargnano.

2. Porous materials

2.1. Overview

Microporous materials have been known since there have been reports on natural zeolites that describe water vapour release during the heating process of these natural minerals [1,2,3]. The elucidation of two fundamental properties of zeolites, their crystalline nature and their microporous properties, requires a long journey through different centuries [4,5]. During the XX^{th} century many researchers studied and developed the field of artificial zeolites that today includes hundreds of different structures [6,7]. The main feature of these solids is the presence of molecular scale pores inside the material that generate cavities and tunnels that are accessible to guest species. Porosity have been tested and proved *via* adsorption techniques and peculiar phenomena have been exploited and adapted to fulfil the needs of industrial processes. For example, molecular sieving effect has been exploited for xylenes isomers separation; the chemically accessible cations in the structure can be exchanged in desalination processes while the acid/base chemical nature has been exploited for catalytic applications in the petrochemical industry [8]. Along with zeolites, porous activated carbons has been explored as high surface area materials. The rapid development of synthetic methods along the last century in both organic and inorganic realms as well as the development of supramolecular chemistry, led the way to the discovery of novel classes of advanced porous materials. Specifically, the concepts and techniques developed in supramolecular chemistry and the development of novel materials generates the background for the development of novel porous architectures. Porous molecular materials [9], porous coordination polymers and metal organic frameworks (PCPs and MOFs; 1997 and 1998, respectively [10,11]) , polymers of intrinsic porosity (PIMs; 2004) [12]), covalent organic frameworks (COFs, 2005 [13]), porous aromatic frameworks (PAFs, 2009 [14]) and many other microporous materials emerged from different chemical approaches to establish functional and versatile platforms directed towards novel properties and applications.

This Ph.D. thesis deals with the design, synthesis and characterization of many materials belonging to this novel classes and aims at displaying how materials

designed at the molecular level can accomplish advanced tasks and display peculiar properties that are not available in “traditional” materials, although the limited length and extension of the work.

2.2.Microporous materials

Porous materials are classified according to the IUPAC nomenclature based on the pore size width of channels or cavity [15]:

- Macroporus materials: materials with pores larger than 50 nm.
- Mesoporous materials: materials with pores between 2 and 50 nm.
- Microporous materials: materials with pores width less than 2 nm.

Although these definitions are quite arbitrary and can be strongly affected by the nature and shape of pores, they provide a useful guidance in the field of porous materials.

In confined environment properties of the guest phase are strongly affected by the surroundings due to the multiple interactions they experience with pore walls and other molecules along the channel. Microporous materials thus produce a different environment from the one usually experienced by molecules, either in gas, liquid or solid state and generate novel behaviours and properties of guest phases. On the other end, guests molecules can impact mechanical, dynamical and electronic properties of host frameworks.

Microporous materials have been developed through the XX^{th} century. Zeolites and porous carbons have been studied and developed extensively for applications in heterogeneous catalysis (e.g. hydrocarbon cracking process), ions exchange and water desalination. Although these materials arouse great interest even today as testified by recent advances of zeolite chemistry and characterization [16,17], in the last 30 years novel classes of microporous materials aroused interest due to their versatile

structures and multiple properties. A brief introduction to each class of microporous materials is reported below:

- Porous molecular materials. Molecular materials are held together by intermolecular interactions [18]. They can contain intrinsic or extrinsic porosity: the former is due to the packing of units that already display an inner cavity or pores as toroidal molecules (e.g. calixarenes) or molecular cages [19,20], while the latter is generated thanks to the inefficient packing of properly designed molecules in the solid state [21,22].
- Fully-organic microporous polymers feature organic backbone generated by covalent bonds between molecular building blocks[23]. A large variety of microporous polymers can be distinguished based on chemical or structural properties. Polymers of intrinsic microporosity (PIMs) were developed by Budd and McKeown [24]. These materials display similar properties to traditional polymers in solution, while they generate microporous structures due to the inefficient packing of monomeric units in the solid state. Conjugated microporous polymers (CMPs) are based on fully-conjugated backbone: the extended conjugation ensures tunable electronic and optical properties comparable to traditionally inorganic semiconductors counterparts [25,26]. Hyper-crosslinked polymers (HCPs) can be thought as microporous polymer resins generated by cross-linking process of polytopic and rigid building blocks [27,28]. Porous organic frameworks (POFs) are obtained through different coupling mechanisms, from metal-catalyzed coupling reactions to oxidative polymerizations [29,30]. Covalent triazine frameworks (CTFs) are generated by trimerization reaction of nitrile moieties generating materials with high nitrogen content [31]. Finally, the acronym covalent organic frameworks (COFs) has been coined to identify covalent materials that show long range periodicity (cristallinity): their synthesis rely on reversible covalent reactions and is performed under thermodynamic control in order to build up stable and crystalline structures [32,33].
- Metal organic materials. Coordination bonds between metal ions or metal-based clusters and di- or poly-topic linkers generate extended structures that can display high porosity. Metal organic frameworks (MOFs) or porous coordination polymers (PCPs) are highly crystalline microporous solids based

on coordination bonds. Since these materials can be designed by careful choice of the organic and inorganic building blocks, they are a versatile platform for the development of advanced porous materials [34,35].

The interest in microporous materials have been driven by their potential applications. Not surprisingly, microporous materials have been developed for gas storage, gas and vapours capture, separation and related gas managing technologies: entering the "age of gas" requires a detailed understanding of the mechanism and the interactions involved during adsorption/desorption cycles [36]. Moreover, advanced porous materials show promising applications in different fields such as heterogeneous catalysis and photocatalysis, biomedical and bioimaging applications, light harvesting and photonic.

The development of microporous materials has been enabled and sustained by advances in characterization techniques. Gas adsorption measurements provide great amounts of information about pore structure and pore chemistry and they are today routinely performed; *in situ* spectroscopic techniques allowed the full characterization of the adsorption process with atomic resolution. Finally, computational techniques allow in-depth insights into the structure of the solid framework as well as a mechanistic view of the adsorption process.

Different classes of porous materials will be briefly introduced based on their chemical and structural characteristic features.

2.3.Porous molecular materials

Molecular materials usually form dense solids due to the formation of close packed structures that maximise the strength and number of interactions between different units. Porous molecular materials can be generated using two different approaches: the molecules can already present intrinsic void space that line up to form channels and cavities inside the solid material; otherwise, extrinsic porosity can be generated by assembling the molecules into a low-density framework. Since the framework

structure rely on intermolecular interactions porous molecular materials display some distinctive properties compared to extended porous solids based on covalent or coordination bonds [37].

- **Solubility**. Porous molecular cages can be purified and analyzed using conventional techniques as column chromatography and recrystallization typical of organic chemistry. Moreover, porous molecular solids can be easily processed from solution and recycled trough dissolution/recrystallization cycles.
- **Flexibility**. Intermolecular interactions form soft frameworks that can be affected and re-shaped by the interaction with molecular species in the gas or liquid phase. Porous molecular materials can thus respond to external stimuli and efficiently trap molecules.
- Other characteristic such as the synthetic flexibility provided by the rich organic chemistry that can be exploited to generate these materials and generation of dual or multi-functional materials can be easily obtained within porous organic materials.

Molecular materials containing macrocycles and molecular cages can generate porous three dimensional solids if they display shape persistence in the solid state (molecules don't collapse after solvent removal) and generate connected channels by pairing of molecular windows. Due to the flexibility of the three dimensional structure even materials that display isolated cavity and voids inside the structure can adsorb specific guests with high selectivity under suitable conditions due to cooperative mechanism [38,39].

Extrinsic porous molecular materials contains voids generated by the inefficient packing of molecules inside the crystal structure. To obtain these solids molecular building blocks are often design in order to develop strong secondary interactions that stabilize the porous phase and these materials are isolated under kinetic control to avoid the generation of close packed structures. Since the pioneering work of Barrer [40] that demonstrate gas adsorption properties by supramolecular metal-organic

microporous materials, many examples have been reported based on a variety of intermolecular interactions [9,41,42].

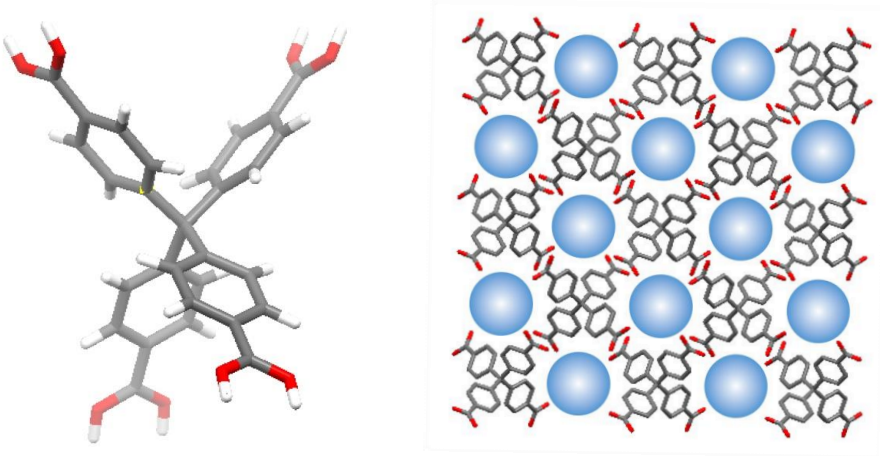

Figure 1. Molecular building block and crystal structure (view along c axis) of TCF-1. Blue circles fit into the channels of the porous structure.The structure is sustained by strong and directional hydrogen bonds between carboxylic acid dimers [41].

2.4.Microporous polymers

Microporous polymers display an extended covalently-linked three dimensional framework [43]. They are usually classified into different classes based on different chemistry or physical properties.

2.4.1. Polymer of intrinsic microporosity (PIMs)

PIMs are linear polymers that possess enough free volume in the de-solvated phase to generate interconnected channels and pores and display a porosity that can be assessed by gas adsorption analysis. Unlike all other categories of microporous polymers, PIMs are soluble linear polymers that can be easily casted from solution to obtain films, membranes and monoliths. This unique feature boosted their applications towards gas separation processes and membrane technology [44,45,46,47]. For example, PIM-1 is synthetized trough a dioxane-forming reaction

between two ditopic monomers that provides a linear polymer [12]. However, the spiro moiety prevents the efficient packing of the polymer chains providing interconnected channels inside the materials. This materials is soluble in common organic polar solvents like THF and can be easily manipulated by casting methods.

2.4.2. Conjugated microporous polymers (CMPs)

CMPs can be though as three dimensional analogues of linear conductive polymers. Different reactions can be exploited to develop fully-conjugated frameworks that are connected through aryl-aryl, aryl-ethynyl or aryl-ethynylene linkages. Yamamoto-type Ullmann coupling, Suzuki cross-coupling coupling, Sonogashira–Hagihara coupling, oxidative coupling reaction, Schiff-base reaction, Friedel–Crafts reaction, phenazine ring fusion reaction and trimerization reaction have been established for the synthesis of CMPs [26]. Microporous organic polymers that feature an extensively conjugated framework can display interesting electronic and conductive properties that are not easily accessible within other classes of porous solids. CMPs have been developed for different applications such as light-harvesting systems, light emitters, chemosensors, heterogeneous catalysts and electrochemical devices [48,49].

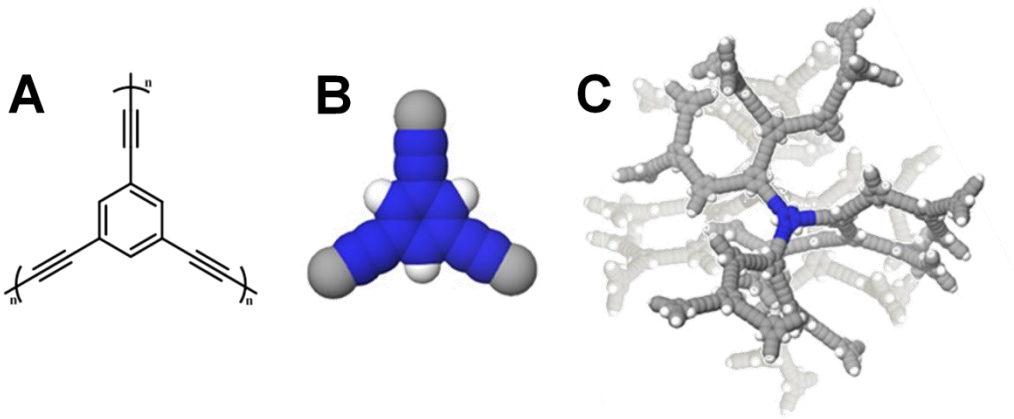

Figure 2. A) Monomeric unit of HCMP-1 [50]. B) Ball and stick model of monomeric unit. C) Schematic representation of three dimensional network of HCMP-1.

2.4.3. Hyper-crosslinked polymers (HCPs)

Hyper-crosslinked polymers are an interesting class of microporous materials that display peculiar characteristics. Low-cost synthetic routes, ease scalability and swelling properties when treated with liquid or gaseous species make HCPs promising for industrial applications as stationary phases in chromatography, adsorbent for gas storage and supports for heterogeneous catalysts.

HCPs can be synthesised *via* crosslinking of preformed linear polymeric chains, direct step growth polymerization of suitable monomers or crosslinking of monomeric units with an external reticulating agents. Davankov et *al.* demonstrated that microporous HCPs with BET surface areas as high as 2000 m^2/g can be generated from polystyrene by extensive crosslinking exploiting Friedel-Crafts alkylation reaction [51,52]. Linear polymer chains or solvent-swollen lightly crosslinked gels have been treated with reactive species (e.g. monochlorodimethyl ether) and suitable catalysts (e.g. $FeCl_3$) in presence of a solvating medium to generate an extensively cross-linked phase. During solvent removal process the material cannot collapse producing a microporous framework.

HCPs have been generated by direct polycondensation of functionalized monomers as, for example, dichloroxylene. Moreover, even un-functionalized aromatic building blocks can produce highly porous frameworks when reticulated with an external crosslinking agent as formaldehyde dimethyl acetal (FDA), *p*-dibromo xylene or 1,4-dimethoxybenzene [53,54].

2.4.4. Porous aromatic frameworks (PAFs)

The prototype of POFs is porous aromatic framework-1 (PAF-1) which is composed of tetrahedral units (*tetrakis* (4,4',4'',4'''-bromo(phenyl))methane) joined *via* Yamamoto-type Ullman cross-coupling that generate a 3D amorphous framework with ultra-high surface area up to 5600 m^2/g [14]. PAFs are open framework porous polymers bearing outstanding surface area and high chemical and thermal stability due to the strong covalent bonds between aromatic units that sustain the extended

structure. These materials can find widespread applications in gas adsorption and storage thanks to their outstanding adsorptive properties, as well as supports for heterogeneous catalysts and many other [55,56].

2.5. Covalent organic frameworks (COFs)

Covalent organic frameworks have been introduced in 2005 by A. Côté et *al.* [13] These materials display skeletons generated by lightweight atoms (C, N, H, O, B, S, Si) that display long-range order in striking contrast with other microporous polymers. Crystalline structures can be accessed thank to the exploitation of reversible and dynamic chemical reactions that guarantee error-checking mechanisms during polymerization reactions and the generation of the thermodynamic products. The first reported COF rely on the condensation reaction of boronic acid: although the product show good micro-crystallinity and adsorption properties, the ease hydrolisis of B···O bonds determines the high chemical instability of the resulting solid in humid environments. Today, a plethora of different chemical reactions have been developed for the fast synthesis of COFs that can be growth as single crystals and display high stability even in water.[57,58]

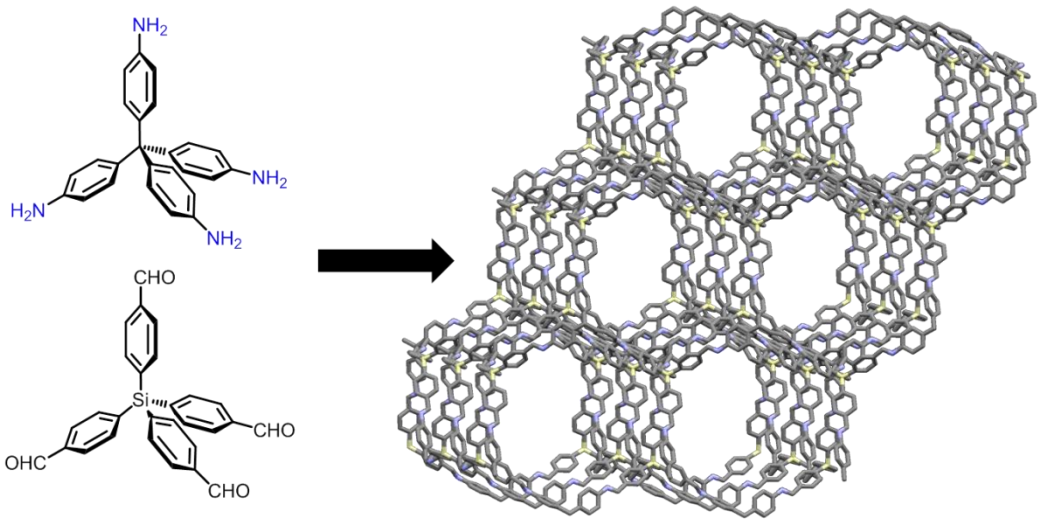

Figure 3. Molecular building blocks of COF LZU-111 and one of its three-fold interpenetrated three dimensional diamondoid framework.

Even though three dimensional COFs have been synthesised in the last years, a great effort has been put in the development of 2D materials that can be seen as organic analogous of graphenes and two-dimensional elemental or inorganic materials. Two dimensional materials can be potentially integrated in microelectronic devices and can be exploited in different applications as electrochemical and photo-electrochemical sensors, electrode materials for lithium batteries and gas separation processes.[59,60]

2.6.Metal-organic frameworks (MOFs)

Coordinative bond was reported for the first time by A. Werner in 1893 as he recognized how metal complexes contains neutral ligands inside their coordination sphere along with the counteranions that provide charge balance. [61]. The outstanding structural and functional versatility of coordination chemistry provided an extremely rich environment for the development of new branches of chemistry as well it paved the way for the development of novel classes of materials generated by coordination-driven self-assembly processes. These materials can be classified as metal-organic materials (MOMs) due to their hybrid chemical nature and can be separated in two main different subclasses:

- Supramolecular coordination complexes (SCCs).
- Coordination polymers (CPs).

SCCs comprise discrete supramolecular entities generated by the self-assembly of metal ion precursors and organic ligands; these supramolecules can be dissolved and crystallized to generate three dimensional materials exploiting intermolecular interactions. Instead, coordination polymers features extended frameworks due to the divergent character of their molecular tectons: solid crystalline materials can be synthetized in one reaction thank to the reversible nature of the coordination bond (Figure 4). Novel materials such as metal organic polyhedra (MOPs) partially bridge the gap between these two different but related branch of materials chemistry.

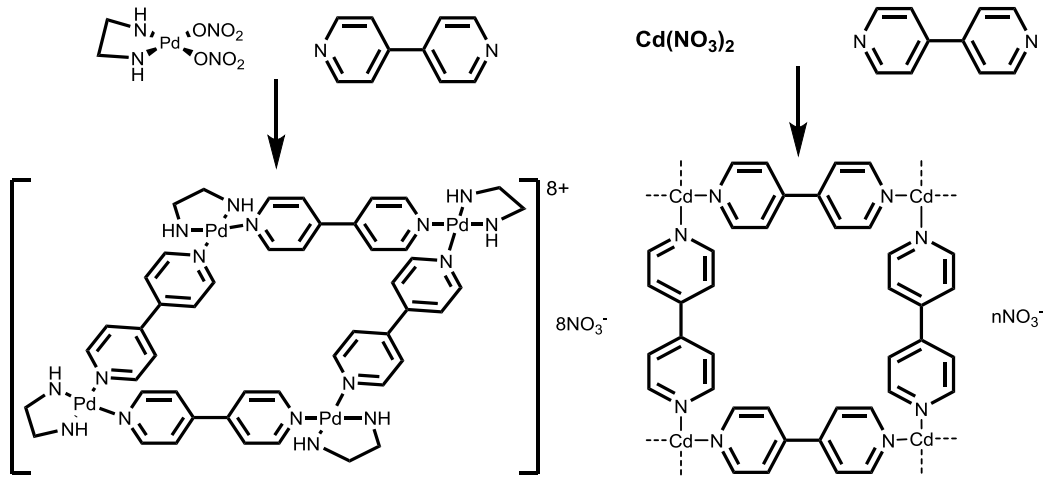

Figure 4. Left: discrete supramolecular coordination complex (0D metal organic materials). Right: coordination polymer. This two example display how different dimensionality can be achieved employing the same molecular building block [62,63].

In the next paragraph I will focus on the development of coordination polymers. Prussian blue, known from the XVIII century can be considered as the prototypal coordination polymer: Fe (II) and Fe(III) cations coordinate in an octahedral geometry cyanide anions that guarantee the electroneutrality of the primitive cubic framework as demonstrated in 1977 from single crystal data [64]. Instead, the development of metal organic coordination polymers can be related to the seminal peper of Hoskins and Robson [65] that shows the formation of diamondoid framework upon the coordination of *tetrakis* (4,4',4'',4''' tetracyano-tetraphenylmethane) with Cu(I) ions: the positively charged framework is neutralized by disordered tetrafluoroborate anions hosted inside the tetrahedral cages along with nitrobenzene molecules.

Metal organic frameworks (MOFs) or porous coordination polymers (PCPs) were described in literature for the first time independently by Kitagawa and Yaghi research groups in 1997 and 1998, respectively. This subclass of coordination polymers showed permanent porosity after solvent removal giving access to novel coordination-based porous materials [66,67]. Since these seminal papers a big amount of work have been performed on MOFs boosted by the rapid increase in the surface area values reported for these novel frameworks [68]. Metal-organic frameworks are generated by coordination of metal ions or clusters with organic linkers. The metal

clusters can be preparaed as stable supramolecular complexes and then the framework can be build through a linker exchange mechanism or, more often, can be formed *in situ* during MOFs crystallization giving access to a higher variety of inorganic SBUs.

These materials display high synthetic and structural versatility that enable the design and development of materials with specific physical and chemical properties for targeted applications. MOFs design can be exploited at different level and with various techniques. A brief account of strategic design of MOFs and selected applications is given below.

Different functional groups have been included in the organic struts of MOFs. Di and poly-topic linkers with carboxylic acids, pyridines, azoles and mixed functional groups generates an almost infinite library that can be exploited for pore size, shape and pore chemistry modulation. (Figure 5)

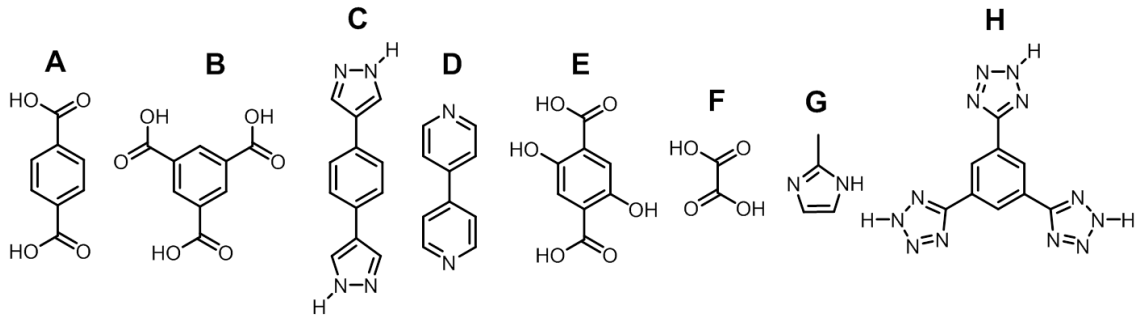

Figure 5. Different linkers used in metal organic framework synthesis.

Single metal cations or metal clusters give rise to an outstanding variety of frameworks. Nodes generated by single metal cation usually display high flexibility that can generate the collapse of the framework during the solvent removal process. However, multi-nuclear metal clusters provided higher rigidity and connectivity usually associated to increased porosity. Usually metal clusters are generated during the growth of the metal organic material, but they can be sometimes introduced as pre-formed clusters generating the extended 3D framework with a ligand-exchange process. The term secondary building unit (SBU) has been borrowed from zeolite chemistry and it refers to the cluster generated from the metal cations and the functional groups that determine the connectivity and spatial disposition of linkers inside the structure. (figure 6)

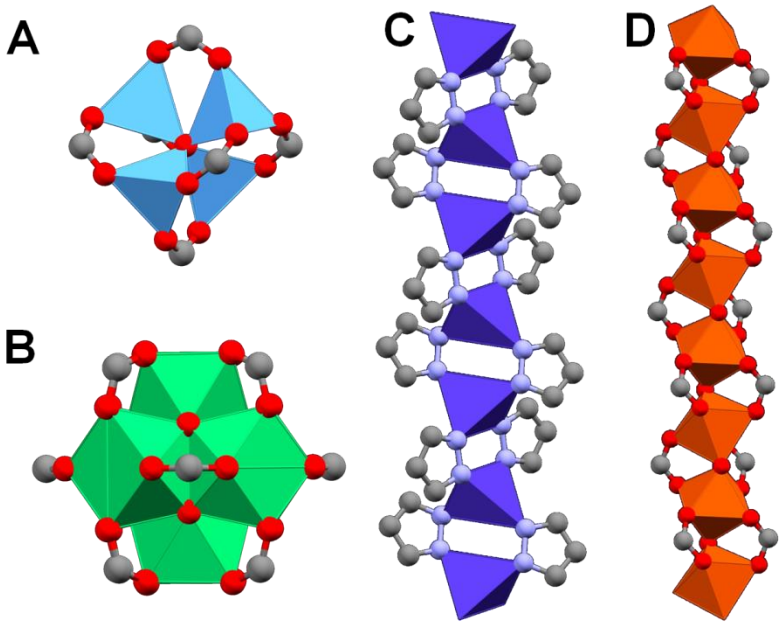

Figure 6. Selected secondary building units. A) Octahedral SBU $Zn_4O(COO^-)_6$. B). $Zr_6(\mu\text{-}O)_4(\mu\text{-}OH)_4(COO^-)_{12}$. Rod secondary building units: C) Co(bdp) MOF. D) MIL-53(Fe). Color code: C, grey; O red; N, blue; Zn, light blue; Zr, green; Co, purple; Fe, orange.

Many reviews and special issues have been published on selected applications and special classes of MOFs [69,70].

2.7.References

[1] Cronstedt, A. F;Kongl Vetenskaps Academiens Handlingar Stockholm, **1756**, *17*, 120-123.

[2] Colella, C. and Gualtieri, F. A.; Microporous Mesoporous Mater., **2007**, *105*, 213 – 221.

[3] Masters, A. F. and Maschmeyer, T.; Microporous Mesoporous Mater., **2011**, *142*, 423 – 438.

[4] Jaeger, F. M.; Trans. Faraday Soc., **1929**, *25*, 320 – 349.

[5] Baur, W. H. and Fisher, R. X.; Microporous Mesoporous Mater., **2008**, *116*, 1 – 3.

[6] Barrer, R. M.; Proc. R. Soc. (Lond.), **1938**, *167 (930)*, 393 – 420.

[7] http://www.iza-online.org/

[8] Gläser R., Weitkamp J. (2004) The Application of Zeolites in Catalysis. In: Baerns M. (eds) Basic Principles in Applied Catalysis. Springer Series in Chemical Physics, *75*. Springer, Berlin, Heidelberg.

[9] Sozzani, P., Bracco, S., Comotti, A., Ferretti, L. and Simonutti, R.; Angew. Chem. Int. Ed., **2005**, *44*, 1816 –1820.

[10] Kondo, M., Yoshitomi, T., Seki, K., Matsuzaka, H. and Kitagawa S.; Angew. Chem. Int. Ed., **1997**, *36 (16)*, 1725 – 1727.

[11] Li, H., Eddaoudi, M., Groy, T. L. and Yaghi, O. M.; J. Am. Chem. Soc., **1998,** *120 (33)*, 8571-8572.

[12]Budd, P. M., Ghanem, B. S., Makhseed, S., McKeown, N. B., Msayiba, K. J. and Tattershall, C. E.; Chem. Commun.**, 2004**, 230 - 231.

[13] Côté, A. P., Benin, A. I., Ockwig, N. W., O'Keeffe, M., Matzger, A. J. and Yaghi O. M.; Science, **2005**, *310*, 1166 - 1170.

[14] Ben, T., Ren, H., Ma, S., Cao, D., Lan, J., Jing, X., Wang, W., Xu, J., Deng, F., Simmons, J. M., Qiu, S. and Zhu, G.; Angew. Chem. Int. Ed., **2009**, *48*, 9457 – 9460.

[15] Thommes, M., Kaneko, K., Neimark, A. V., Olivier, J. P., Rodriguez-Reinoso, F., Rouquerol, J. and Sing K. S. W.; Pure Appl. Chem., **2015**, *87(9-10)*, 1051 – 1069.

[16] Mazur, M., Wheatley, P. S., Navarro, M., Roth, W. J., Položij, M., Mayoral, A., Eliášová, P., Nachtigall, P., Čejka, J. and Morris, R.E.; Nature Chem., **2016**, *8*, 58 – 62.

[17] Prech, J., Pizarro, P., Serrano, D. P.and Cějka, J.;Chem. Soc. Rev., **2018**, *47*, 8263 – 8306.

[18] Holst, J. R., Trewin, A. and Cooper, A. I.; Nature Chem., **2010**, *2*, 915 – 920.

[19] Dalgarno, S. J., Thallapally, P. K., Barbour, L. J. and Atwood J. L.; Chem. Soc. Rev., **2007**, *36*, 236–245.

[20] Mastalerz, M.; Acc. Chem. Res., **2018**, *51 (10)*, 2411 - 2422.

[21] Yamagishi H., Sato H., Hori A., Sato Y., Matsuda R., Kato K., Aida T.; Science, **2018**, *361*, 1242 – 1246.

[22] Xing, G., Bassanetti, I., Bracco, S., Negroni, M., Bezuidenhout, C. X., Ben, T., Sozzani, P. and Comotti, A.; Chem. Sci., **2019**, *10*, 730 – 736.

[23] Das, S., Heasman, P., Ben, T. and Qiu, S.; Chem. Rev., **2017**, *117(3)*, 1515 - 1563.

[24] McKeown N. B. and Budd, P. M.; Chem. Soc. Rev., **2006**, *35*, 675–683.

[25] Cooper, A. I.; Adv. Mater., **2009**, *21*,1291–1295.

[26] Xu, Y., Jin, S., Xu, H., Nagai, A. and Jiang D.; Chem. Soc. Rev., **2013**, *42*, 8012 – 8031.

[27] Tana, L. and Tan, B.; Chem. Soc. Rev., **2017**,*46*, 3322-3356.

[28] Huang, J. and Turner, S. R.; Polymer Reviews, **2017**, *58(1)*, 1 – 41.

[29] Ben, T., and Qiu, S.; CrystEngComm, **2013**, *15*, 17 – 26.

[30] Yuan, Y. and Zhu, G.; ACS Cent. Sci., **2019**, *5*, 409 – 418.

[31] Liu, M., Guo, L., Jin, S. and Tan B.; J. Mater. Chem. A, **2019**, *7*, 5153 - 5172.

[32] Diercks, C. S. and Yaghi, O. M.; Science, **2017**, *355*, 923 – 931.

[33] Chen, X., Geng, K., Liu, R., Tan, K. T. Gong, Y., Li, Z., Tao, S., Jiang, Q. and Jiang, D.; Angew. Chem., Int. Ed., **2019**, *58*, 2 – 44.

[34] O'Keeffe, M. and Yaghi, O. M.; Chem. Rev., **2012**, *112*, 675 – 702.

[35] Férey, G.; Chem. Soc. Rev., **2008**, *37*, 191 – 214.

[36] Kitagawa, S.; Angew.Chem.Int.Ed., **2015**, *54*, 10686 – 10687.

[37] McKeown, N. B.; J. Mater. Chem., **2010**, *20*, 10588–10597.

[38] Atwood, J. L., Barbour, L. J., Jerga, A. and Schottel, B. L.; Science, **2002**, *298*, 1000 – 1002.

[39] Barbour, L. J.; Chem. Commun., **2006**, 1163 – 1168.

[40] Allison, S. A. and Barrer, R. M.; J. Chem. Soc. A, ***1969***, 1717 - 1723.

[41] Bassanetti, I., Bracco, S., Comotti, A., Negroni, M., Bezuidenhout, C. X., Canossa, S., Mazzeo, P. P., Marchió L. and Sozzani, P.; J. Mater. Chem. A, **2018**, *6*, 14231–14239.

[42] Tian, J., Thallapally, P.K. and McGrail, B. P.; CrystEngComm, **2012**, *14*, 1909 – 1919.

[43] Chaoui, N., Trunk, M., Dawson, R., Schmidt, J. and Thomas, A.; Chem. Soc. Rev., **2017**, *46*, 3302 – 3321.

[44] McKeown, N. B., Budd, P. M., Msayib, K. J., Ghanem, B. S., Kingston, H. J., Tattershall, C. E., Makhseed, S., Reynolds, K. J. and Fritsch, D.; Chem. Eur. J., **2005**, *11*, 2610 – 2620.

[45] Du, N., Robertson, G. P., Song, J., Pinnau, I., Thomas, S. and Guiver, M. D.; Macromolecules, **2008**, *41*, 9656 - 9662.

[46] Ghanem, B. S., Swaidan, R., Litwiller, E. and Pinnau, I.; Adv.Mater., **2014**, *26*, 3688 – 3692.

[47] Rose, I., Carta, M., Malpass-Evans, R., Ferrari, M.-C., Bernardo, P., Clarizia, G., Jansen, J. C. and McKeown, N. B.; ACS Macro Lett., **2015**, *4*, 912 − 915.

[48] Gu, C., Huang, N., Wu, Y., Xu, H. and Jiang, D.; Angew. Chem. Int. Ed., **2015**, *54*, 11540 – 11544.

[49] Jin, E., Asada, M., Xu, Q., Dalapati, S., Addicoat, M. A., Brady, M. A., Xu, H., Nakamura, T., Heine, T., Chen, Q. and Jiang, D.; Science, **2017**, *357*, 673 – 676.

[50] Jiang, J.-X., Su, F., Niu, H., Wood, C. D., Campbell, N. L., Khimyak, Y. Z. and Cooper, A. I.; Chem. Commun., **2008**, 486 – 488.

[51] Tsyurupa, M. P. and Davankov, V.A.; Reactive & Functional Polymers, **2002**, *53*, 193 – 203.

[52] Tsyurupa, M. P. and Davankov, V.A.; Reactive & Functional Polymers, **2006**, *66*, 768 – 779.

[53] Huang, J. and Turner, S. R.; Polymer Reviews, **2018**, *58 (1)*, 1 – 41.

[54] Tan, L. and Tan, B.; Chem. Soc. Rev., **2017**, *46*, 3322 – 3356.

[55] Ben, T., Pei, C., Zhang, D., Xu, J., Deng, F., Jing, X. and Qiu, S.; : Energy Environ. Sci., **2011**, *4*, 3991 – 3999.

[56] Ben, T., Qiu, S.; CrystEngComm, **2013**, *15*, 17 – 26.

[57] Zhang, Y. B., Su, J., Furukawa, H., Yun, Y., Gándara, F., Duong, A., Zou, X. and Yaghi O. M.; J. Am. Chem. Soc., **2013**, *135 (44)*, 16336 - 16339.

[58] Ma, T., Kapustin, E. A., Yin, S. X., Liang, L., Zhou, Z., Niu, J., Li, L.-H., Wang, Y., Su, J., Li, J., Wang, X., Wang, W. D., Wang, W., Sun, J. and Yaghi O. M.; Science, **2018**, *361*, 48 – 52.

[59] Lyle, S. J., Waller, P. J. and Yaghi, O. M.; Trends in Chemistry, **2019**, *1 (2)*, 172 – 184.

[60] Wang, H., Zeng, Z., Xu, P., Li, L., Zeng, G., Xiao, R., Tang, Z., Huang, D., Tang, L., Lai, C., Jiang, D., Liu, Y., Yi, H., Qin, L., Ye, S., Rena, X. and Tang, W.; Chem. Soc. Rev., **2019**, *48*, 488 – 516.

[61] Cook, T. R., Zheng, Y.-R. and Stang, P. J.; Chem. Rev., **2013**, *113*, 1734-1777.

[62] Fujita, M., Yazaki, J. and Ogura, K.; J. Am. Chem. Soc., **1990**, *112 (14)*, 5645 – 5647.

[63] Fujita, M., Kwon, Y. J., Washizu, S. and Ogura, K.; J. Am. Chem. Soc., **1994**, *116*, 1151 - 1152.

[64] Buser, H. J., Schwarzenbach, D., Fetter, W. and Ludi, A.; Inorganic Chemistry, **1977**, *16*, 2704 – 2710.

[65] Hoskins, B. F. and Robson, R.; J. Am. Chem. Soc., **1989**, *111 (15)*, 5962 – 5964.

[66] Kondo, M., Yoshitomi, T., Seki, K., Matsuzaka, H. and Kitagawa, S.; Angew. Chem. Int. Ed., **1997**, *36*, 1725 – 1727.

[67] Li, H., Eddaoudi, M., Groy, T. L. and Yaghi, O. M.; J. Am. Chem. Soc., **1998**, *120*, 8571 - 8572.

[68] Li, H., Eddaoudi, M., O'Keeffe, M. and Yaghi O. M.; Nature, **1999**, *402*, 276 – 279.

[69] Themed collection: Metal-organic frameworks and porous polymers – current and future challenges.

Maurin, G., Serre, C., Cooper, A. and Férey, G.; Chem. Soc. Rev., **2017**, *46*, 3104 – 3107.

[70] Themed issue on Metal Organic Frameworks (MOFs).

Zhou, H.-C. and Kitagawa, S.; Chem. Soc. Rev., **2014**, *43*, 5415 – 5418.

3. Tailored gas adsorption properties in porous organic materials

3.1. Pore wall decoration of porous organic polymers

3.1.1. Summary

In this chapter porous organic frameworks (POFs) based on triphenylmethane building blocks will be described and their adsorption properties towards carbon dioxide and methane will be discussed. Specifically, three dimensional porous frameworks have been synthetized from pre-functionalized monomeric units bearing hydroxyl or amino functional groups that are fully retained and homogeneously distributed inside the resulting materials. Three different frameworks have been generated: a porous polymer that does not bear any functional group (TPAF = Triphenilmethane-based porous aromatic frameworks), a framework bearing an amino group on the central carbon atom (TPAF-NH_2) and its hydroxyl analogue (TPAF-OH). Different functional groups affect the porous properties of the materials and determine a different ratio between micro and mesopores as determined from nitrogen adsorption isotherms at 77 K. Aliphatic amino groups interact strongly with carbon dioxide displaying an isosteric heat of adsorption (Q_{st}) up to 54 kJ/mol at room temperature. The strong interaction between the guest CO_2 molecules and the amino groups decorating the pore walls has been deeply investigated by 2D ^{1}H–^{13}C heterocorrelated MAS NMR: carbon dioxide molecules sit in close contact with the hydrogen of the amino groups and interact with the aromatic proton of benzene rings that surround the functional group. On the other hand, hydroxyl groups and a higher micropore percentage increase the interaction with methane molecules: TPAF-OH displays an isosteric heat of adsorption up to 21 kJ/mol at low coverage. Moreover, treatment of TPAF-OH with lithium hydride allows the post-synthetic generation of lithium alkoxide groups (TPAF-OLi) that enhance the affinity of the framework towards methane molecules (Q_{st} = 25 kJ/mol). Moreover, the possible application in adsorbed methane storage technology has been investigated measuring high pressure methane adsorption isotherms up to 100 bar: TPAF displayed a working capacity up to 200 cm^3/g between 100 bar and 5 bar at room temperature.

Related paper:

"Expandable porous organic frameworks with built-in amino and hydroxyl functions for CO_2 and CH_4 capture",

Perego, J.; Piga, D.; Bracco, S.; Sozzani, P. and Comotti, A.

Chem. Commun., **2018**, *54*, 9321-9324.

3.1.2. Porous organic frameworks (POFs): carbon dioxide capture and separation and methane adsorption

The increase of carbon dioxide concentration since the beginning of the industrial revolution raised great concern in the scientific community and in public opinion [1]. Specifically, the increase of the Greenhouse effect strictly related to global warming and the acidification of oceans speeded up due to the increasing emission of carbon dioxide in the atmosphere related to human activities [2,3,4].

Since the energy demand will increase in the future by 53% by 2030 and the complete transition towards CO_2-neutral technology is still in its infancy there is a great efforts in the development of new technologies and processes for CO_2 capture, sequestration and utilization (CCSU) [3,5]. Different CO_2 capture technologies are currently under investigation and many of them are already implemented on an industrial scale [5,6]:

- Post-combustion CO_2 capture. Removal of carbon dioxide from gas streams after combustion processes
- Oxyfuel process. Use of pure oxygen instead of air to increase the CO_2 concentration in the flue gas.
- Pre-combustion CO_2 capture.
- Direct air CO_2 capture.

For example, since about 44 % of anthropogenic CO_2 emissions come from coal, oil or natural gas- fired power plants, post-combustion technologies have been greatly developed in order to separate and recover CO_2 from flue gas. The current state of the art is chemical adsorption performed with solvents based on amines, alkali or amino-acods salts. After the adsorption process, carbon dioxide is removed from the solvent using a temperature or pressure-swing regeneration process. Then the solvent can be recirculated inside the plant and the CO_2 processed for transport, storage and utilization [7,8].

Porous organic frameworks (POFs) display valuable properties that make them attractive towards applications in gas separation and storage. High thermal and chemical stability as well as high synthetic flexibility allow to optimize POFs for gas capture, separation and storage processes. The utilization of porous materials that exhibit high CO_2 loading, high selectivity and fast kinetics adsorption can improve the current technology for carbon dioxide sequestration based on liquid amine scrubbing processes. Specifically, solid sorbents can be easily recycled due to their lower interactions with carbon dioxide molecules resulting in less energy-intense processes. Moreover, stable frameworks can provide higher recyclability compared to liquid amine scrubbing processes [9,10,11,12,13,14,15,16].

In our work we study from a fundamental point of view the effect of pore functionalization on the adsorptive properties of porous organic frameworks.

3.1.3. Triphenylmethane-based porous aromatic frameworks (TPAFs)

3.1.3.1. Synthesis and physico-chemical characterization

Three different building blocks have been designed and synthetized containing three reactive bromine groups and a functional group on the central carbon atom. The reaction proceeds *via* preparation of a mono-lithiated reactant from 4,4'-dibromobenzene under inert and low temperature (-78°C) conditions and its nucleofilic substitution reaction with diethylcarbonate in 3:1 ratio to give *tris*-(4-bromophenyl)methanol in high yield and purity after a washing step in hexane (see

Experimental Section for further details). The hydroxyl group can then be replaced by a hydrogen atom or an amino group as reported in the scheme below.

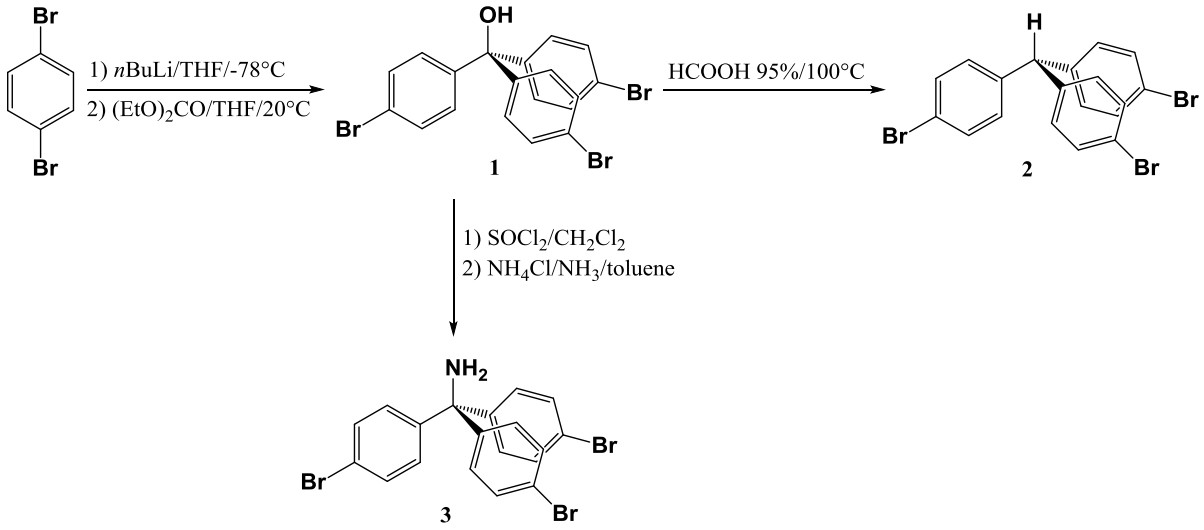

Scheme 1. Synthetic strategy to obtain the three different functionalized monomers.

The building blocks have been characterized with DSC, infrared spectroscopy and ^{1}H liquid NMR spectroscopy.

To generate an extended framework Yamamoto-type Ullmann coupling reaction has been employed to obtain a direct coupling between aryl units. This reaction ensures quantitative yield and minimize the residual impurities contained in the resulting framework.

Three extended networks have been obtained through homocoupling of the different units: TPAF, which contains unfunctionalized ternary carbon atom, TPAF-OH and TPAF-NH_2. Chemical and structural information on these amorphous samples (see Fig.X) have been collected *via* elemental analysis, thermogravimetric analysis, infrared spectroscopy, solid state NMR and nitrogen adsorption isotherms at 77 K.

TGA measurements show thermal stability of the samples up to 350 °C. Nitrogen content of TPAFNH_2 of 5.1%$_{wt}$ and oxygen content of 6.0 %$_{wt}$ in TPAFOH are in good agreement with the calculated values of 5.5 %$_{wt}$ and 6.2 %$_{wt}$, respectively, corroborating that the functional groups inserted inside the frameworks are not altered during the reticulation process.

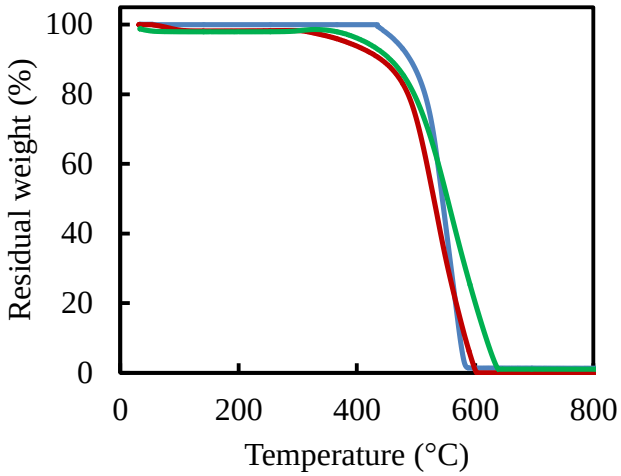

Figure 1. Thermogravimetric analysis of TPAF (blue), TPAF-OH (red) and TPAF-NH_2 (green).

Table 1. Elemental analysis of samples TPAF, TPAF-OH and TPAF-NH_2.

Sample	**C**		**H**		**N**		**O**	
	Calc	Exp	Calc	Exp	Calc	Exp	Calc	Exp
TPAF	94.5	91.6	5.4	5.5	0	0.4	0	-
TPAF-OH	88.7	86.2	5.1	5.3	0	0.4	6.2	6.0
TPAF-NH_2	89.0	85.7	5.5	5.6	5.5	5.1	0	-

Spectroscopic techniques prove the full retainment of hydrogen atom, hydroxyl or amino groups in resulting frameworks. FT-IR spectroscopy allows us to determine some structural features and to confirm qualitatively the maintenance of chemical functionality during frameworks syntheses. All samples show multiple bands in the range 3000-3100 cm^{-1} due to aromatic C-H stretching. Distinctive bands related to the functionality of the ternary carbon appear in the regions 1000-1600 cm^{-1} and 3000-3600 cm^{-1}. In the former the C-O stretch gives rise to a sharp peak at 1158 cm^{-1} and an additional peak at 920 cm^{-1} usually observed for tertiary alcohols. In the latter region free O-H moieties gives rise to a sharp peak at 3580 cm^{-1} while a broad band at 3480 cm^{-1} is caused by hydrogen bonded O-H···O groups. TPAF-NH_2 shows

absorption bands at 3320 and 3380 cm^{-1} due to symmetric and asymmetric stretch of N-H bond.

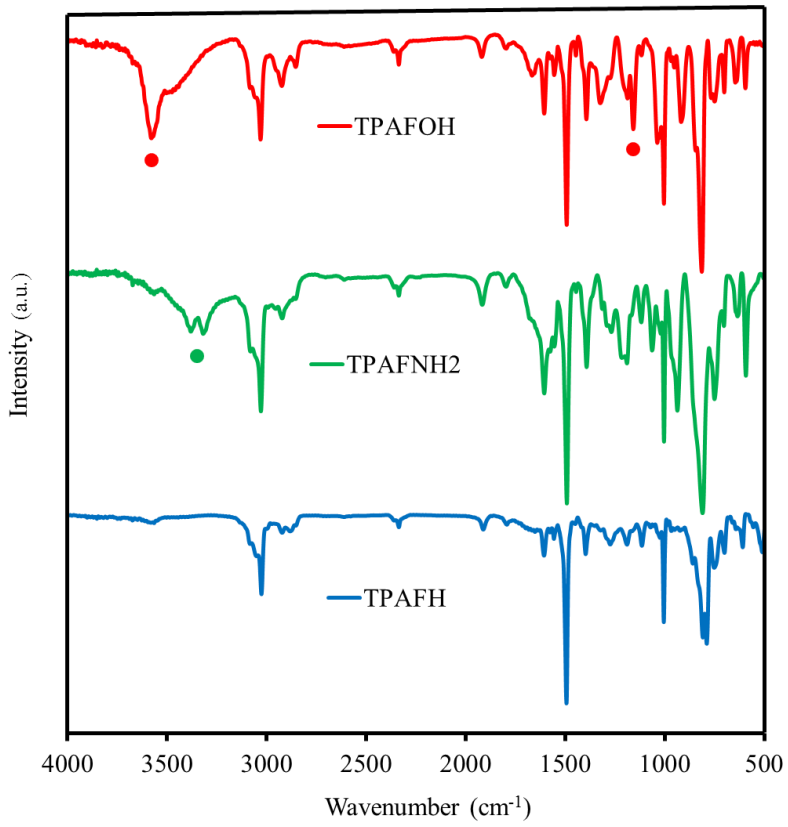

Figure 2. Infrared spectra of TPAF-H (blue), TPAF-NH_2 (green) and TPAF-OH (red). Characteristic absorption bands related to the installed functional groups are marked by dots (see the text for discussion).

Both ^{1}H and ^{13}C solid state NMR spectra prove the formation of the desired frameworks. ^{13}C MAS solid state NMR spectra feature a large shift of the signal related to the central carbon atoms from 56.2 ppm in TPAF to 65.7 ppm in TPAFNH_2 and 81.3 ppm in TPAFOH. Moreover, the deconvolution of the experimental spectra using Lorentzian and Gaussian lineshapes allow to confirm the 1 to 3 ratios between the central carbon atom and the aromatic ones. ^{1}H solid state NMR spectra clearly display the different chemical shifts generated by different moieties installed inside the framework. Finally, recording ^{13}C CP MAS NMR spectra at different contact times (50 μs and 2 ms, respectively) allow to recognise the peaks due to quaternary

carbon atom and thus make a proper assignment of each peak in the solid state NMR spectra. (Figure 3,4)

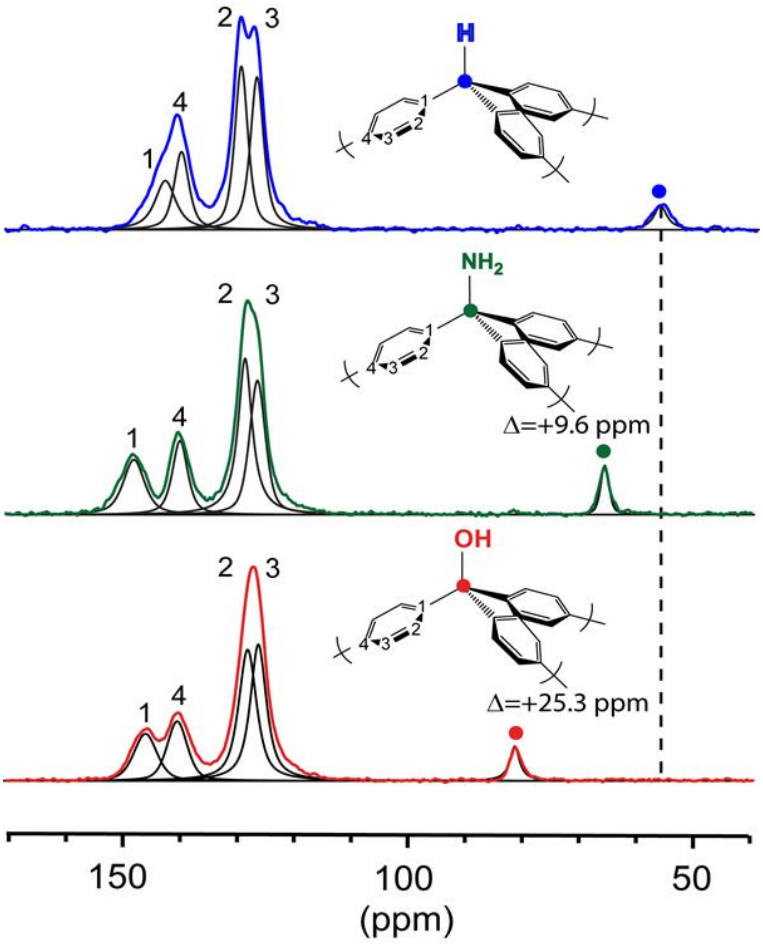

Figure 3. ^{13}C MAS solid state NMR spectra of TPAF (blue), TPAF-OH (red) and TPAF-NH_2 (green). The spectra were deconvoluted using Lorentzian and Gaussian line-shapes.

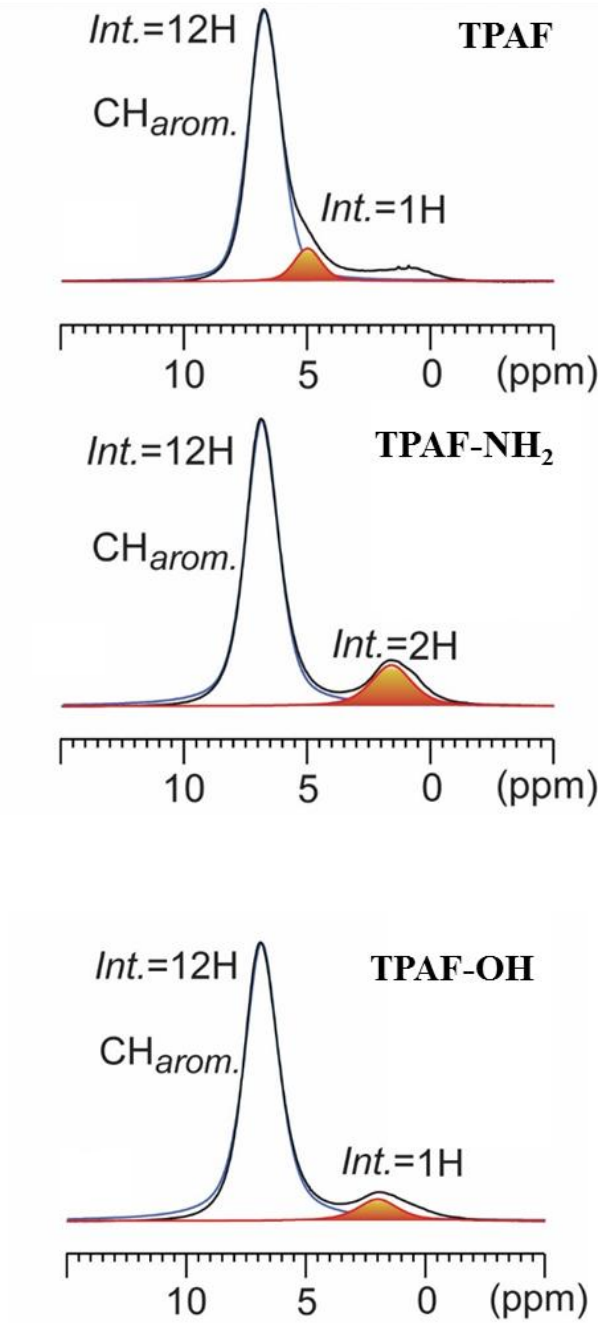

Figure 4. ^{1}H solid state NMR spectra of TPAF (top), TPAF-NH_2 (middle) and TPAF-OH (bottom).

Nitrogen adsorption isotherms measured at 77 K provided Langmuir and BET surface areas of 1565, 1343, and 1108 m^2/g and 1383, 1190, and 984 m^2/g for TPAF, TPAF-NH_2 and TPAF-OH. The surface areas and pore-volumes (0.95, 0.68 and 0.45 cm^3/g for TPAF, TPAF-NH_2 and TPAF-OH), are comparable or superior to many of the best performing functionalized POFs, despite the volume occupied by the organic functions in the pores. Nitrogen desorption branches run distinctly above the

adsorption curves, especially for TAF, forming large hysteresis loops indicative of the framework swellability with an increased pore capacity after expansion.

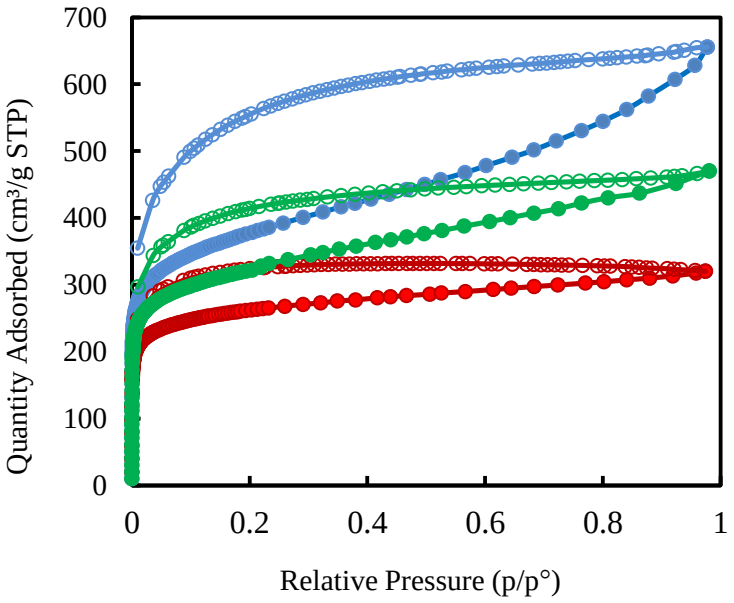

Figure 5. Nitrogen adsorption isotherms of TPAF (light blue), TPAF-OH (green) and TPAF-NH_2 (red) measured at 77 K.

Table 2. Adsorptive properties of TPAF, TPAF-OH and TPAF-NH_2. Langmuir and BET surface area are calculated from nitrogen adsorption isotherms at 77 K; pore size distribution is calculated according to non-local DFT theory and N_2@77 K carbon slit pore model.

Sample	**Langmuir surface area (m^2/g)**	**BET surface (m^2/g)**	**Pore volume (cm^3/g)**	**Micro/ Mesopore ratio (%)**
TPAF	1565	1383	0.95	47
TPAF-NH_2	1343	1190	0.68	60
TPAF-OH	1108	984	0.45	78

3.1.3.2. Carbon dioxide adsorption properties

Carbon dioxide adsorption isotherms have been measured at 3 different temperatures (273 K, 283 K and 298 K) to evaluate the adsorptive properties of the materials. CO_2

adsorption isotherms revealed high gas uptakes already at low pressure. The uptake up to 1 bar reaches 41 cm^3/g (1.9 mmol/g) at ambient temperature and 71 cm^3/g (3.2 mmol/g) at 273 K in TPAF–NH_2. The adsorption isotherms have been fitted with a dual site Langmuir model and have been elaborated by the van't Hoff equation to calculate the isosteric heat of adsorption at low coverage as high as 54 kJ/mol (13 kcal/mol) for the amine derivative, which outperforms the other two compounds (26 kJ/mol and 30 kJ/mol for TPAF and TPAF-OH, respectively) and it is comparable to the highest values reported for amine-modified porous organic frameworks. The strong interaction of TPAF–NH_2 has been accounted for by the favourable activity of the aliphatic amines that display higher basicity compared to aromatic amines.

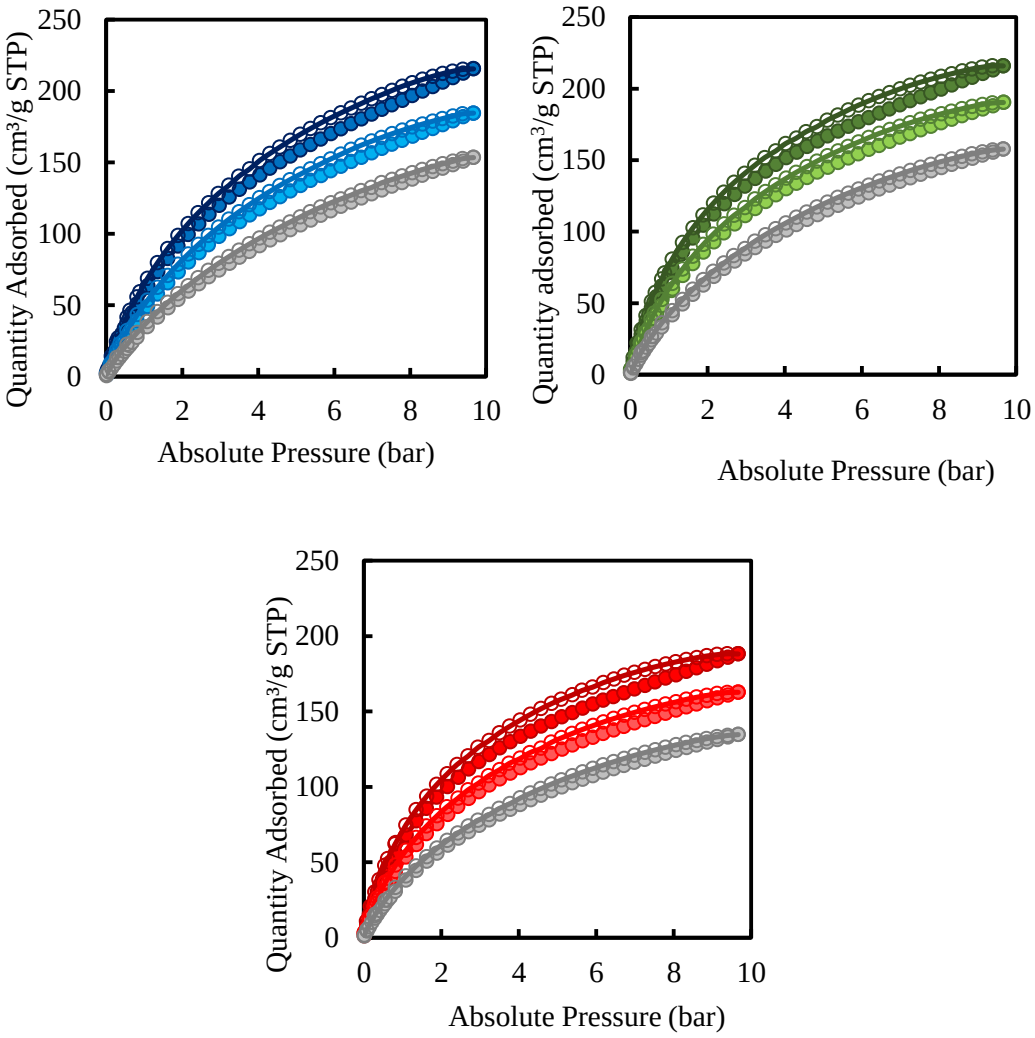

Figure 6. A) CO_2 adsorption isotherms of TPAF-H at 273 K (blue), 283 K (light blue) and 298 K (grey) measured up to 10 bar. B) CO_2 adsorption isotherms of TPAF-NH_2 at 273 K

(green), 283 K (light green) and 298 K (grey). C) CO_2 adsorption isotherms of TPAF-OH at 273 K (red), 283 K (light red) and 298 K (grey).

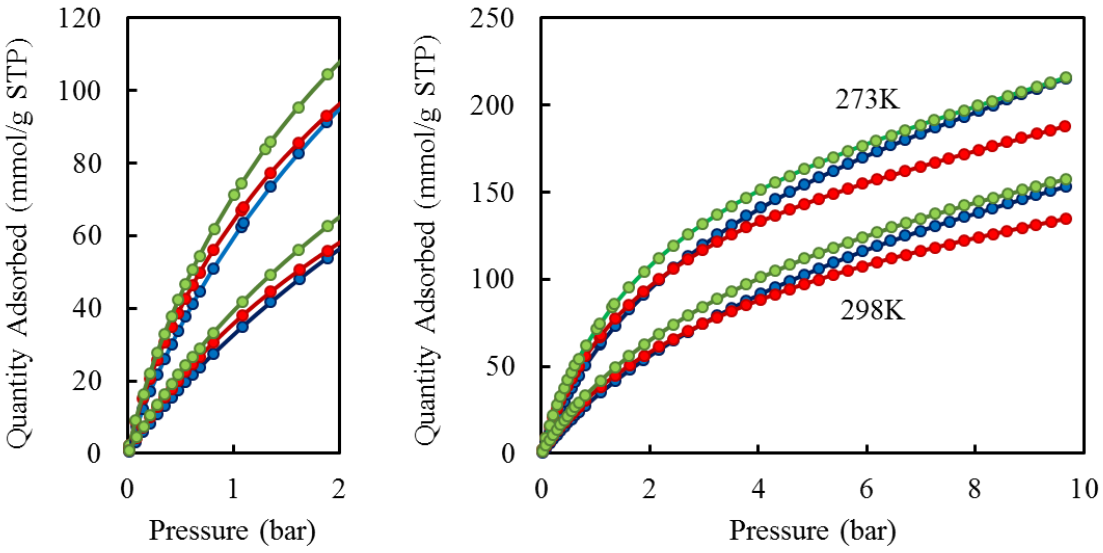

Figure 7. Carbon dioxide adsorption isotherm branches of TPAF (blue), TPAF-OH (red) and TPAF-NH_2 (green) measured at 273 and 298 K. Inset: enlargement of the low pressure region of isotherms.

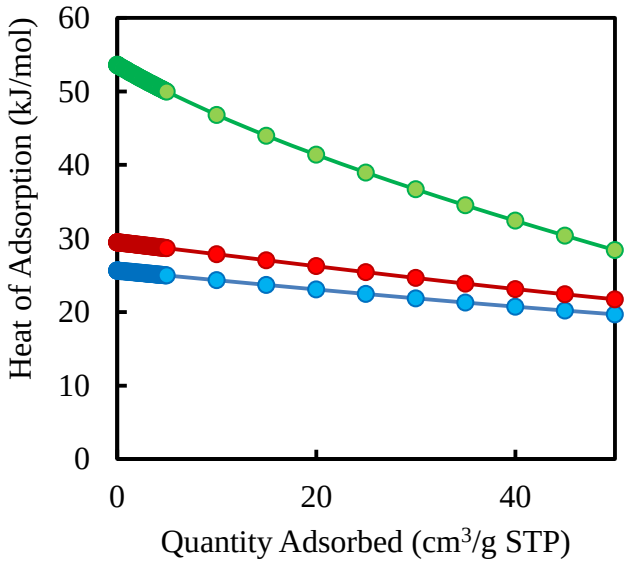

Figure 8. Isosteric heat of adsorption of CO_2 calculated for TPAF-H (blue), TPAF-OH (red) and TPAF-NH_2 (green)

The high value of isosteric heat of adsorption calculated for TPAF-NH_2 encouraged us to perform a detailed study of the interactions between the guest phase and the pore walls. The sample has been loaded in an NMR rotor, degassed and filled with ^{13}C-enriched carbon dioxide and an *in situ* solid state NMR study has been carried out at different temperatures. 2D ^{1}H-^{13}C heterocorrelated MAS NMR provides the spectroscopic observation of the intimate spatial relationship between the CO_2 guest molecules and the amino groups exposed on the cavity walls in the porous matrix. The spectrum recorded at 215 K displays through-space cross-correlations between the hydrogen atoms of the matrix and ^{13}C-enriched CO_2 carbons that resonate at 125.1 ppm. CO_2 is in the slow exchange regime with the functional groups on the matrix walls, and spent a relatively long time over an individual site that generates an efficient magnetization transfer by dipole–dipole interactions that took place at distances as short as 5–10 Å. In the 2D-heterocorrelated spectrum, the hydrogen of NH_2 groups and of nearby aromatic moieties correlate with CO_2 carbons, indicating that the CO_2 molecules sit in close contact with the these groups. These results provides clear evidence of highly energetic binding of CO_2 inside the porous matrix.

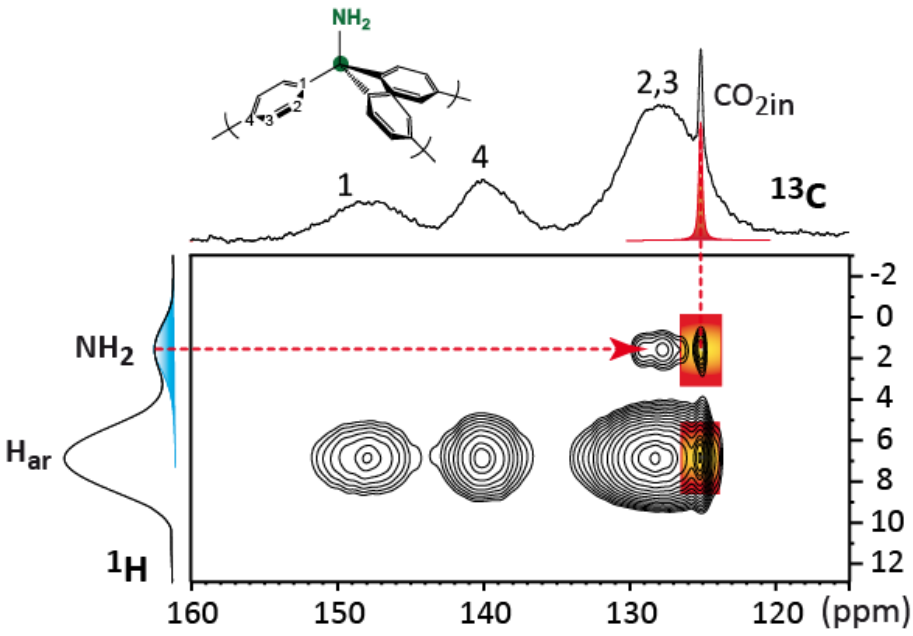

Figure 9. 2D ^{1}H-^{13}C HETCOR MAS solid state NMR of TPAF-NH_2 measured after loading ^{13}C-enriched CO_2 at 215 K with a contact time of 5 ms.

3.1.3.3. Methane adsorption properties

The CH_4 adsorption measurements have been collected up to 10 bar and at various temperatures (273, 283 and 298 K). The binding energies at low coverage exhibit values of 18 kJ/mol and 19 kJ/mol for TPAF and TPAF-NH_2, respectively, and up to 21 kJ/mol for TPAF–OH due to stronger electrostatic interactions and the smaller average mean size of pores. The intermolecular interactions can be further increased by generating charged lithium alkoxyde moieties inside TPAF-OH with a post-synthetic treatment with lithium hydride in THF (TPAF-OLi). It shows excellent CH_4 binding energy reaching a value as high as 25 kJ/mol, that matches or even exceeds the performances of MOFs containing open metal sites as Ni-MOF-74 (21.4 kJ/mol) and HKUST-1 (17 kJ/mol).

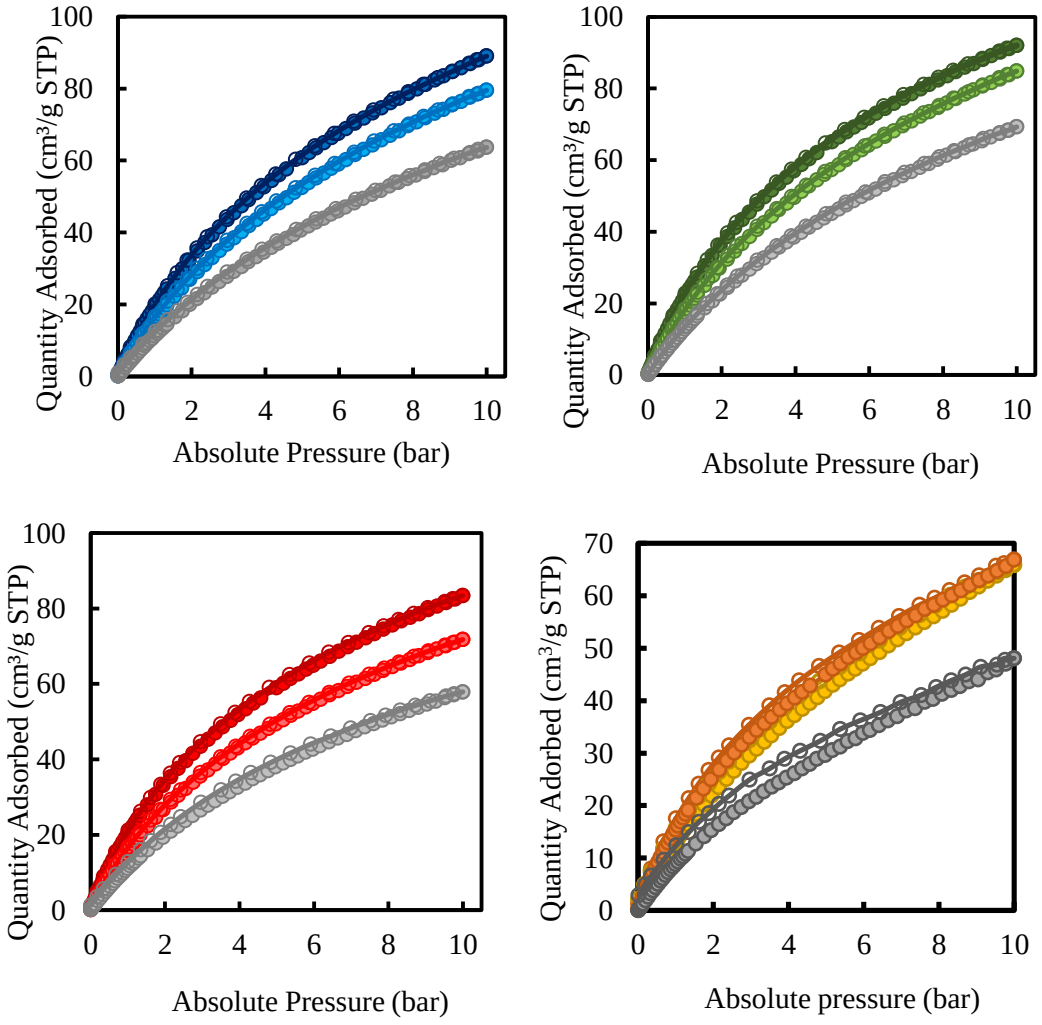

Figure 10. A) CH_4 adsorption isotherms of TPAF-H at 273 K (blue), 283 K (light blue) and 298 K (grey) measured up to 10 bar. B) CH_4 adsorption isotherms of TPAF-NH_2 at 273 K

(green), 283 K (light green) and 298 K (grey). C) CH_4 adsorption isotherms of TPAF-OH at 273 K (red), 283 K (light red) and 298 K (grey). D) CH_4 adsorption isotherms of TPAF-OLi at 273 K (orange), 283 K (yellow) and 298 K (grey).

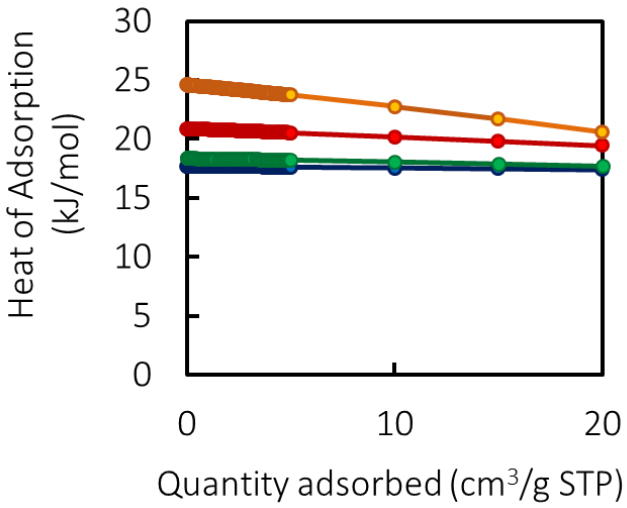

Figure 11. Isosteric heat of adsorption of CH_4 calculated for TPAF-H (blue), TPAF-OH (red), TPAF-NH_2 (green) and TPAF-OLi (yellow).

3.1.3.4. High pressure methane adsorption

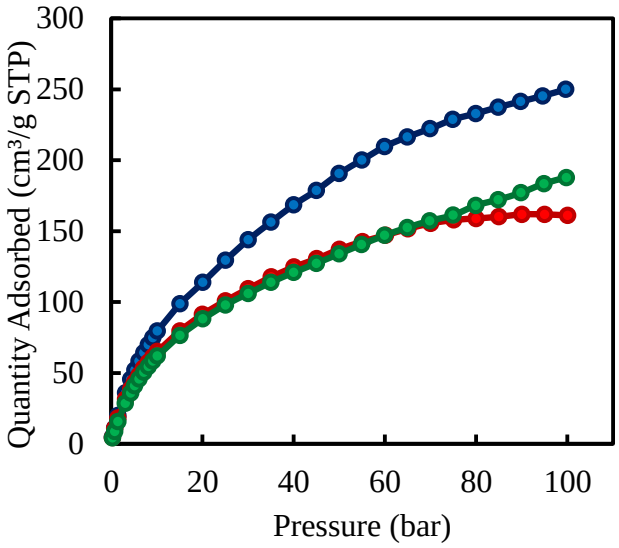

Figure 12. High pressure methane adsorption isotherms up to 100 bar for TPAF (blue), TPAF-OH (red) and TPAF-NH_2 (green).

High pressure methane isotherms up to 100 bar were collected on a Micromeritics HPVAII. The excess adsorbed quantity (methane excess isotherm) is directly measured and then converted to the total adsorption isotherm taking into account the contribution due to compressed methane inside the pores according to NIST data. At high pressures the maximum adsorption capacity is related to the pore volume inside the material: TPAF outperforms the other frameworks. The working capacity of the three samples has been evaluated in order to determine the properties of this materials for application in methane storage and adsorbed natural gas technology. The working capacities have been evaluated between different maximum pressures (35, 65 and 100 bar) and the minimum pressure of 5 bar and are summarized in the table below.

Table 3. Working capacities calculated for TPAF, TPAFNH_2 and TPAFOH.

Sample	Working capacity (cm^3/g; 5 – 35 bar; RT)	Working capacity (cm^3/g; 5 – 65 bar; RT)	Working capacity (cm^3/g; 5 – 100 bar; RT)
TPAF	106	154	200
TPAF-NH_2	73	112	147

TPAF-OH	75	110	118

3.1.4. Conclusion

3D aromatic frameworks (TPAFs) have been designed and synthetized starting from monomers with three rigid aromatic branches and a functional group connected to the tetrahedral core. This arrangement ensures the generation of a robust covalent scaff old, resistant to structural collapse, and regularly, homogeneously spaced organic functions all over the framework. The newly designed strategy satisfies the requirements for creating a framework that supports –OH, –NH2 and $–O^- Li^+$, which are constantly exposed inside the pores. The frameworks have been proved effective in capturing CO_2 and, especially, the amine derivative contains an energetic binding site in each monomer unit accounting for 54 kJ/mol, amongst the highest isosteric heat of adsorption reported in POFs. The direct spectroscopic observation of CO_2 over the sites has been provided by the magnetization transfer from amine hydrogens to CO_2 carbon nuclei through a short-distance dipolar interaction. Methane is a second target gas due to its importance in energy supply, since its transportation can cause concern on both large and small scales. Indeed, the functional materials proposed here exhibit relevant sorptive properties and excellent capacity, even in high-pressure regimes, owing to the balance between micro and meso-porosity. From the application point of view, it is worthwhile to mention the relatively low cost of triphenylmethane and its derivatives, which constitute the building blocks of the TAF frameworks.

3.1.5. Experimental details

Synthetic procedure

Tris(4-bromophenyl)methanol (1). *p*-dibromobenzene (8.7 g, 37.2 mmol) and freshly distilled THF (135 ml) have been added to a 2-neck round-bottom flask. The solution has been cooled to -78°C in a dry ice/acetone bath and *n*-BuLi (13.5 ml, 2.5 M in hexane 33.8 ml) has been added dropwise. After 3 h, the solution has been transferred in a 2-neck round-bottom flask cointaning diethyl carbonate (1.02 ml, 8.5

mmol) dissolved in THF (3ml). The solution has been subsequently warmed to room temperature. After 6 h, the reaction has been quenched with saturated aqueous NH_4Cl (50 ml). The crude product has been extracted with EtOAc (3x50 ml). The organic fractions have been collected, washed with brine and evaporated to dryness. At the crude oil was added hexane (60 ml) gently heated and sonicated to given a white solid, collected with filtration to yield 3.38 g (80%). H^1 NMR (300 MHz, $CDCl_3$): 7.45 (dd, 6H), 7.12 (dd, 6H), 2.70 (s, 1H).

Tris(4-bromophenyl)methane (2). **1** (1.25 g, 2.52 mmol) has been added to a 50 ml round-bottom flask equipped with a stirbar. Formic acid (95% in H_2O, 25 ml) has been added. A condenser has been attached and the solution heated to 100°C for 19 h to give a yellow suspension. The reaction has been quenched with a satured solution of Na_2CO_3 (100 ml). The aqueous suspension has been washed with diethyl ether (3x40 ml) and the combined organic phases were washed with brine and evaporated. The resulting solid has been purified with a plug of SiO_2 in pentane, to isolated 2 (0.89 g, 74% yield) as a white crystalline solid. H^1 NMR (300 MHz, $CDCl_3$): 7.42 (dd, 6H), 6.93 (dd, 6H), 5.40 (s, 1H).

Tris(4-bromophenyl)methylamine (3). **1** (2 g, 4.03 mmol) and anhydrous CH_2Cl_2 (20 ml) have been added to a 2-neck round-bottom flask. The solution has been cooled to 0°C and fresh distilled $SOCl_2$ (2 ml) added dropwise under vigorous stirring. After 5 h, the solvent has been evaporated, the resulting solid diluted in anhydrous toluene (25 ml) and added dropwise to a satured solution of NH_4Cl in 25% of aqueous ammonia (25 ml) at 0°C. Then, the reaction has been stirred for 24 h at 20°C and the organic phase has been separated, dried and evaporated. Hexane (20 ml) has been added to the crude oil and sonicated for 30 minutes. The white solid has been collected by filtration and dried. Pure **3** (1.046 g, 52.6% yield) can be obtained by precipitation of its hydrochloride salt. H^1 NMR (300 MHz, $CDCl_3$): 7.42 (dd, 6H), 6.93 (dd, 6H), 4.5 (s, 2H).

General procedure for framework synthesis (Yamamoto coupling)

The catalytic mixture was prepared by adding *cis*,*cis*-1,5-cyclooctadiene (1 ml), 2,2'bypiridyl (1g) and $Ni(COD)_2$ (2 g) in freshly distilled DMF (180 ml) and THF (60 ml) and stirred at 0°C for 10 minutes. The porous polymers have been obtained by adding dropwise the monomer (0.800 g) dissolved in THF (60 ml), to the catalytic mixture and the resulting mixture has been stirred at room temperature for 48 h. The reaction has been quenched by adding concentrated HCl (30 ml) until the solution turned blue-green with a white suspension. The product was filtered and washed with THF (3x30 ml), water (3x30 ml) and chloroform (3x30 ml) and dried in a vacuum at 170°C to obtain the activated solid.

3.1.6. References

[1] https://climate.nasa.gov/climate_resources/24/graphic-the-relentless-rise-of-carbon-dioxide/

[2] Mitchell, J. F. B.; Reviews of Geophysics, **1989**, *27*, 115 – 139.

[3] Yu, K. M. K., Curcic, I., Gabriel, J. and Tsang, S. C. E.; ChemSusChem, **2008**, *1*, 893 – 899.

[4] Doney, S. C., Fabry, V. J., Feely, R. A. and Kleypas, J.A.; Ann. Rev. Mar. Sci., **2009**, *1*, 169 – 192.

[5] D'Alessandro, D. M., Smit, B. and Long, J. R.; Angew. Chem. Int. Ed., **2010**, *49*, 6058 – 6082.

[6] Li, J.-R., Ma, M., McCarthy, M. C., Sculley, J., Yu, J., Jeong, H.-K., Balbuena, P. B. and Zhou, H.-C.; Coordination Chemistry Reviews, **2011**, *255*, 1791 – 1823.

[7] Markewitz, P., Kuckshinrichs, W., Leitner, W., Linssen, J., Zapp, P., Bongartz, R., Schreibera, A. and Müller, T. E.; Energy Environ. Sci., **2012**, *5*, 7281 – 7305.

[8] Rochelle, G. T., Science, **2009**, *325*, 1652 – 1655.

[9] Wang, Q., Luo, J., Zhong, Z. and Borgna, A.; Energy Envorn. Sci., **2011**, *4*, 42 – 55.

[10] Li, Y., Ben, T., Zhang, B., Fu, Y. and Qiu, S.; Scientific Reports, **2013**, *3*, 2420, 1 - 6.

[11] Lu, W., Sculley, J. P., Yuan, D., Krishna, R., Wei, Z. and Zhou, H.-C.; Angew. Chem. Int. Ed., **2012**, *51*, 7480 – 7484.

[12] Lu, L., Verdegaal, W. M., Yu, J., Balbuena, P. B., Jeong, H.-K. and Zhou, H.-C.; : Energy Environ. Sci., **2013**, *6*, 3559 – 3564.

[13] Chang, Z., Zhang, D.-S-, Chen Q. and Bu, X.-H.; Phys. Chem. Chem. Phys., **2013**, *15*, 5430 – 5442.

[14] Patel, H. A., Je, S. H., Park, J., Chen, D. P., Jung, Y., Yavuz, C. T. and Coskun, A.; Nat. Commun., **2013**, *4*, 1357.

[14] Sanz-Perez, E. S., Murdock, C. R., Didas, S. A. and Jones, C. W.; Chem. Rev., **2016**, *116*, 11840 − 11876.

[15] Dawson, R., Cooper, A. I. and Adams, D. J.; Polym. Int., **2013**, *62*, 345 – 352.

[16] Je, S. H., Buyukcakir, O., Kim, D. and Coskun, A.; Chem, **2016**, *1*, 482 – 493.

4. CO_2 adsorption and solid state reactivity of MOFs

4.1. Metal-organic frameworks based on bicyclo[1.1.1]pentane dicarboxylic acid (BCP)

4.1.1. Summary

Two MOFs based on the rigid yet aliphatic ligand bicyclo [1.1.1] pentane-1,3-dicarboxylic acid (BCP) have been synthetized using zinc or zirconium salts to obtain two materials isoreticular to MOF-5 and UiO-66 [1,2,3], Zn-BCP and Zr-BCP, respectively. These materials display Langmuir surface areas as high as 2700 and 1020 m^2/g and their adsorption behaviour towards carbon dioxide has been evaluated at high pressure (up to 10 bar) and different temperatures. Powder x-ray diffraction, infrared spectroscopy, solid state NMR, SEM microscopy and thermal analyses have been applied to study the structural and physical properties of these materials. Thermal and degradation properties of samples have been studied in detail and the solid-state reaction of the linkers has been observed under inert conditions.

4.1.2. ZnBCP and ZrBCP

4.1.2.1. Synthesis and structure of ZnBCP and ZrBCP

I select a rigid yet aliphatic ligand, bicyclo[1.1.1]pentan-dioic acid (BCP).

- The molecular structure is rigid due to the presence of a bi-cycloalkane moiety.
- The aliphatic linker provides a different electronic environment for the guest species compared to the usual electron-rich aromatic surrounding generated by phenyl moieties.

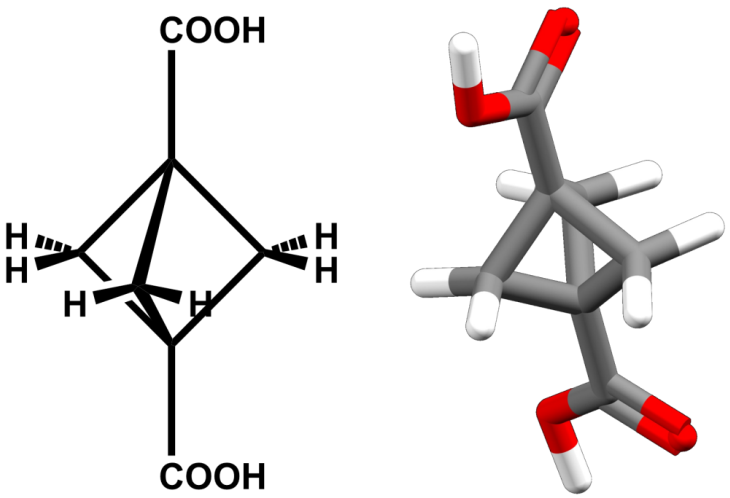

Figure 1. Chemical structure of bicyclo[1.1.1]pentan-dioic acid (BCP).

Two Metal Organic Frameworks have been developed isoreticular to the parent structures MOF-5 and UiO-66, Zn-BCP and Zr-BCP, respectively. Zn-BCP has been synthetized through a room temperature self-assembly process by mixing a solution of zinc acetate dihydrate with a solution containing the ligand in DMF under stirring (see Experimental details for further details). The BCP molecules displace the acetate ions and a white powder appears during the addition of the two solutions. After 30 minutes the agitation has been stopped and the mixture was left 16 h at room temperature. The white solid has been washed with dry DMF and dry dichloromethane was exchanged before activation at high temperature (130ºC) under high vacuum. Instead, Zr-BCP has been obtained under solvothermal conditions using a modulation approach: after optimization of experimental conditions, a highly nano-crystalline sample has been obtained adding 20 equivalents of formic acid as modulator (see Experimental details). The solid has been filtered and washed with DMF before activation at 140ºC under high vacuum.

The two solids were characterized *via* powder x-ray diffraction. PXRD patterns reveal the formation of highly crystalline materials and the comparison with the well-known experimental patterns of MOF-5 and UiO-66 suggest the formation of the desired structures. The crystal structures of the two MOFs have been simulated and the experimental powder x-ray diffraction patterns have been refined with Rietveld method by Dr. Charl Xavier Bezuidenhout. The crystal structures are reported below.

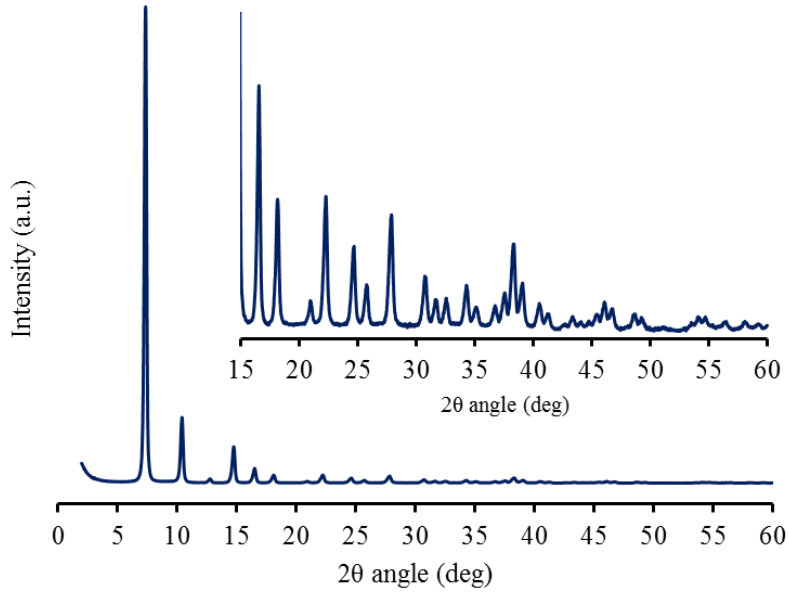

Figure 2. Powder x-ray diffraction pattern of Zn-BCP from 2 to 60 2θ degree. Inset: enlargement between 15 and 60 2θ degree.

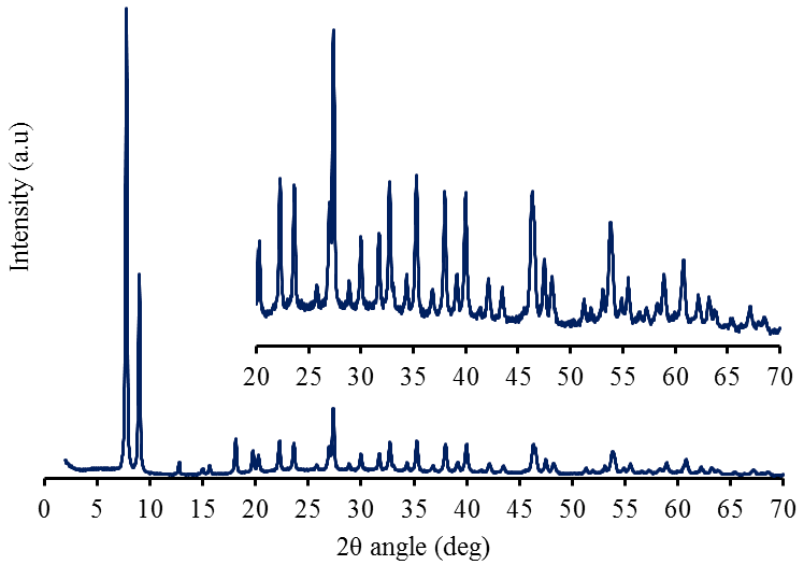

Figure 3. Powder x-ray diffraction pattern of Zn-BCP from 2 to 70 2θ degree. Inset: enlargement between 15 and 70 2θ degree.

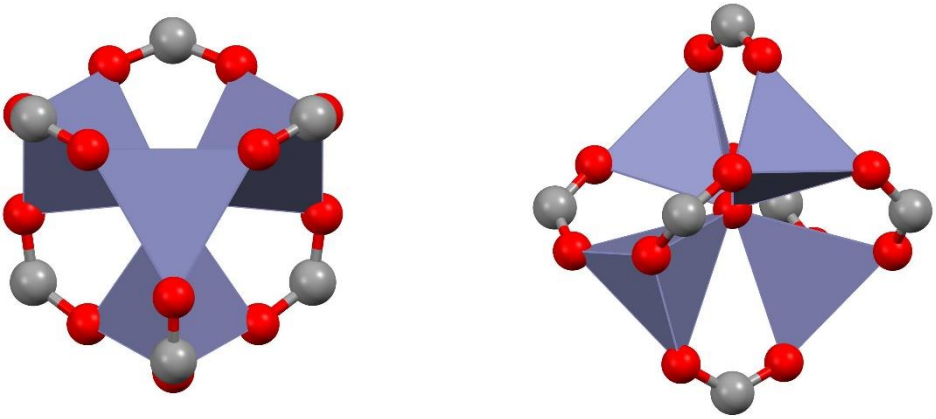

Figure 4. Secondary building unit (SBU) of Zn-BCP MOF. Left: top view of the SBU $Zn_4O(COO^-)_6$ (along the (a,b) plane). Right: side view of the SBU (along the c axis).

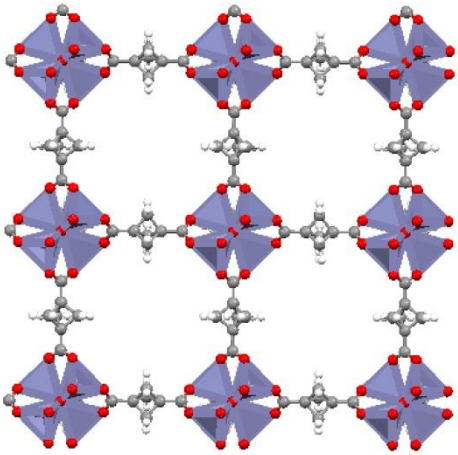

Figure 5. crystal structure of Zn-BCP MOF viewed along c axis.

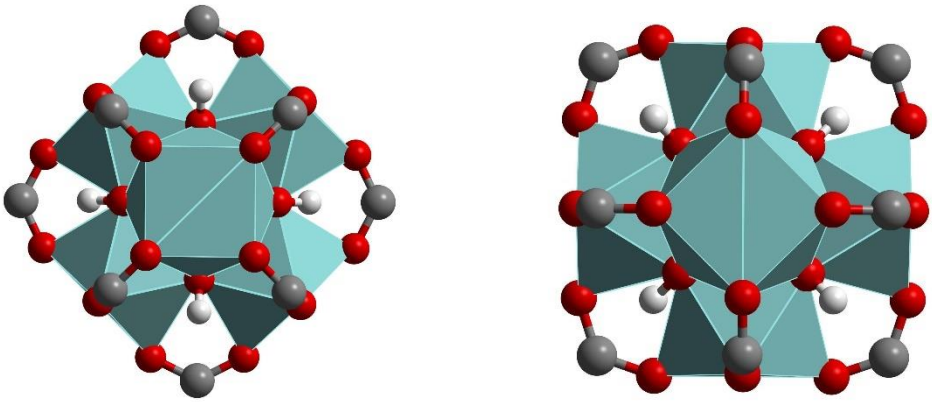

Figure 6. Secondary building unit (SBU) of Zr-BCP MOF. Left: top view of the SBU $Zn_6(\mu\text{-}O)_4$ $(\mu\text{-}OH)_4(COO^-)_{12}$ (along the (a,b) plane). Right: side view of the SBU (along the c axis).

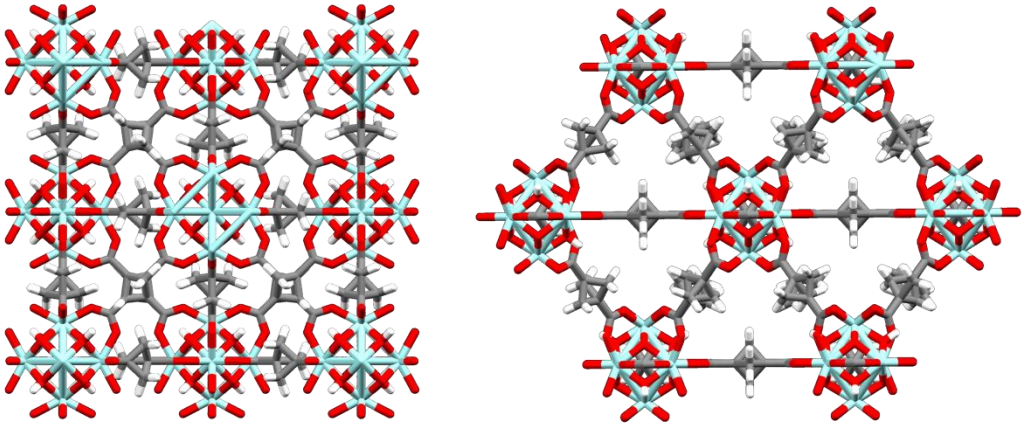

Figure 7. Crystal structure of Zr BCP along different axis.

The crystalline nature of the samples has been confirmed with scanning electron microscopy techniques. Zn-BCP is composed of cubic-shaped crystals with linear dimension between 10 nm to 500 nm, while Zr-BCP particles display an octahedral morphology and linear dimension in the range from 50 nm to 500 nm.

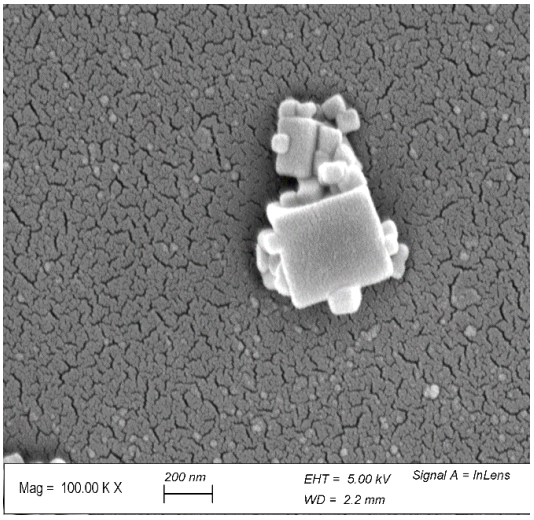

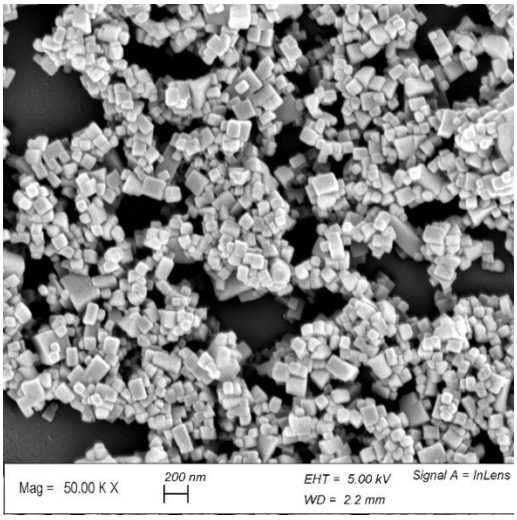

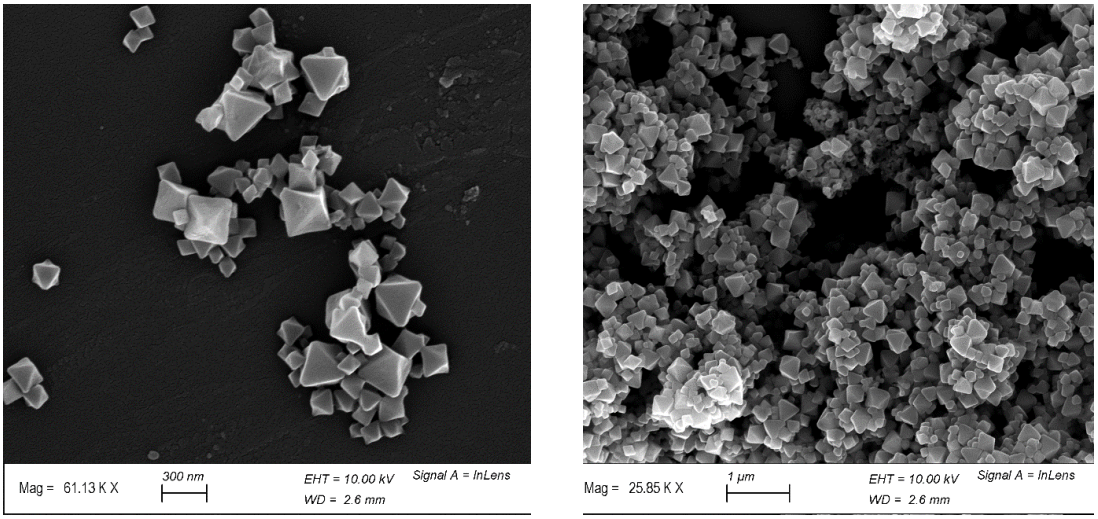

Figure 8. Scanning electron microscopy images of Zn-BCP (above) and Zr-BCP (below) at different magnifications. Zn-BCP displays a cubic habit while Zr-BCP nanocrystals shows an octahedral shape.

The chemical purity of the two MOFs has been assessed through dissolution of the bulk sample in a solution of deuterated dimethylsulfoxide/trifluoroacetic acid (DMSO_d_6:TFA_d = 0.8 ml: 0.15 ml, see Experimental Methods for details) and measurement of the ^{1}H liquid NMR spectrum of the digested MOF. Liquid ^{1}H NMR spectrum of Zn-BCP displays only the signal related to the hydrogen atoms on the aliphatic carbons; instead, the NMR spectrum of Zr-BCP shows the maintenance of formic acid in the final structure due to its competitive coordination to the metal cluster during MOF synthesis. The chemical composition obtained from this experiment is reported in tables below.

Table 1. Chemical shifts and assignments of liquid ^{1}H NMR spectrum of dissolved Zn-BCP.

Chemical Shift (ppm)	**Assignments**
2.14	C**H**$_2$, *s* (BCP)
2.50	DMSO, *quintet* solv. residual peak
15.8	TFA,*s* solv. residual peak

Table 2. Chemical shifts and assignments of liquid ^{1}H NMR spectrum of dissolved Zr-BCP. The carboxylic acid hydrogens of BCP and formic acid can't be detected due to deuterium exchange.

Chemical Shift (ppm)	Assignments
2.13	C**H**$_2$, *s* (BCP)
2.50	DMSO, *quintet* solv. residual peak
8.05	C**H**, *s* (formic acid)
16.0	TFA, *s* solv. residual peak

The composition has been calculated by integrating the peaks related to each chemical species in the ^{1}H liquid NMR spectrum accounting for the multiplicity of each hydrogen atoms inside different molecules. The molar ratio between formate anions and BCP inside Zr-BCP structure can thus be evaluated as shown below:

$$\frac{I_{FORM}}{I_{BCP}} = \frac{FORM}{BCP} m_R = 0.16$$

where:

$I_{FORM} = integral\ value\ of\ peak\ centered\ at\ 8.05\ ppm$

$I_{BCP} = integral\ value\ of\ peak\ centered\ at\ 2.13\ ppm$

$\frac{FORM}{BCP} m_R$ = *molar ratio between formic acid and BCP moieties in solution*

The experimental ^{1}H liquid state NMR spectra are reported below.

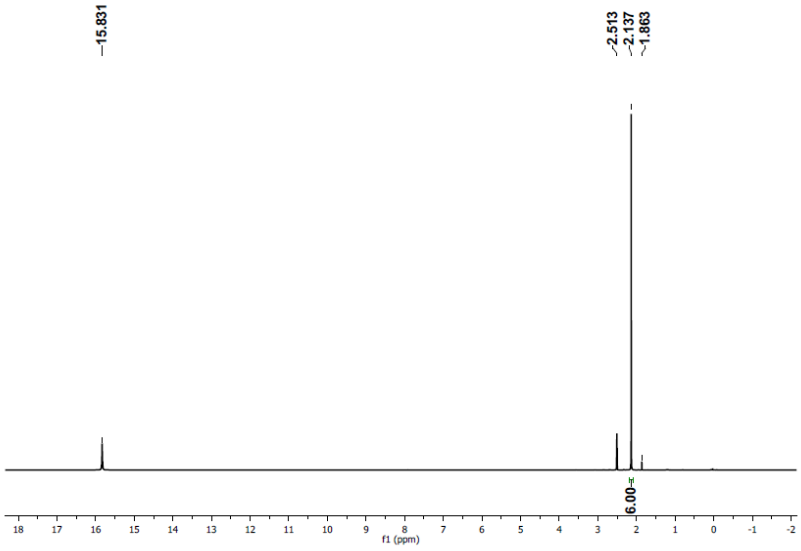

Figure 9. ^{1}H NMR of digested Zn-bcp metal organic framework in TFA_d/DMSO_d$_6$ solution (0,15/0,8ml). The hydrogen atoms of bcp moiety peaks at 2.14 ppm. A small signal at 1.86 ppm is due to a small amount of residual acetate ions inside the structure.

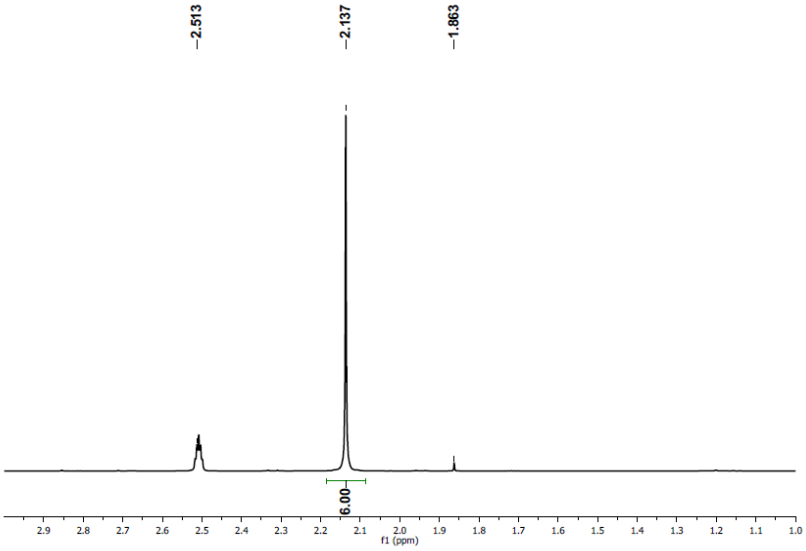

Figure 10. ^{1}H NMR of digested Zn-bcp metal organic framework in TFA_d/DMSO_d$_6$ solution (0,15/0,8ml) between 1 and 3 ppm.

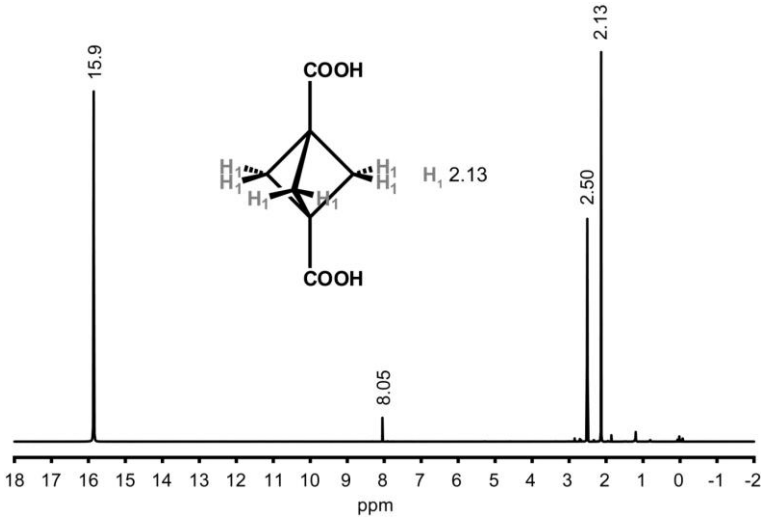

Figure 11. ^{1}H NMR of digested Zr-bcp metal organic framework in TFA_d/DMSO_d$_6$ solution (0,15/0,8ml). The hydrogen atoms of bcp moiety peaks at 2.13 ppm. The signal at 8.04 ppm is related to residual formate anions inside the MOF structure: from the relative integral value we could calculate that the MOF contains 1 formic acid molecule every 5 bcp ligand moieties.

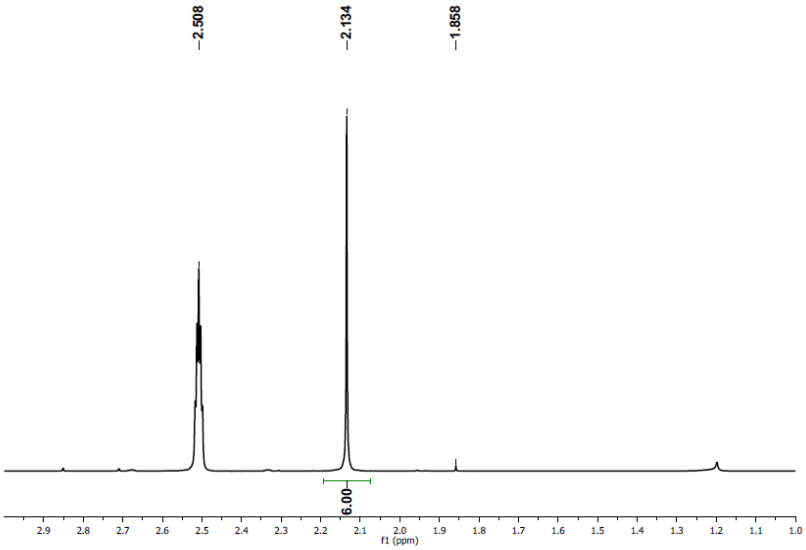

Figure 12. ^{1}H NMR of digested Zr-bcp metal organic framework in TFA_d/DMSO_d_6 solution (0,15/0,8ml) between 1 and 3 ppm.

4.1.2.2. Adsorptive properties of ZnBCP and ZrBCP

The porosity of the activated samples has been tested by collecting the nitrogen adsorption isotherms at 77 K. The two isotherms display type I adsorption behaviour (Langmuir isotherm) without any hysteresis during desorption branches typical of microporous solids. Zn-BCP displays a steep rise in the adsorption isotherm at low relative pressures: Langmuir and BET surface areas were calculated as high as 2700 m^2/g and 2400 m^2/g. The adsorption branch has been modelled according to DFT theory in order to calculate the pore size distribution (PSD) derived from adsorption data. The PSD display a sharp peak at 10.9 Å.

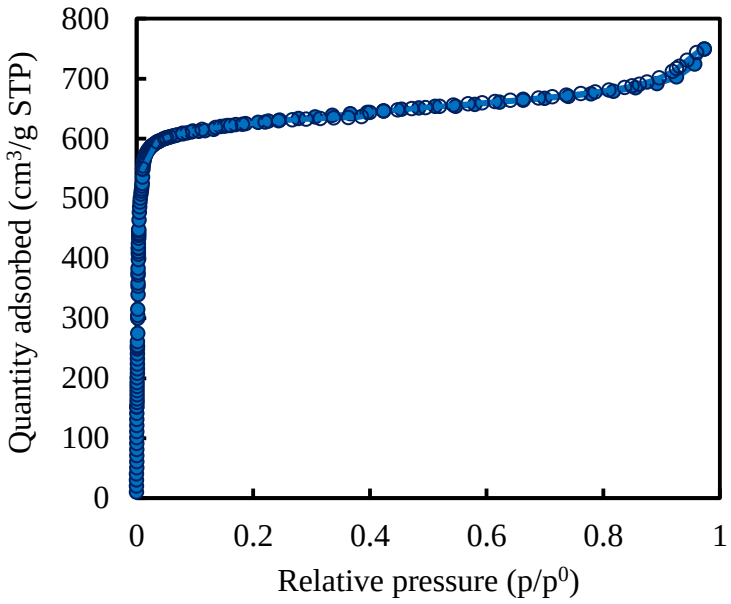

Figure 13. Nitrogen adsorption isotherm of sample Zn-BCP collected at 77K.

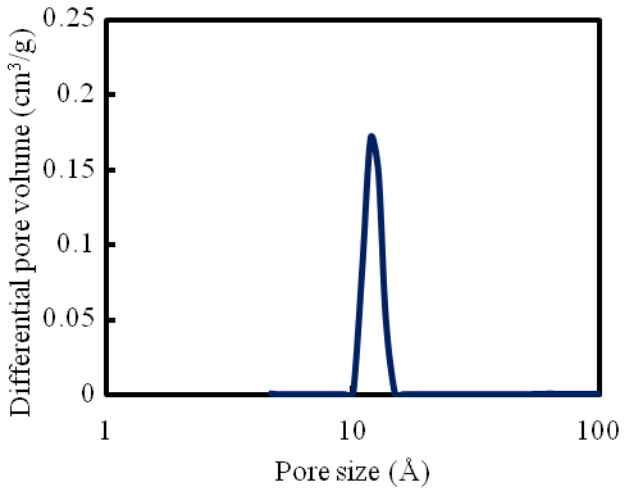

Figure 14. Pore size distribution between 1 and 100 Å of Zn-BCP calculated according to DFT method (logarithmic scale).

Zr-BCP adsorption isotherm displays a different behaviour at low pressure: a change in the adsorption isotherm slope around 0.001 p/pº suggests the presence of different pore sizes in the microporous region. Accordingly, the PSD peaks at 8.6 nm, a value in excellent agreement with the data calculated from the simulated structure, but presents also a broader distribution between 10 and 17 nm. This pore distribution

arises due to the formation of defects inside the crystal structure according to the liquid state NMR data and as discussed extensively in later session of this manuscript that generates connected cages inside the material. Instead, the smaller pore hosted inside the tetrahedral cage (4 Å) predicted by the simulated structure are not accessible to nitrogen at 77 K due to the small aperture of the accessible triangular window.

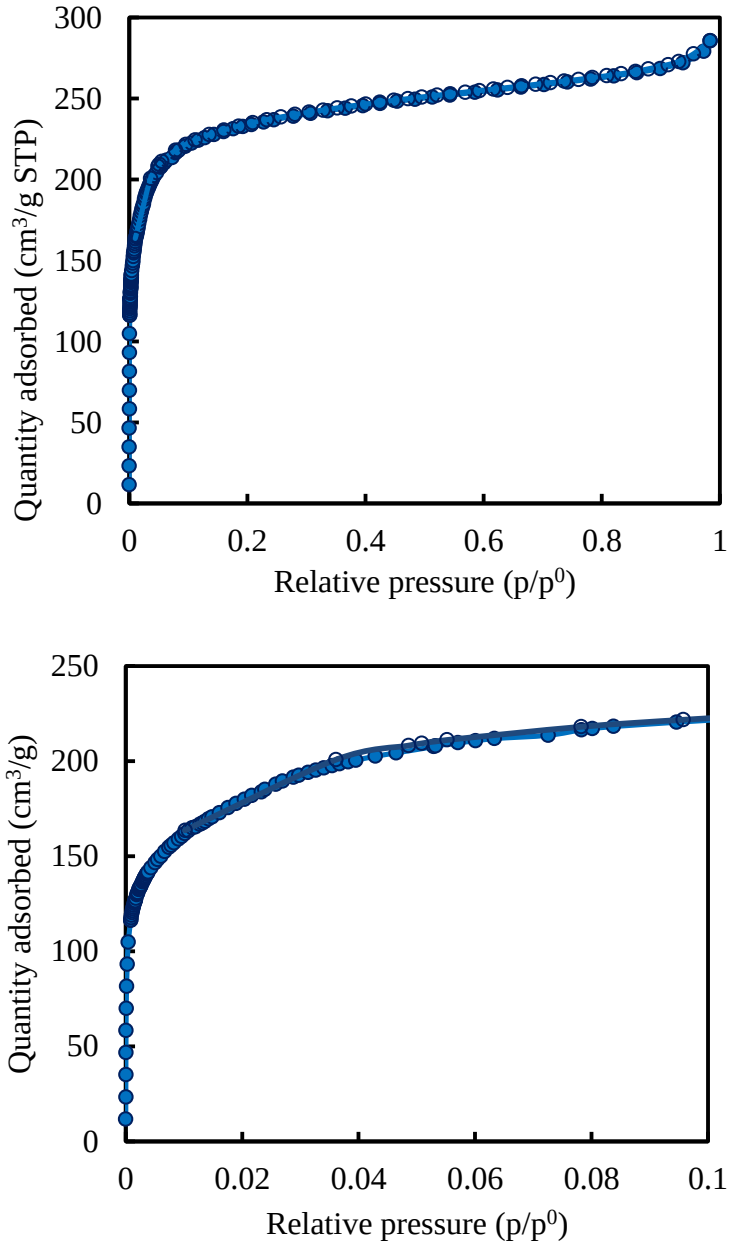

Figure 15. Top: nitrogen adsorption isotherm of sample Zr-BCP collected at 77K. Bottom: enlargement between 0 and 0.1 p/p°: the adsorption curve display a change in slope at uptakes higher than 120 cm^3/g.

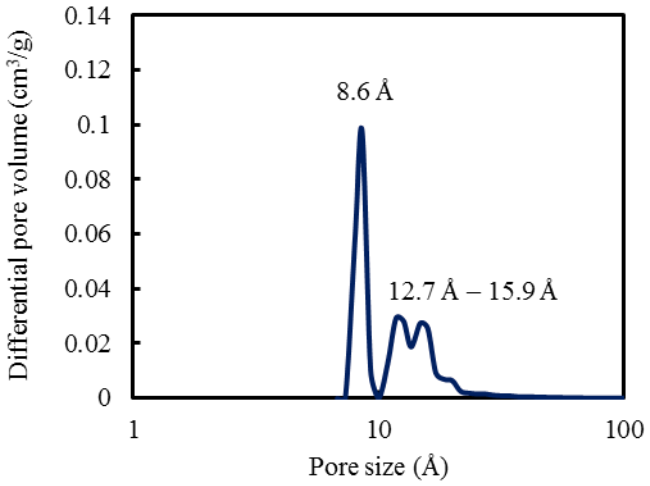

Figure 16. Pore size distribution (PSD) of Zr-BCP between 1 and 100 Å (logarithmic scale). The PSD has been calculated according to DFT method.

Carbon dioxide adsorption has been studied at 195 K. Zn-BCP display a linear uptake at low pressure; then, at $p/p^o = 0.11$ the adsorption curve display a steep slope and it gives rise to a S-shaped curve with a maximum uptake of 470 cm^3/g. This behaviour is similar to MOF-5 [4]: at low pressure only primary adsorption sites near the metal clusters are occupied by CO_2 molecules; at higher pressure carbon dioxide molecule interact with each other as well as secondary adsorption sites near the ligands and fill the cubic cavities inside the MOF structure. This behaviour is observed also at higher temperatures. The threshold pressure at which the slope of isotherms increases drift to higher values with increasing temperature and the slope itself becomes gentle: the higher thermal energy competes with the adsorption process. The isosteric heat of adsorption (Q_{st}) has been evaluated by fitting the isotherms at 263 K, 273 K, 283 K and 298 K with a triple site Langmuir model in order to model properly the S-shaped behaviour of the curve. Application of the Clausius-Clapeyron equation at constant uptake allows the calculation of the isosteric heat of adsorption. At low uptake Q_{st} is about 20.5 KJ/mol, while at about 100 cm^3/g, consistently with the start of increasing slope in the adsorption isotherms, it starts to raise and reaches values up to 25 KJ/mol.

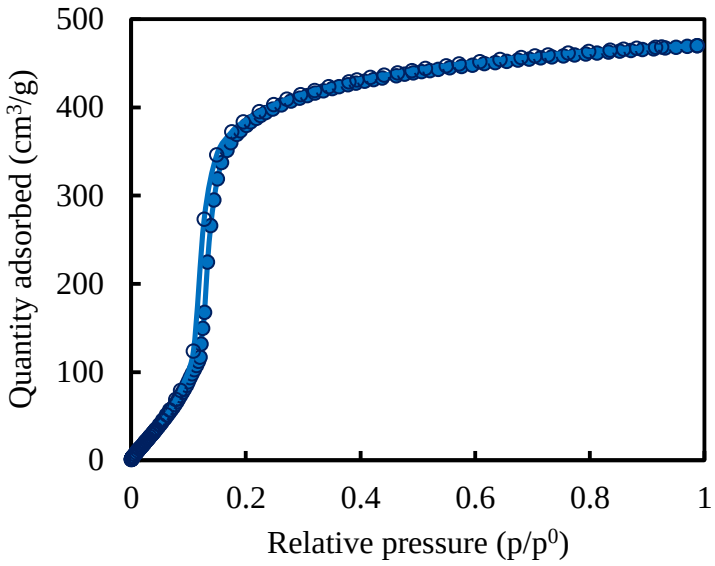

Figure 17. Carbon dioxide adsorption isotherms of Zn-BCP collected at 195 K.

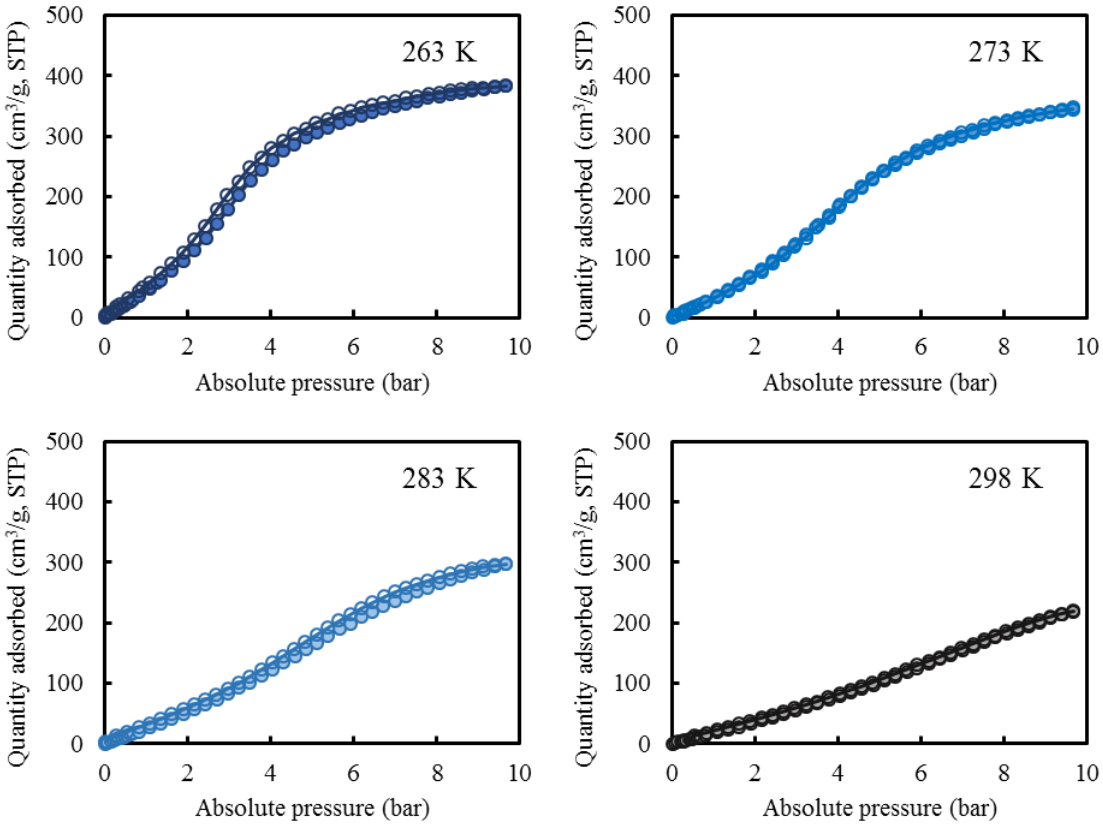

Figure 18. Carbon dioxide adsorption isotherms of Zn-BCP collected at different temperature: 263 K (dark blue), 273 K (blue) 283 K (light blue) and 298 K (grey).

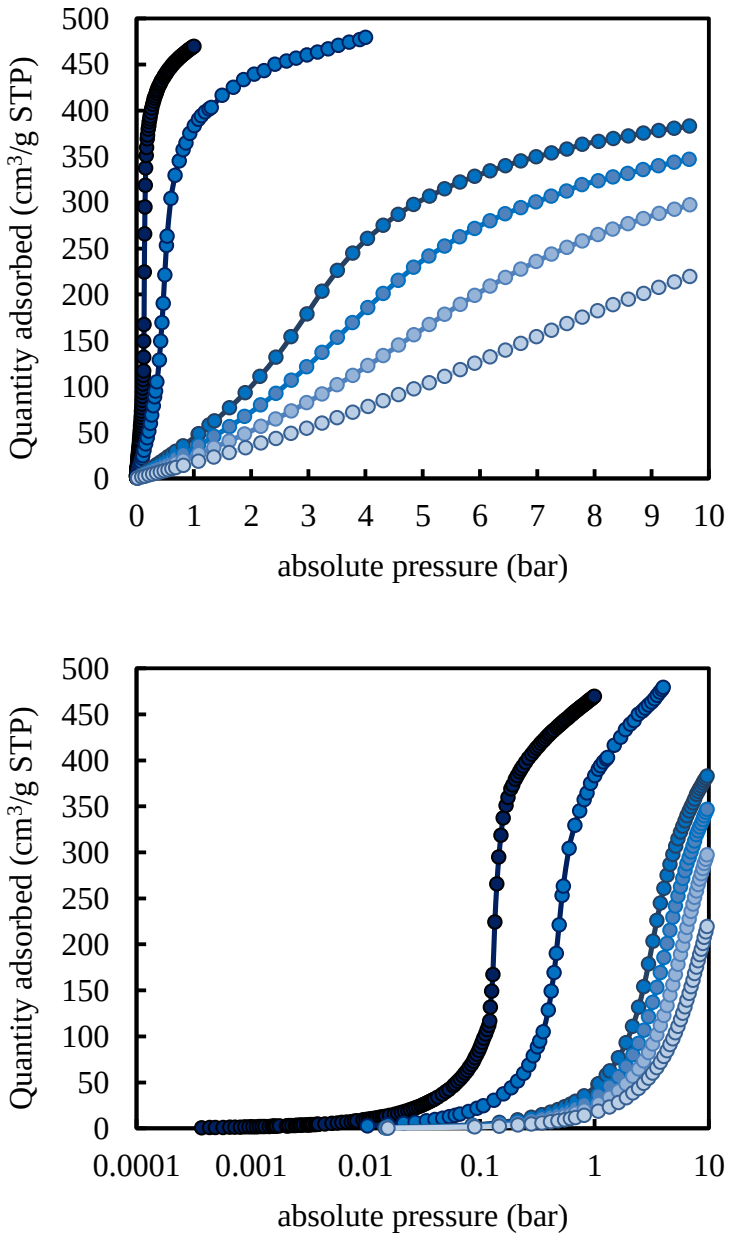

Figure 19. Adsorption branch of carbon dioxide adsorption isotherms of Zn-BCP collected at different temperature in natural and Log scale (195K, 218K, 263K, 273K, 283K and 298K).

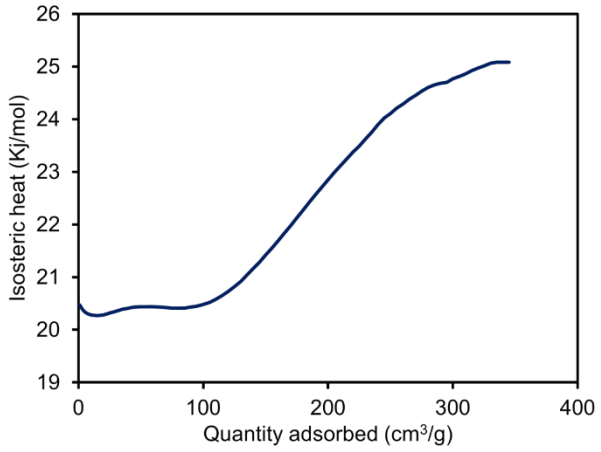

Figure 20. Isosteric heat of adsorption of Zn-BCP calculated from the isotherms collected at 263 K, 273 K, 283 K and 298 K.

Carbon dioxide adsorption isotherms at 195 K of Zr-BCP displays a bimodal slope due to the presence of smaller pores of 8.6 Å and a broader pore size distribution between 10 and 17 Å. High temperature carbon dioxide adsorption isotherms collected at 273 K, 283 K and 298 K have been fitted with a dual site Langmuir model and the isosteric heat of adsorption has been evaluated (figure 22, 23). At low coverage the interaction between carbon dioxide molecules and the primary sites located near the zirconium oxo-hydroxy cluster results in a higher heat of adsorption of about 31 KJ/mol, similar to the one reported for UiO-66; this value drops at higher loadings due to the saturation of primary adsorption sites.

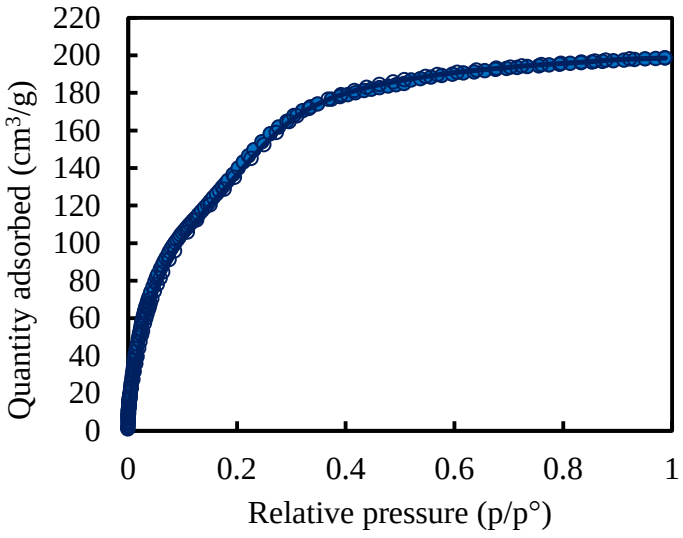

Figure 21. Carbon dioxide adsorption isotherms of Zr-FTR collected at 195K.

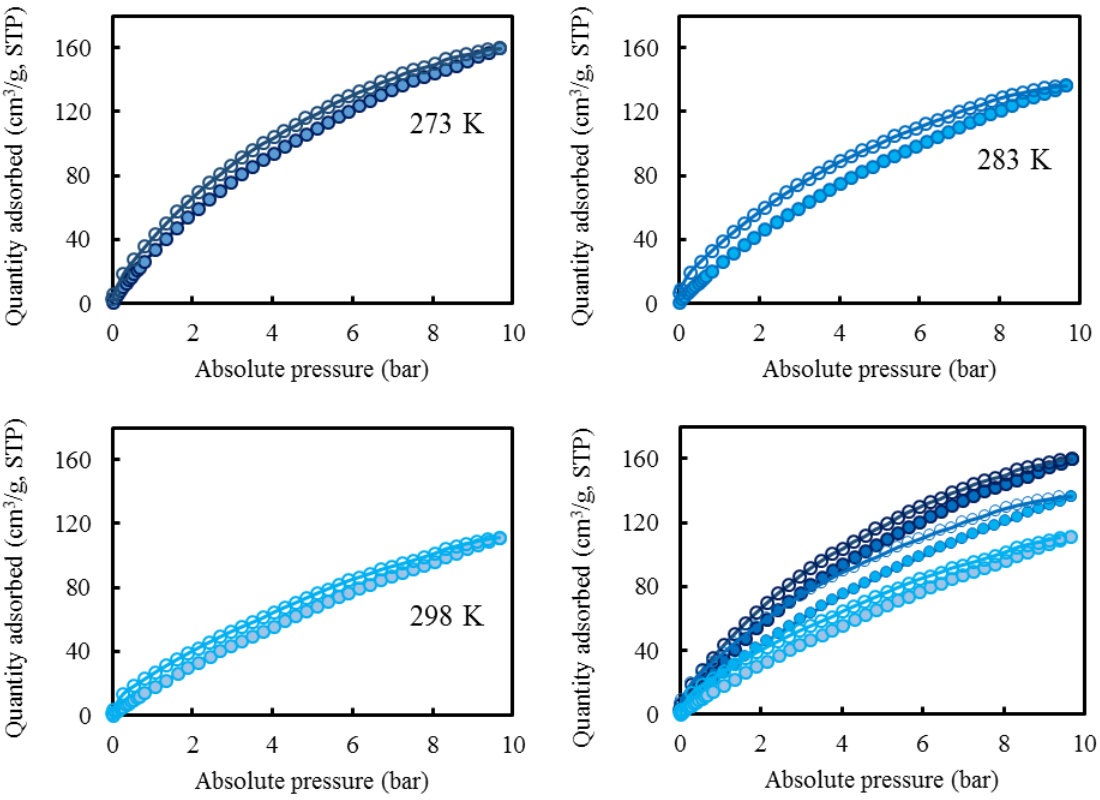

Figure 22. Carbon dioxide adsorption isotherms of Zr-BCP collected at high temperature (273K, 283K and 298K).

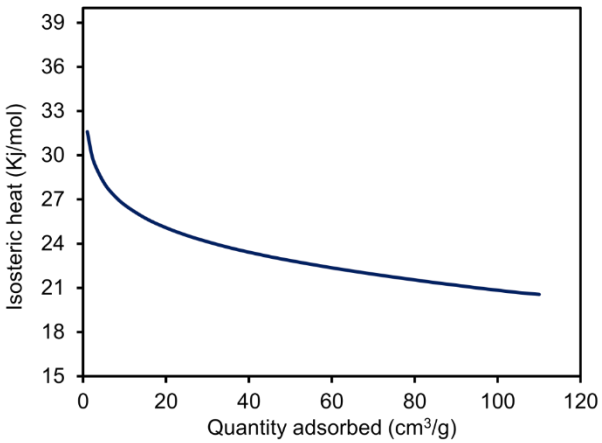

Figure 23. Isosteric heat of adsorption of Zr-BCP calculated from the isotherms collected at 273 K, 283 K and 298 K.

Methane adsorption isotherms at 273 K, 283 K and 298 K have been measured on Zn-BCP MOF: all isotherms display an almost linear behaviour up to 10 bar due to the low interactions between methane molecules and the pore walls as quantified calculating the isosteric heat of adsorption that reaches values of 17 KJ/mol at low loading and is almost steady up to an uptake of 60 cm^3/g.

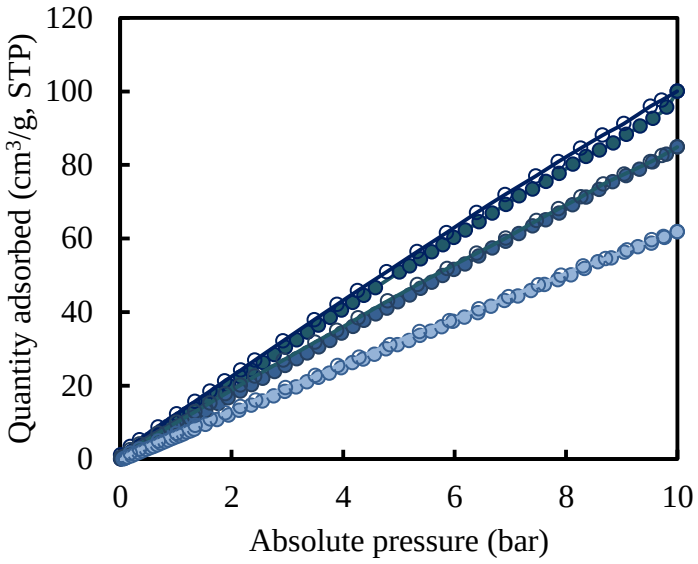

Figure 24. Methane adsorption isotherms of Zn-BCP collected at high temperature (273 K, dark blue; 283 K, blue; and 298 K, light blue).

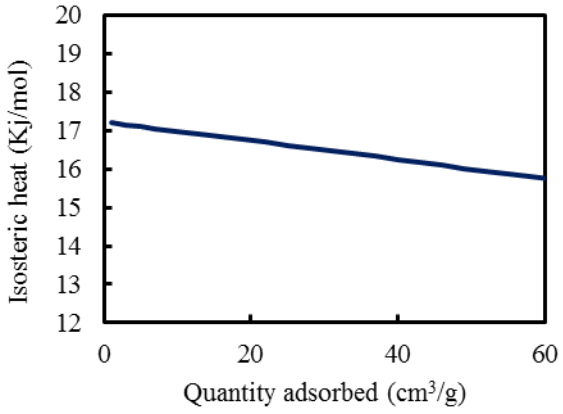

Figure 25. Isosteric heat of adsorption of methane for Zn-BCP calculated from the isotherms collected at 273 K, 283 K and 298 K.

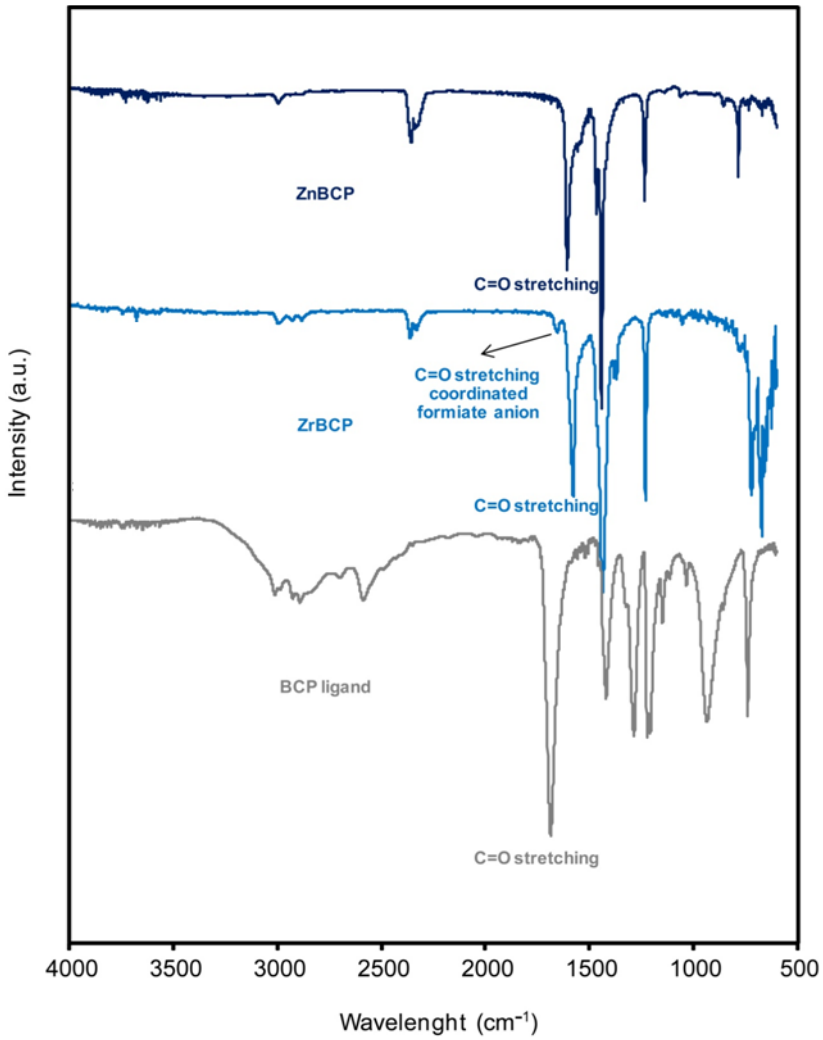

Figure 26. FT-IR spectra of Zn-BCP, Zr-BCP and the ligand BCP.

Infrared spectra of Zn-BCP and Zr-BCP display a shift of the O−C−O stretching band from 1684 cm^{-1} in the free ligand to 1609 cm^{-1} and 1580 cm^{-1} in Zn-based and Zr-based metal organic frameworks, respectively. The peak at 1652 cm^{-1} is assigned to the asymmetric O−C−O stretching of formic acid moieties coordinated to the zirconium cluster (in agreement with solid state NMR of Zr-BCP and liquid NMR of dissolved MOF).

4.1.2.3. Thermal properties of ZnBCP and ZrBCP

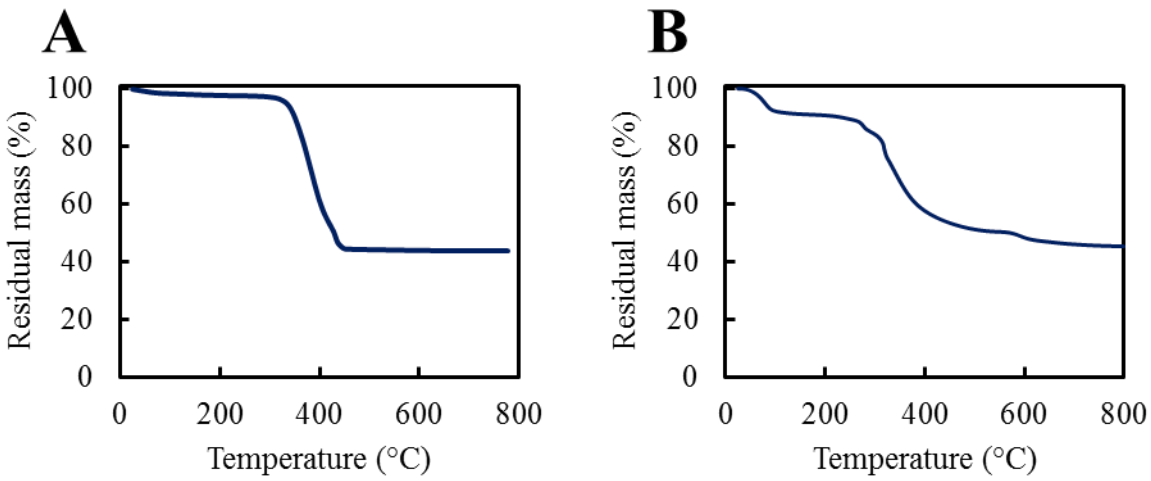

Figure 27. Thermogravimetric analysis of A) Zn-BCP and B) Zr-BCP under oxidative conditions (dry air).

Thermogravimetric analysis has been employed to evaluate the thermal stability of the samples. Zn-BCP and Zr-BCP are stable up to 315ºC under oxidative condition.

Zn-BCP displays a residual experimental mass of 43.8 % that matches the residual mass calculated from the unit formula due to the conversion of the MOF to ZnO (43.8 %) under oxidative conditions. Under inert atmosphere (nitrogen gas) the sample displays a different behaviour: during TGA analysis it is stable up to 370ºC, while DSC measurement shows an exothermic peak at 315ºC that is not related to any weight loss in TGA analysis. An in-depth study has been carried out to understand the process that takes place at high temperature: the sample (Zn-BCP) has been treated at 320°C for 30 minutes under inert atmosphere and the resulting off-white powder has been dissolved in a DMSO_d_6/TFA_d mixture and analyzed *via* ^{1}H liquid state NMR. The NMR spectrum display a dramatic change in the chemical shifts of the peaks associated to the ligand molecule. Two novel peaks at 5.49 ppm and 6.10 ppm appear suggesting the formation of carbon-carbon double bonds. The NMR spectrum is in excellent agreement with the spectrum reported for the expected molecule [5]. This result is supported by literature data that show the ring opening reaction of 1,3 substituted [1.1.1] bicyclopentane moiety occurring in gas phase at high temperature

[6]. Since the dicarboxylic acid itself sublimes at 260°C, the insertion of this moiety inside porous frameworks allows to perform the chemical transformation in the solid state and the final product can be potentially isolated easily by a simple work-up after the framework dissolution.

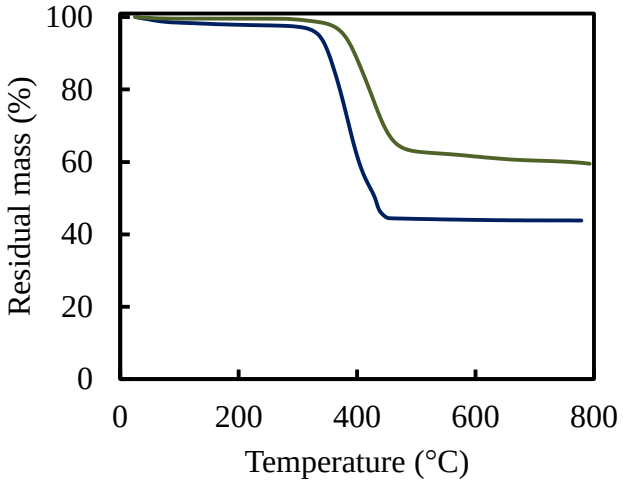

Figure 28. Thermogravimetric analysis of Zn-BCP under oxidative conditions (blue) and under nitrogen (inert atmosphere, grey) measured at a rate of 10 K/min.

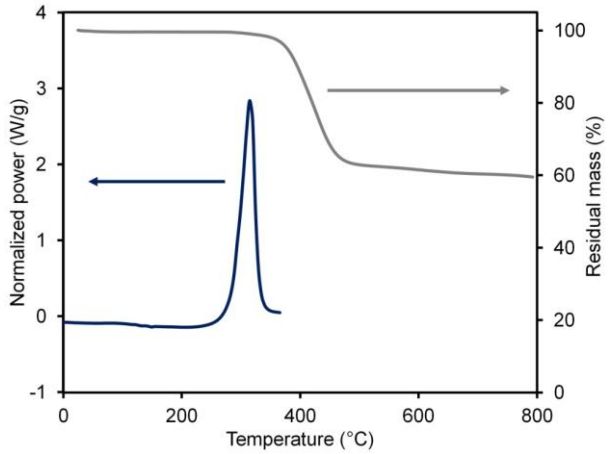

Figure 29. Thermogravimetric analysis of Zn-BCP under nitrogen (inert atmosphere, grey) and differential scanning calorimetry under nitrogen (blue) measured at a rate of 10 K/min.

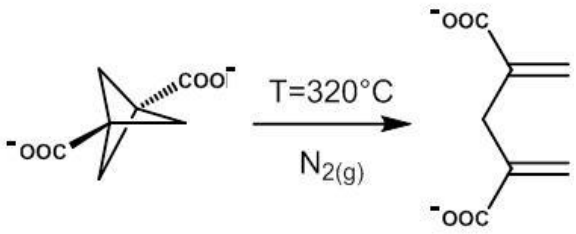

Figure 30. Scheme of the thermal ring opening reaction of the BCP linker inside the Zn-BCP MOF under inert atmosphere.

Thermogravimetric analysis of Zr-BCP under oxidative conditions displays a complex behaviour. Below 100ºC adsorbed water is released (weight loss = 9%); then, between 210ºC and 300ºC two different weight losses occur: these processes involve the desorption of acetic acid coordinated to the zirconium clusters and the high temperature rearrangement of the zirconium oxy-hydroxy clusters from $Zr_6(\mu_3\text{-}O)_4(\mu_3\text{-}OH)_4(COO_2)_6$ to its dehydrated form $Zr_6(\mu_3\text{-}O)_6(COO_2)_6$ according to the similar processes observed in UiO-66 [7].

$$Zr_6(\mu_3 - O)_4(\mu_3 - OH)_4(COO_2)_6 \rightleftarrows Zr_6(\mu_3 - O)_6(COO_2)_6 + 2\,H_2O$$

At 320ºC the sample degrades generating cubic ZrO_2 at high temperature. The residual experimental weight loss is 45.5%, close to the calculated one of 46.8% for the ideal structure.

Under nitrogen atmosphere the sample displays higher thermal stability up to 380ºC, while the DSC scan reveals an exothermic peak at 305ºC due to ligand rearrangement, similar to Zn-BCP.

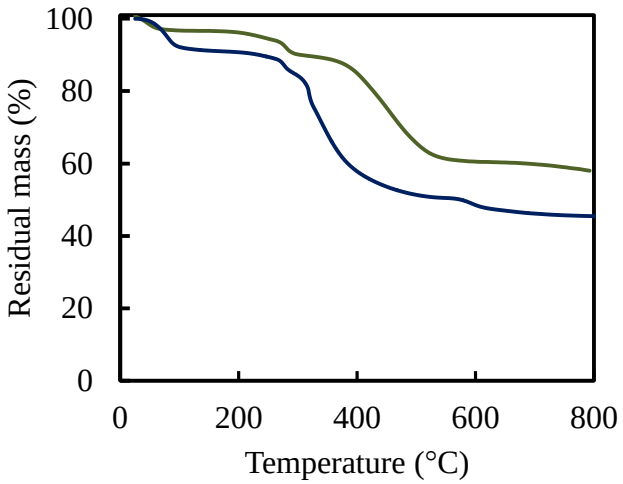

Figure 31. Thermogravimetric analysis of Zr-BCP under oxidative conditions (blue) and under nitrogen (inert atmosphere, grey) measured at a rate of 10 K/min.

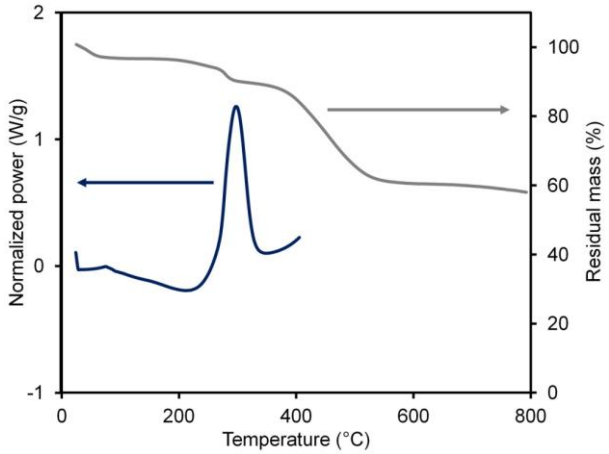

Figure 32. Thermogravimetric analysis of Zn-BCP under nitrogen (inert atmosphere, grey) and differential scanning calorimetry under nitrogen (blue) measured at a rate of 10 K/min.

4.1.2.4. Stability of ZnBCP and ZrBCP

The stability of the two MOFs has been tested. The empty Zn-BCP was exposed to moisture resulting in fast degradation processes. Infrared spectrum displayed the appearance of novel vibrational band centered at 1540 cm^{-1}. According to literature, this peak could be ascribed to a carboxylic acid interacting with a water molecule

through hydrogen bonding [8]. Moreover, a broad vibrational band between 3100 and 3600 cm^{-1} was due to hydrogen bonded O-H groups.

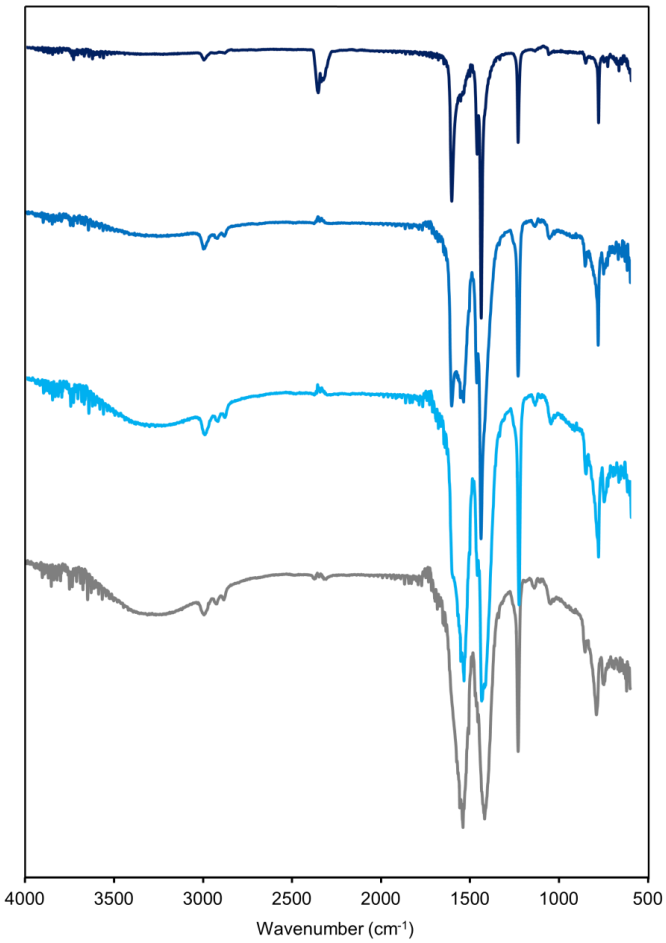

Figure 33. Infrared spectra of empty Zn-BCP (dark blue) and sample exposed to atmospheric moisture after 10 (blue), 20 (light blue) and 45 minutes (grey).

Exposure to atmospheric moisture quickly degrades the sample Zn-BCP: the crystallinity of the sample is quickly degraded during powder X-ray diffraction experiment.

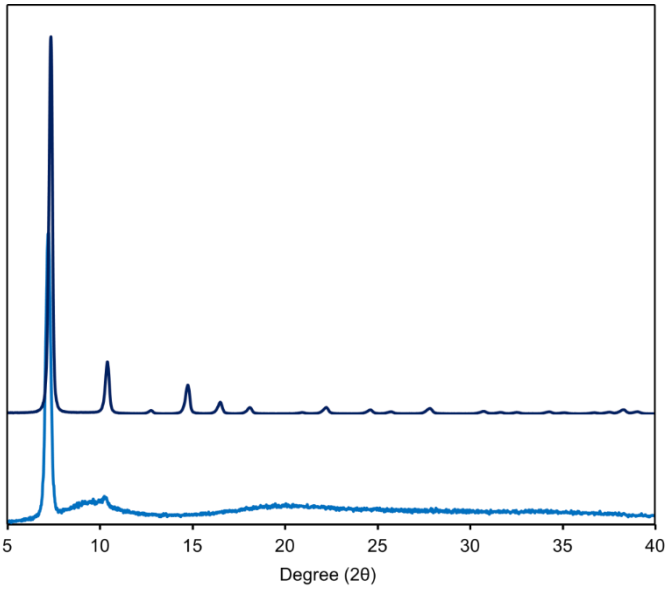

Figure 34. Powder x-ray diffraction pattern of pristine Zn-BCP (dark blue) and degraded sample (light blue).

Instead, ZrBCP displays high chemical stability in moist air and even when it is soaked in water. Powder x-ray diffraction patterns of evacuated Zr-BCP (140°C, overnight) (black); Zr-BCP exposed in air for 3 months and then evacuated at 140°C (blue) and a sample soaked in water for 24h and then dried at 140°C (grey) are perfectly matching. The sample mass does not show significative changes during water soaking experiment (starting mass: 60.4mg; recovered mass: 58.8mg).

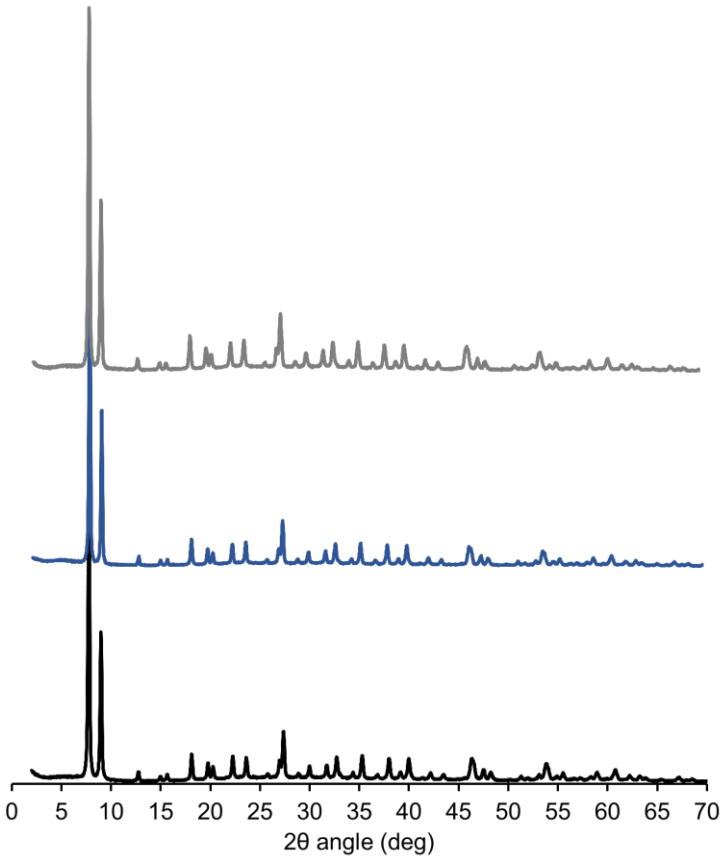

Figure 35. Powder x-ray diffraction pattern of evacuated Zr-bcp (black); Zr-bcp after exposure in air (3 months) and evacuation (blue) and water-soaked Zr-bcp after evacuation (grey).

4.1.3. Experimental details

All solvent (dry N,N'DMF, DCM and methanol) were reagent grade and used as received). 1,3-Bicyclo[1.1.1]pentanedicarboxylic acid (BCP) was purchased at fluorochem (95%)

Synthesis of Zn-BCP

A solution of $Zn(CH_3COO)_2 \cdot 2H_2O$ (197.56 mg; 0.90 mmol) in dry N,N'DMF (3 ml) was added dropwise to a solution of 1,3-Bicyclo[1.1.1]pentanedicarboxylic acid (46.84 mg; 0.30 mmol) in dry N,N'-DMF (3 ml) over a period of 5 minutes at room temperature under stirring. The mixture was additionally stirred for 30 minutes and

then left under static conditions for 16h. The white precipitate is centrifuged and fresh dry N,N'DMF was replaced 4 times (4 x 5 ml). The solvent was exchanged and soaked in dry DCM for 2 days replacing the solvent two times a day. The material was activated in high vacuum at room temperature for 8 h and then at 130°C overnight.

Synthesis of Zr-BCP

$ZrCl_4$ (144.6mg; 0.62mmol) and 1,3-Bicyclo[1.1.1]pentanedicarboxylic acid (290.4 mg; 1.86 mmol) were dispersed in a mixture of dry N,N'DMF (24 ml) and formic acid (456 µl; 12 mmol) in a 100 ml glass vial and the mixture was sonicated for 1 minutes at room temperature and then heated at 120°C for 22 h. Then the vial is taken out of the oven and cooled at room temperature. The white solid is filtered on a 0.2 µm PTFE filter and washed with N,N'DMF (100 ml) and methanol (100 ml). The resulting powder was activated in high vacuum first at room temperature and then at 140°C overnight.

Rietveld refinement and crystallographic data of Zn-BCP and Zr-BCP

Powder x-ray diffraction patterns have been refined by Dr. C. X. Bezuidenhout using the TOPAS-Academic-64 V6 software package.

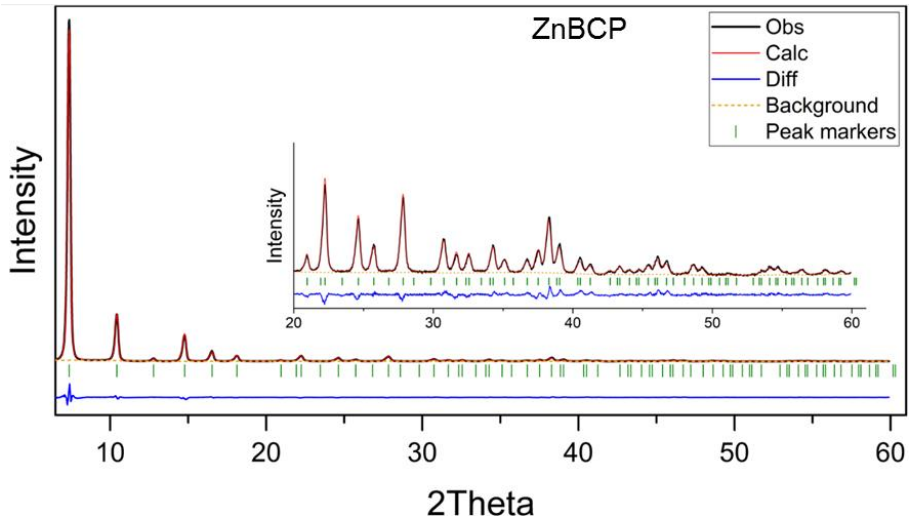

Figure 36. Rietveld fits of X-ray data for Zn-BCP. The HKL indices are indicated as green markers and the difference plot are shown below. The black and red represent the observed and calculated traces respectively while the dotted yellow line represent the background plot.

Table 2. Crystallographic data for the PXRD Rietveld refinement.

Identification code	**Zn-BCP**
Empirical formula	C1.75H1.5O1.083Zn0.333
Formula weight	61.67
Temperature/K	N/A
Crystal system	cubic
Space group	*F*-43*c*
a=b=c/Å	23.9551
Volume/Å^3	13746.56
Z	96
ρ_{calc}g/cm^3	0.71511
Rp	4.2 %
Rwp	5.9 %

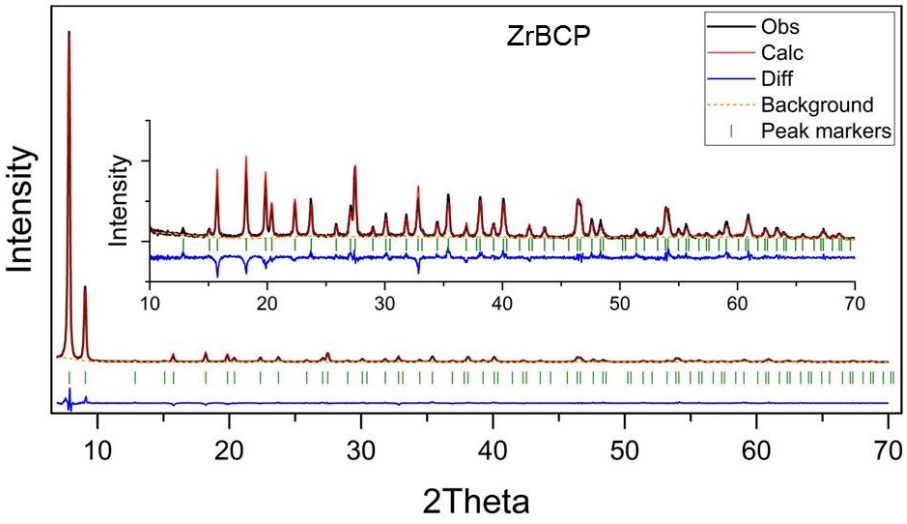

Figure 37. Rietveld fits of X-ray data for Zr-BCP. The HKL indices are indicated as green markers and the difference plot are shown below. The black and red represent the observed and calculated traces respectively while the dotted yellow line represent the background plot.

Table 3. Crystallographic data for the PXRD Rietveld refinement.

Identification code	**Zr-BCP**
Empirical formula	C3.5H3.333O2.667Zr0.5
Formula weight	133.67
Temperature/K	N/A

Crystal system	cubic
Space group	*F*23
a=b=c/Å	19.4611
Volume/$Å^3$	7370.59
Z	48
ρ_{calc} g/cm^3	1.4456
Rp	7.5 %
Rwp	10.54 %

4.1.4. References

[1] Li, H., Eddaoudi, M., O'Keeffe, M. and Yaghi, O. M.; Nature, **1999**, *402*, 276 – 279.

[2] Cavka, J. H., Jakobsen, S., Olsbye, U., Guillou, N., Lamberti, C., Bordiga, S. and Lillerud, K. P.; J. Am. Chem. Soc., **2008**, *130*, 13850 – 13851.

[3] Tranchemontagne, D. J., Hunt, J. R. and Yaghi, O. M.; Tetrahedron, **2008**, *64*, 8553 – 8557.

[4] Walton, K. S., Millward, A. R., Dubbeldam, D., Frost, H., Low, J. J., Yaghi, O. M. and Snurr, R. Q.; J. Am. Chem. Soc., **2008**, *130*, 406 – 407.

[5] Liu, X., Wang, Y., Laurini, E., Posocco, P., Chen, H., Ziarelli, F., Janicki, A., Qu, F., Fermeglia, M., Pricl, S., Zhang, C.-C. and Peng, L.; Org. Lett., **2013**, *15*, 4662 – 4665.

[6] Srinivasan, R.; J. Am. Chem. Soc., **1968**, *90*, 2752 – 2754.

[7] Valenzano, L., Civalleri, B., Chavan, S., Bordiga, S., Nilsen, M. H., Jakobsen, S., Lillerud, K. P. and Lamberti, C.; Chem. Mater., **2011**, *23*, 1700 – 1718.

[8] Ming, Y., Kumar, N. and Siegel, D. J.; ACS Omega **2017**, *2*, 4921 – 4928.

5. Flexibility and dynamics in MOFs

5.1. Nitrile-decorated soft metal-organic frameworks

5.1.1. Summary

Metal organic frameworks can display structural flexibility that arises from a variety of mechanisms such as deformation of metal nodes or clusters, ligand tilting and rotation or dynamic response under gas stimuli due to secondary interactions between rigid planes or rod secondary building units. [1,2]

Flexibility has been increasingly investigated for gas storage applications (e.g. adsorbed natural gas storage (ANG) and hydrogen storage) since it often generates S-shaped adsorption isotherms that maximise the working capacity between the storage pressure and the minimum working pressure [3,4].

Moreover, the intrinsic dynamics and flexibility of the framework can generate responsive materials that can be driven by external stimuli such as gas adsorption, light-matter interaction, application of external electrical and magnetic fields, changes in temperature or mechanical actions. This flexible behaviour can be exploited to obtain smart systems operating at molecular level for gas storage, gas and vapour sensing and controlled drug release. On a macroscopic scale these materials can generate complex systems that can change their shape and size under controlled conditions [5,6].

I developed novel flexible MOF during a research period (6 months) spent at the Bernal Institute (University of Limerick) under the supervision of Prof. M. Zaworotko

In the next chapter flexible MOFs based on 1,2-*bis*-(4-pyridil) acrylonitrile (bpAN) will be described ($Zn_2(TPA)_2$(bpAN). The solvothermal reaction of zinc nitrate, terephtalic acid and the ligand bpAN in a 2:2:1 ratio generates a three dimensional two-fold interpenetrated MOF with **pcu** topology based on zinc paddlewheel clusters (α phase) that hosts DMF molecules inside interconnected channels. Upon activation process, this MOF undergoes a dramatic structural rearrangement due to the change in coordination sphere of zinc ions from square pyramidal to tetrahedral geometry. The transition generates tightly packed close phase with extended and multiple π···π

interactions. Surprisingly, this phase can rearrange itself into porous structures under external gas stimuli giving rise to switching adsorption isotherms characterized by a sudden gas uptake at specific temperature and pressure conditions. Moreover, a family of isostructural mixed-linker MOFs with different molar ratio of terephtalic acid and 2-amino terephtalic acid display tunable switching threshold pressure and show completely different behaviour in presence of various gaseous species (nitrogen and carbon dioxide at 77 K and 195 K, respectively).

Future work will be focused on the measurements of high temperatures and pressures adsorption isotherms, adsorption kinetics of several gases (CO_2, CH_4 and N_2), direct measurement of isosteric heat of adsorption with a microcalorimetric method coupled to adsorption processes and detailed investigation of the structural rearrangement that takes place during gas adsorption through multiple *in situ* spectroscopic techniques.

5.1.2. Flexible metal-organic frameworks (FMOFs)

5.1.2.1. Structures of FMOFs

Metal-organic frameworks usually display rigid three-dimensional microporous structures. However, flexible or third generation metal organic frameworks (FMOFs) display intrinsic dynamics of their framework. Prototypal systems were MIL-53(Cr), Co(bdp) or pillared structures based on Zn or Cu paddlewheel clusters as MOF-508 [$Zn_2(bdc)_2(bpy)$]. [7,8,9] Dynamical properties in MOFs can be related to different microscopic mechanisms and can be influenced in many ways.

- **Two dimensional or layered MOFs**. Layered 2D metal organic materials can display switching and stepped adsorption isotherms due to formation of host-guest chlatrates with gaseous molecules and subsequent expansion of the interlayer distance to accommodate even higher amount of guests. Square lattice coordination polymers as [$Cu(BF_4)_2(bipy)_2$] (ELM-11, where bipy = 4,4'-bipyridine) reported by Kondo et *al.* and [$Co(bipy)_2(NCS)_2$] described by Wang et *al*. show switching CO_2 adsorption isotherms. Interestingly, the

absence of structural strain associated with the phase change provides high recyclability of these materials [10,11].

- **Flexibility of the organic linkers or at the metal nodes**. Coordination bonds between the metal node or cluster and the functional group of the linker can distort in both distance and angles. For example, Co(bdp) displays a severe distortion of the coordination sphere of cobalt atoms after desolvation that generates a close-packed structure: during adsorption processes with various gases the structure adapts to accommodate different guest loadings at different pressure and temperatures and gives rise to multi-stepped isotherms. [12,13]
- **Interpenetrated MOFs**. Interpenetrated frameworks can glide one against the other to switch between different phases. Usually, during the synthetic process solvent molecules can be trapped inside the growing material avoiding further interpenetration and promoting the formation of low density structures. Solvent removal during the activation process generates capillary forces that can induce structural changes towards more compact structures stabilized through multiple intermolecular interactions. The mechanism responsible for the phase transition can be either related to bending and tilting of organic ligands, distorsion of the coordination sphere around metal centers or coordination isomerism. [14,15].

Some examples of flexible metal organic frameworks are reported below.

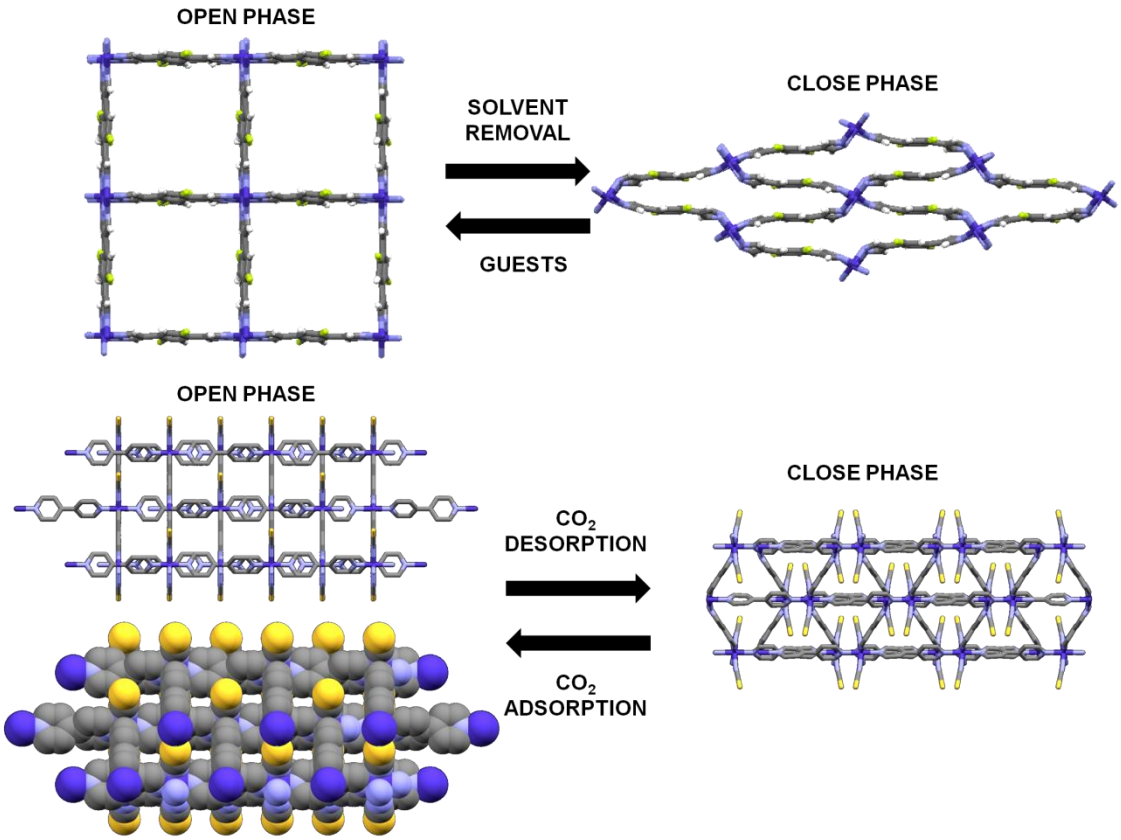

Figure 1. Top: flexible MOF based on bi-pyrazolate ligands and cobalt cations (**Co(*p*-F_2-bdp)**). The solvent molecules have been removed from the open phase for clarity.[16] Bottom: 2D square grid framework of $Co(bipy)_2(NCS)_2$ (**sql-1-Co-NCS**). This layered MOF display switching adsorption isotherms for carbon dioxide adsorption. CO_2 molecules have been removed from the open phase for clarity [11].

5.1.2.2. Applications of FMOFs

Flexible metal organic materials can display peculiar structure-property relationships that can provide superior performances in various applications.

- **Gas storage**. Microporous materials have long been studied for their application in gas storage due to the possible increase in the amount of stored gas or vapours related to the excess uptake determined by the confinement of molecules inside a porous host that determines a local increase in density of the fluid compared to simple compression processes under the same conditions.

Thus, porous materials can potentially reduce the pressure needed for gas and vapour storage with beneficial decrease of costs and ease management of these chemical species [13]. Among other gases methane and hydrogen have been particularly investigated as cleaner and useful gases that can be stored with adsorbed technology. Flexible materials displaying switching adsorption isotherms can provide improvement in gas storage applications due to the increase in working capacity, i.e. the amount of gas stored between the storage pressure and the discharge pressure (figure 2).

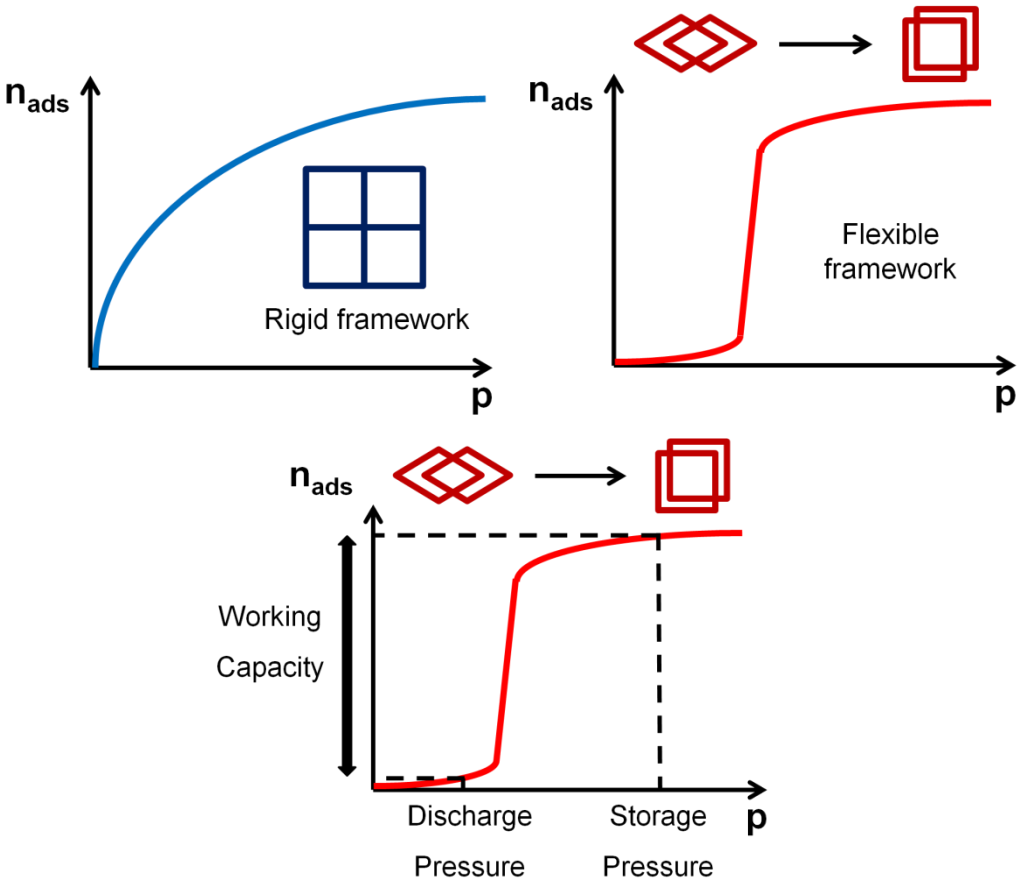

Figure 2. Top: scheme of different shapes of adsorption isotherms in microporous materials. Left: type I adsorption isotherm. Right: switching adsorption isotherm (type F-IV). Bottom: scheme of working capacity for a switching materials.

- **Sensing**. Flexibility can provide highly selective uptake of molecules either in gas or vapour phase or in the liquid state: changes of the physicochemical properties upon the adsorption processes can be exploited as signals for detection. Changes in optical properties have often been employed to monitor

the adsorption process; e.g. changes in photoluminescence or optical absorption. For example, Takashima et *al.* developed a flexible MOF containing electron-poor naphtalenediimide moieties as pillared struts: different volatile organic compounds accommodate in different ways inside the flexible framework drastically changing the fluorescence properties. [17].

- **Capture and controlled release of guests**. Flexible MOFs that can respond to external stimuli can be engineered for applications in drug delivery and removal of hazardous substances. For example Chandler and co-workers reported a MOF capable of entrapping different gases (CO_2, O_2, N_2, CH_4, He, Ar, Xe and NH_3) upon dehydration process and releasing them after hydration in a reversible manner [18]. Moreover, flexible MOFs can be designed for controlled drug release: an in-depth understanding of the kinetic of structural transformation and releasing process is a key point for development of novel systems. [19]
- **Switching electronic, optical and magnetic properties**. Electronic properties of MOFs are currently under investigation by different research groups since they can be effectively exploited in catalytic and photocatalytic applications and in hybrid electronic and optoelectronic devices [20]. Since these properties as well as optical and magnetic properties strongly depend on the structure of the material, flexibility plays a key role.
- **Flexibility induced guests uptake and reactivity.** Uemura et *al.* demonstrated how flexibility impacts the occurrence of *p*-divinylbenzene uptake and polymerization reaction in two isostructural MOFs displaying two fold interpenetration and different metals, zinc and copper, respectively [21]. Flexible zinc-based MOFs display higher adsorption values of the liquid monomer and, in presence of a radical initiator, promote the topotactic polymerization of *p*-divinylbenzene generating linear polymers with pendant vinyl groups, instead of the cross-linked resin generated in the bulk state under the same experimental conditions.

5.1.3. Nitrile-decorated FMOFs

5.1.3.1. General overview

In order to generate a flexible and potentially switching material different MOFs displaying twofold interpenetrated structures and **pcu** topology have been designed and synthetized due to the well-known flexibility of these structures. [8,22].

A pillaring strut (bpAN) has been synthesized through Knoevenagel condensation reaction of 4-pyridineacetonitrile with 4-pyridinecarboxyaldehyde catalyzed with sodium hydroxide in ethanol. Under optimised conditions the reaction yield is about 55 % and the product is obtained in high purity as a polycrystalline powder that has been characterized with multiple techniques. (see Experimental Details for further information).

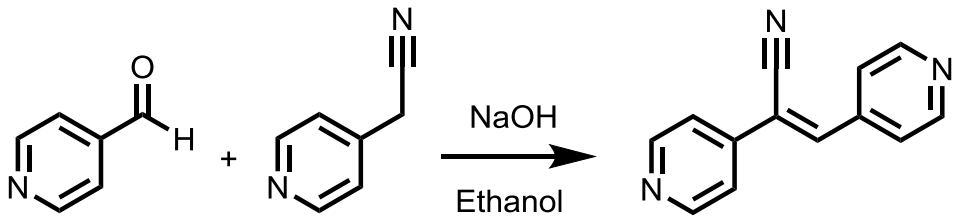

Scheme 1. Synthetic scheme for the preparation of nitrogen-based linker 1,2-*bis*-(4-pyridil) acrylonitrile (bpAN).

A novel metal organic framework has been grown under solvothermal conditions employing a 2:2:1 ratio of zinc nitrate hexahydrate: terephtalic acid and bpCNe linker. Moreover, this strategy can be easily adapted to grow isoreticular MOFs based on functionalized terephtalic acid: below I will focus on materials mainly obtained with terephtalic acid (TPA), 2-aminoterephtalic acid (2A-TPA) or a mixture of these reagents. A series of 5 MOFs have been obtained by using either the pure monomers or mixture of the different building blocks at specified ratios: the feed ratios are reported in the table below.

Table 1. Feed ratio composition of MOFs (equivalent).

Sample	$Zn(NO_3)_2 \cdot 6H_2O$	TPA	2A-TPA	bpCNe
$Zn_2(TPA)_2(bpAN)$	2	2	-	1
$Zn_2(TPA)_{1.5}(2A\text{-}TPA)_{0.5}(bpAN)$	2	1.5	0.5	1
$Zn_2(TPA)_1(2A\text{-}TPA)_1(bpAN)$	2	1	1	1
$Zn_2(TPA)_{0.5}(2A\text{-}TPA)_{1.5}(bpAN)$	2	0.5	1.5	1
$Zn_2(2A\text{-}TPA)_2(bpAN)$	2	-	2	1

5.1.3.2. $Zn_2(TPA)_2(bpAN)$

The structure of $Zn_2(TPA)_2(bpAN)$ has been solved by single crystal analysis. This MOF crystallizes in triclinic space group *P*-1 and displays **pcu** topology and two-fold off-set interpenetrated nets (α phase). Each net is constitute by square grid planes of dicarboxylic acid connected through zinc paddlewheel clusters that are pillared by the bpAN molecules along c axis. The paddlewheel unit displays a Zn···Zn distance of 2.98 Å, similar to literature values, but it shows a distorted geometry. DMF molecules are disordered inside MOF channels. PXRD on powdered samples confirms the phase purity and high crystallinity of the bulk material.

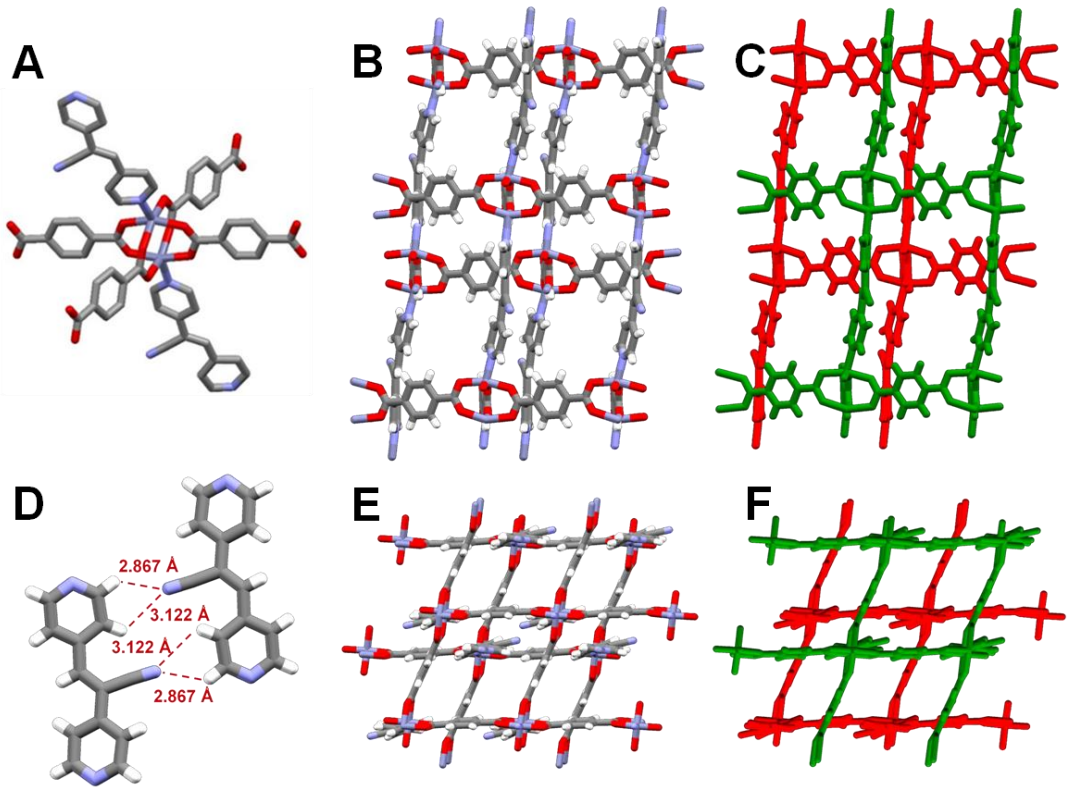

Figure 3. A) Zinc paddlewheel cluster. B) and C) Crystal structure of $Zn_2(TPA)_2(bpAN)$ viewed along a axis. In C) the two subnets are highlighted in different colours D) Intermolecular interactions between bpAN units of different subnets. E) and F) Crystal structure of $Zn_2(TPA)_2(bpAN)$ view along c axis. In F) the two subnets are highlighted in different colours.

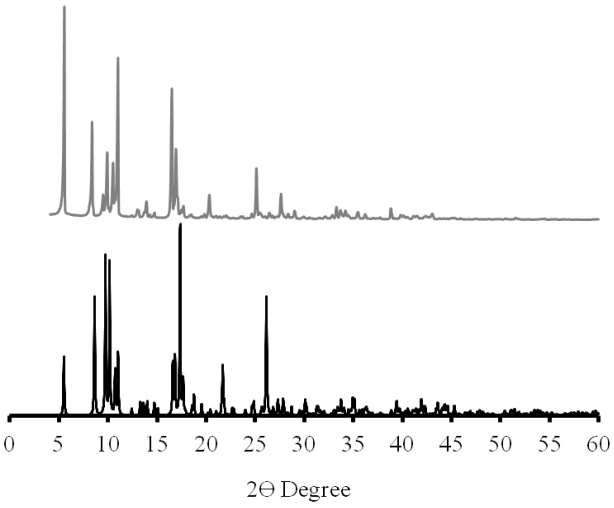

Figure 4. Experimental powder x-ray diffraction of $Zn_2(TPA)_2(bpAN)$ collected between 3 and 60 2Θ degree (grey line). Simulated powder x-ray diffraction pattern from single crystal data (black line).

After the activation process at 130°C under high vacuum many crystals of $Zn_2(TPA)_2(bpAN)$ are still translucent and are suitable for SC-XRD analysis. The structure displays a dramatic change in the unit cell as well as connectivity of the metal cluster. In the close phase (β phase) terephtalic acid moieties along one direction break one Zn···O bond becoming mono-dentate ligands. Thus, the coordination number of the Zn atoms changes from 5 to 4 and the paddlewheel cluster alters its structure. The mono-dentate ligand fits inside the channels that are present in the open phase and arrange itself almost parallel to bp(AN) units. The unit cell reduces about 28 % its volume during the de-solvation process. Collectively, the structure undergoes an open to close phase transition due to coordination isomerism at the metal cluster.

PXRD performed on the powdered activated sample confirms the phase purity and high crystallinity of the activated MOF, even after the structural rearrangement due to solvent removal.

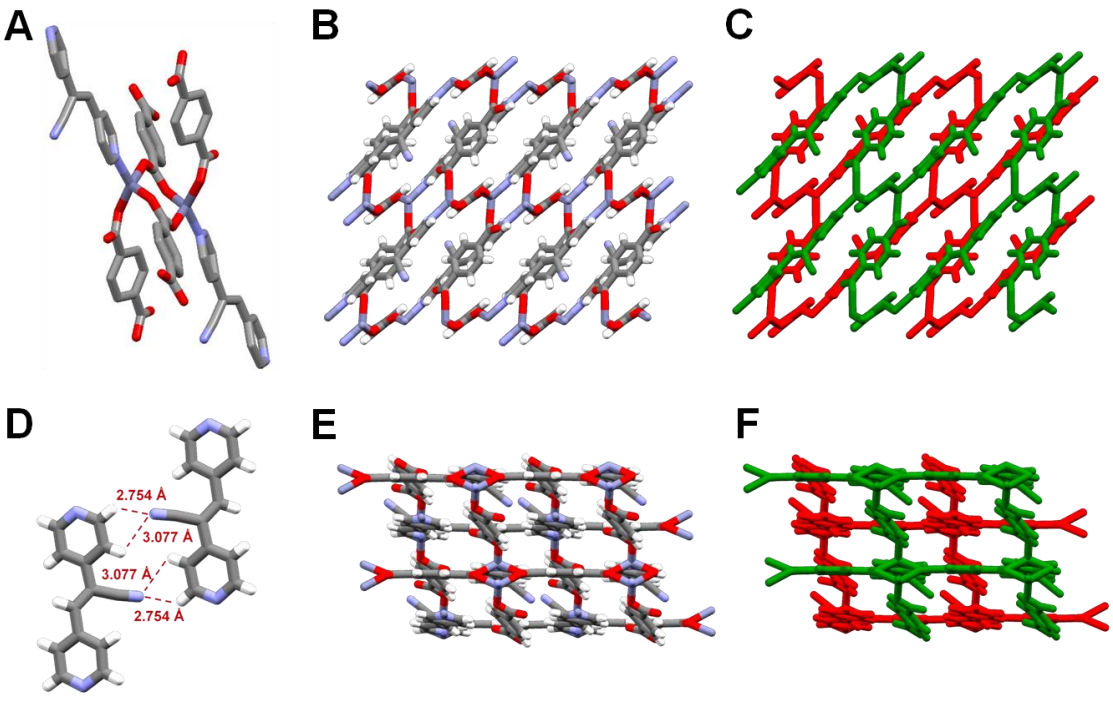

Figure 5. A) Zinc tetrahedral cluster. B) and C) Crystal structure of de-solvated $Zn_2(TPA)_2(bpAN)$ viewed along b axis. In C) the two subnets are highlighted in different colours D) Intermolecular interactions between bpAN units of different subnets. E) and F) Crystal structure of de-solvated $Zn_2(TPA)_2(bpAN)$ (top view). In F) the two subnets are highlighted in different colours.

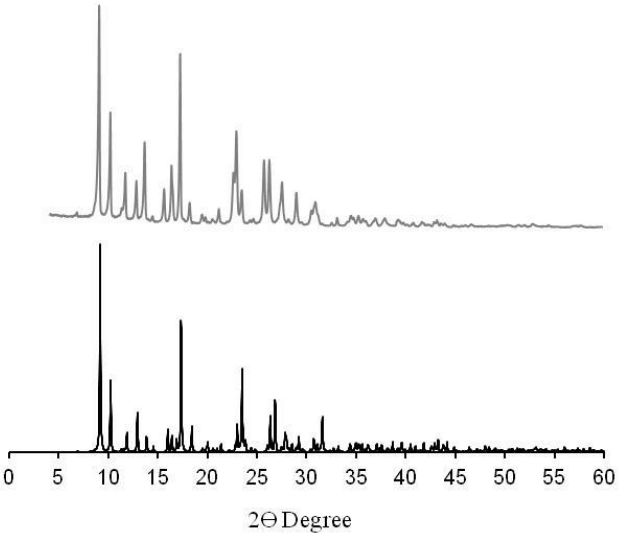

Figure 6. Experimental powder x-ray diffraction of dried sample $Zn_2(TPA)_2(bpAN)$ collected between 3 and 60 2Θ degree (grey line). Simulated powder x-ray diffraction pattern from single crystal data (black line).

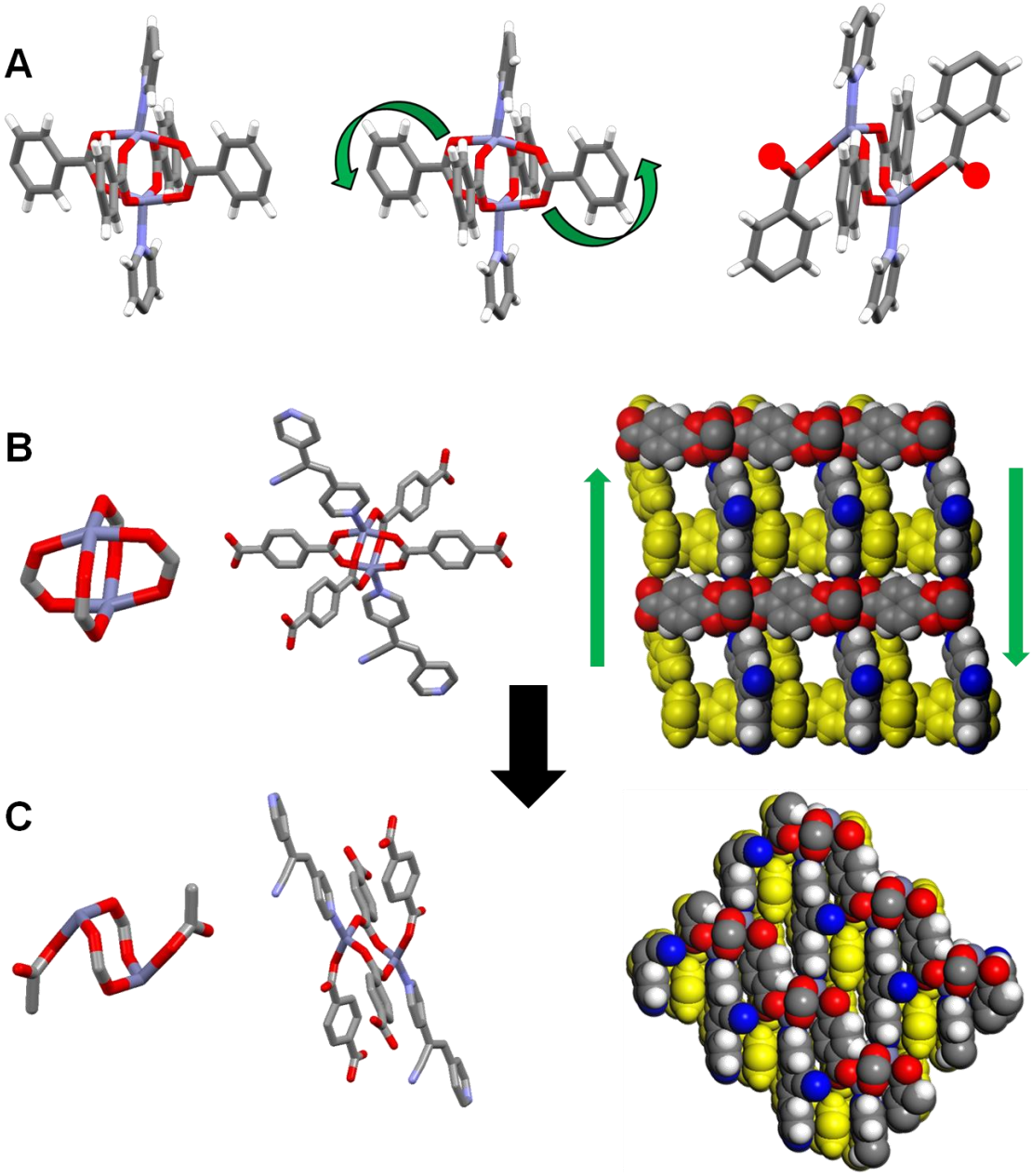

Figure 7. A) Possible rearrangement mechanism of Zn coordination sphere. From left to right: Zn paddlewheel cluster in the open phase; Zn···O bond breakage and ligand rotation; distorted tetrahedral coordination of zinc cations in the de-solvated phase (red dots identify the dangling carbonyl functional group). B) Open phase structure. From left to right: Zn paddlewheel cluster and crystal structure view along channels. C) Close phase structure. From left to right: distorted tetrahedrally coordinated Zn cations and close packed structure.

Infrared spectroscopy is a valuable tool to confirm qualitatively the formation of the network and to follow the structural rearrangement following activation process. The

as-synthetized MOF displays vibrational bands related to the entrapped solvent molecules inside the channels: figure 8 shows the comparison between the I.R. spectra of the solvated and activated phase of sample $Zn_2(TPA)_2(bpAN)$. In the open phase DMF vibrational bands are clearly visible at 1670 cm^{-1} (C=O stretching), 1094 cm^{-1} and 658 cm^{-1} and vibrational bands at 2860 and 2925 cm^{-1} (see figure X.) confirm the analysis above. In the region between 1300 cm^{-1} and 1600 cm^{-1} vibrational bands related to carbonyl stretching modes are strongly affected by the structural changes and the variation of coordination to the zinc atom.

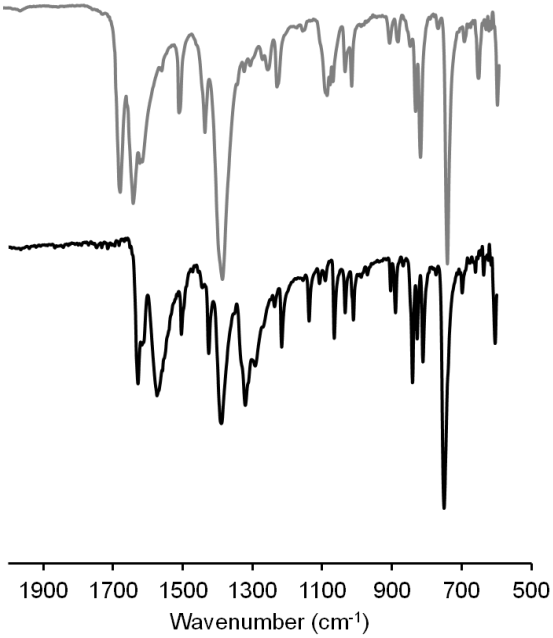

Figure 8. Infrared spectra of as-synthetized $Zn_2(TPA)_2(bpAN)$ (top, grey) and dried $Zn_2(TPA)_2(bpAN)$ (bottom, black) between 500 and 2000 cm^{-1}.

Gas adsorption properties have been tested at low temperature. The close phase has been exposed to nitrogen at 77 K and CO_2 at 195 K up to 1 bar of pressure. While the material does not show any uptake of nitrogen at low temperature, CO_2 adsorption is triggered at pressure of 70 mbar ($p/p° = 0.09$). The adsorption features a step isotherm up to an uptake as high as 130 cm^3/g that is possibly related to the formation of an open phase due to the re-generation of the zinc paddlewheel cluster inside the structure (a detailed analysis of the structural transformation is currently under

investigation). After reaching a plateaux, the material can accommodate higher quantity of CO_2 above 150 mbar up to 215 cm^3/g.

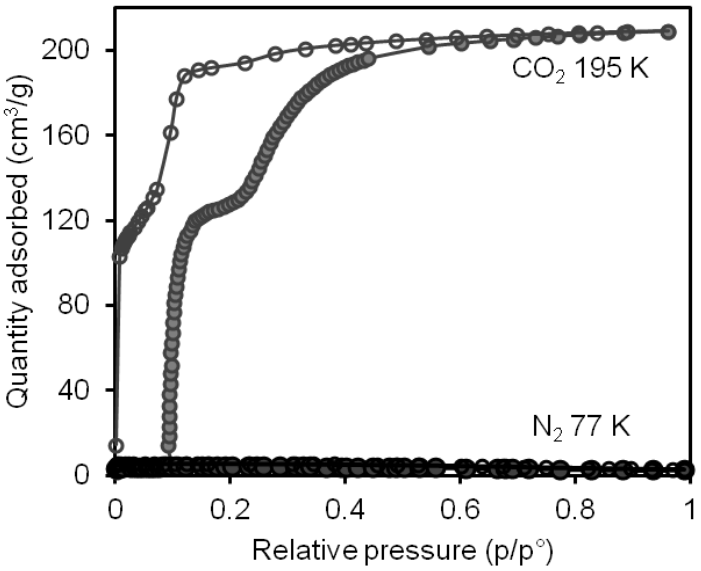

Figure 9. N_2 adsorption isotherm collected at 77K (black line) and CO_2 adsorption isotherms measured at 195 K of $Zn_2(TPA)_2(bpAN)$ (grey line).

5.1.3.3. $Zn_2(TPA)_X(2A\text{-}TPA)_{(2-X)}(bpAN)$

An isostructural serie of MOFs can be easily grown under the same experimental conditions: different functional groups in the terephtalic acid unit do not affect the connectivity and topology of the frameworks. Interestingly, a series of mixed linkers MOFs can be obtained starting from bare terephtalic acid and 2-amino terephtalic acid: changing the linker ratio inside MOFs can be exploited to explore the effects on host-host and host-guest interactions.

All MOFs generated with different molar ratios of TPA and 2A-TPA display similar crystalline structures as observed from powder x-ray diffraction data.

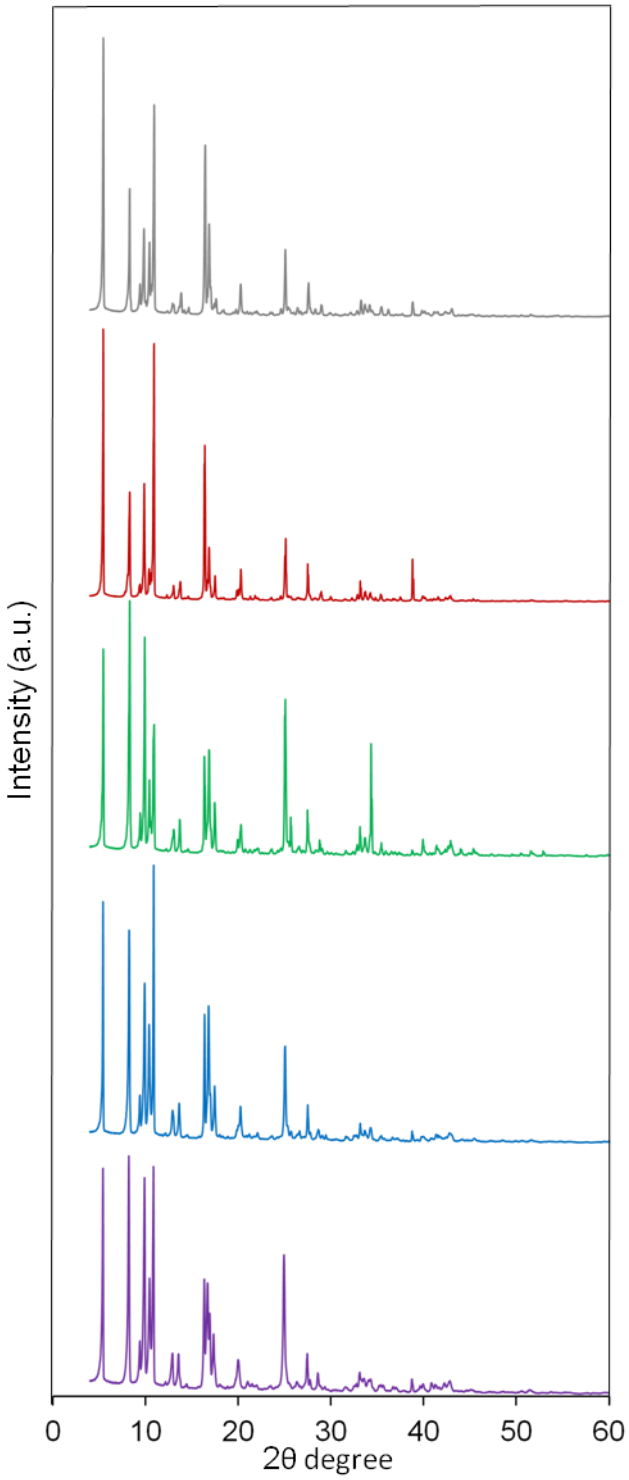

Figure 10. Powder X-ray diffraction patterns of $Zn_2(TPA)_2(bpAN)$ (top, grey line), $Zn_2(TPA)_{1.5}(2A\text{-}TPA)_{0.5}(bpAN)$ (red line), $Zn_2(TPA)_1(2A\text{-}TPA)_1(bpAN)$ (green line), $Zn_2(TPA)_{0.5}(2A\text{-}TPA)_{1.5}(bpAN)$ (blue line) and $Zn_2(2A\text{-}TPA)_2(bpAN)$ (bottom, purple line).

Thermogravimetric analyses under inert atmosphere of the as-synthetized samples show weight loss at temperatures below 150°C due to pore evacuation of solvent molecules entrapped inside pores. The first weight loss below 80°C is due to methanol guest molecules and its contribution increases as the number of inserted nitrogen atoms inside the frameworks increase, probably due to hydrogen bonding of the methanol molecules with the amine units of 2A-TPA. A second mass decrease below 150°C is related to DMF molecule loss and the total weight loss range from 16.2 to 18.7 %. The desolvated crystals display thermal stability up to 330°C before the degradation of organic phase.

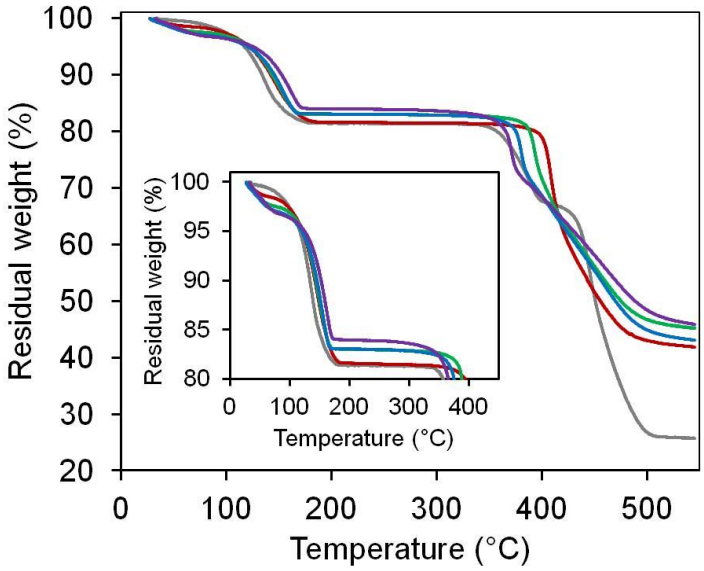

Figure 11. TGA analysis of as-synthetized MOFs performed under inert atmosphere (nitrogen flow) performed at 10°C/min [$Zn_2(TPA)_2(bpAN)$ (grey line), $Zn_2(TPA)_{1.5}(2A\text{-}TPA)_{0.5}(bpAN)$ (red line), $Zn_2(TPA)_1(2A\text{-}TPA)_1(bpAN)$ (green line), $Zn_2(TPA)_{0.5}(2A\text{-}TPA)_{1.5}(bpAN)$ (blue line) and $Zn_2(2A\text{-}TPA)_2(bpAN)$ (purple line)].

Moreover, all MOFs display similar PXRD after solvent removal suggesting the formation of similar structures even in the close phase.

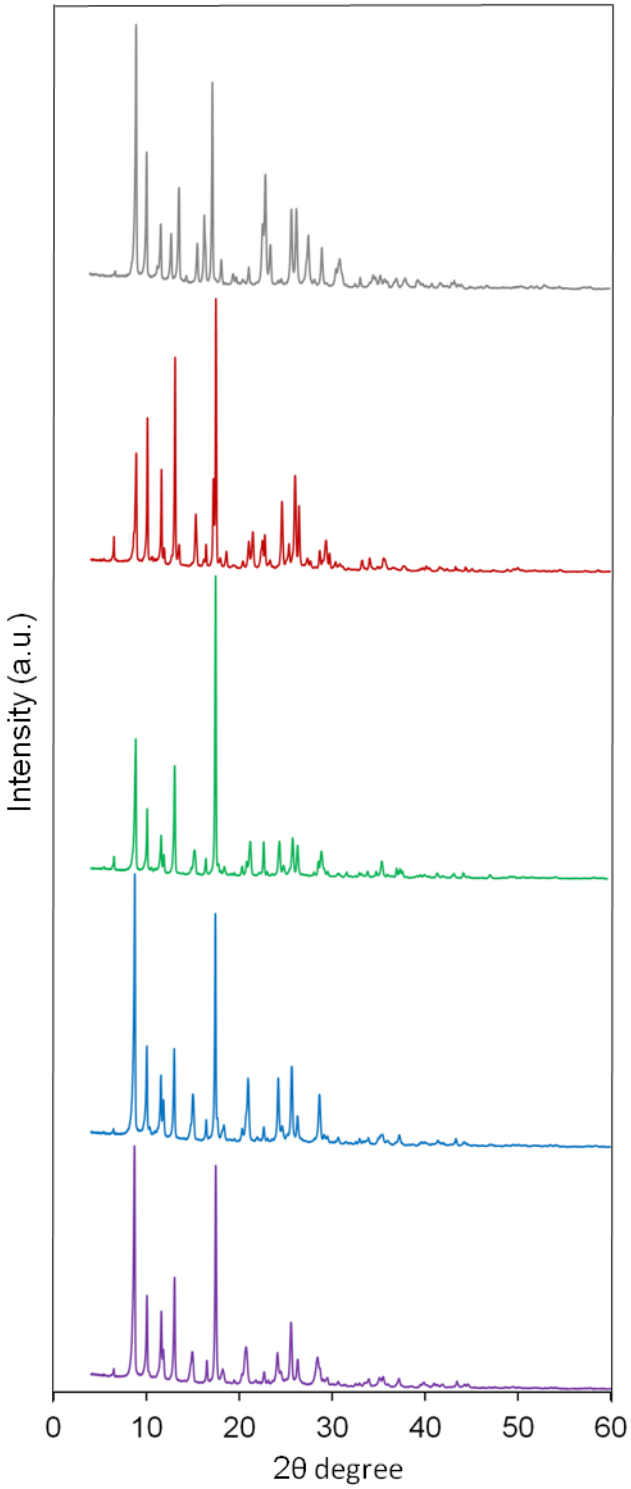

Figure 12. Powder X-ray diffraction patterns of activated samples: $Zn_2(TPA)_2(bpAN)$ (top, grey line), $Zn_2(TPA)_{1.5}(2A\text{-}TPA)_{0.5}(bpAN)$ (red line), $Zn_2(TPA)_1(2A\text{-}TPA)_1(bpAN)$ (green line), $Zn_2(TPA)_{0.5}(2A\text{-}TPA)_{1.5}(bpAN)$ (blue line) and $Zn_2(2A\text{-}TPA)_2(bpAN)$ (bottom, purple line).

TGA analysis of activated samples performed under inert atmosphere (nitrogen flux) display no weight loss up to the thermal degradation temperature (330°C).

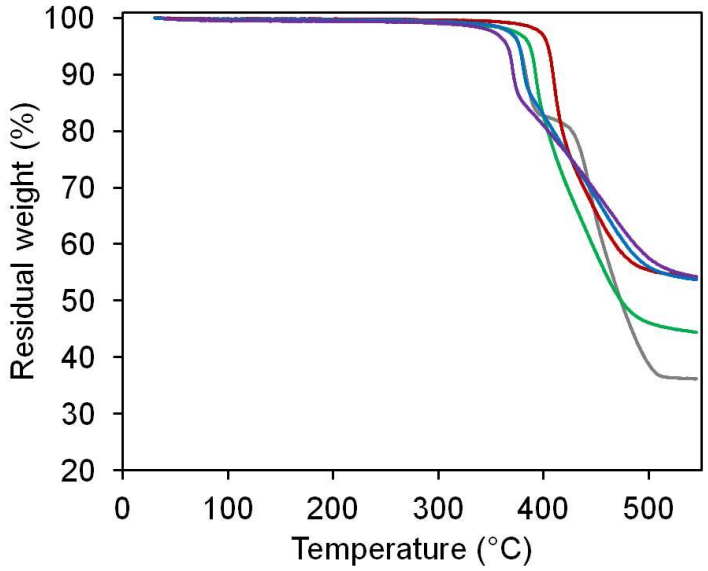

Figure 13. TGA analysis of activated MOFs performed under inert atmosphere (nitrogen flow) performed at 10°C/min. $Zn_2(TPA)_2(bpAN)$ (top, grey line), $Zn_2(TPA)_{1.5}(2A\text{-}TPA)_{0.5}(bpAN)$ (red line), $Zn_2(TPA)_1(2A\text{-}TPA)_1(bpAN)$ (green line), $Zn_2(TPA)_{0.5}(2A\text{-}TPA)_{1.5}(bpAN)$ (blue line) and $Zn_2(2A\text{-}TPA)_2(bpAN)$ (bottom, purple line).

Figures 14 and 15 display the IR spectra of samples with increasing amino groups content. The N-H symmetric and asymmetric stretching modes at 3344 cm^{-1} and 3463 cm^{-1}, respectively, display higher intensities on increasing amine loading inside MOFs and a sharp peak appears at 1256 cm^{-1} (1248 cm^{-1} in activated compounds) due to the phenyl carbon-nitrogen bond (C-N) of amino groups.

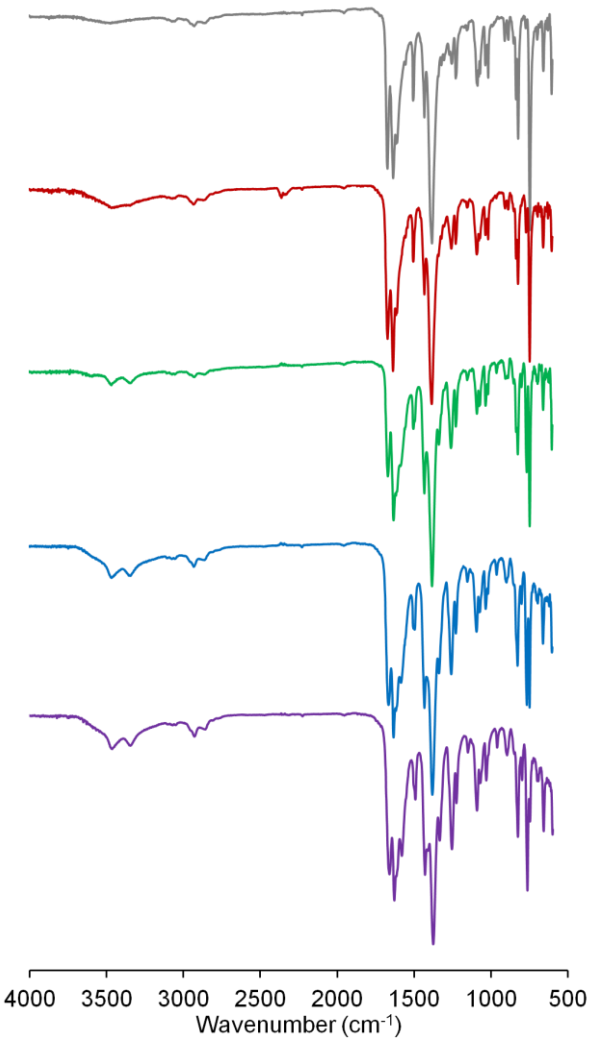

Figure 14. From top to bottom: infrared spectra of as-synthetized samples. $Zn_2(TPA)_2(bpAN)$ (top, grey line), $Zn_2(TPA)_{1.5}(2A\text{-}TPA)_{0.5}(bpAN)$ (red line), $Zn_2(TPA)_1(2A\text{-}TPA)_1(bpAN)$ (green line), $Zn_2(TPA)_{0.5}(2A\text{-}TPA)_{1.5}(bpAN)$ (blue line) and $Zn_2(2A\text{-}TPA)_2(bpAN)$ (bottom, purple line).

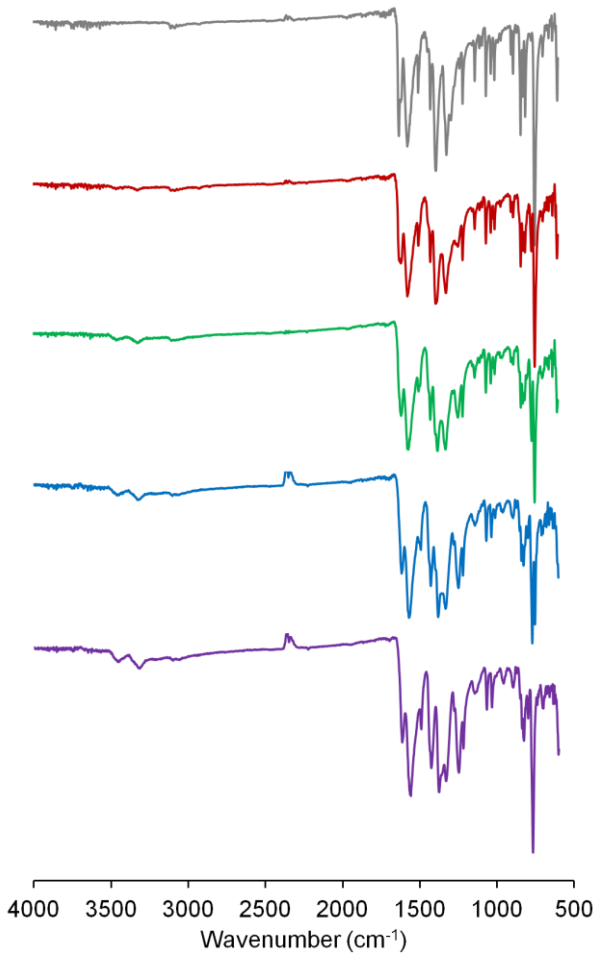

Figure 15. From top to bottom: infrared spectra of activated samples. $Zn_2(TPA)_2(bpAN)$ (top, grey line), $Zn_2(TPA)_{1.5}(2A\text{-}TPA)_{0.5}(bpAN)$ (red line), $Zn_2(TPA)_1(2A\text{-}TPA)_1(bpAN)$ (green line), $Zn_2(TPA)_{0.5}(2A\text{-}TPA)_{1.5}(bpAN)$ (blue line) and $Zn_2(2A\text{-}TPA)_2(bpAN)$ (bottom, purple line).

Low temperature adsorption isotherms have been measured for all samples. Nitrogen adsorption isotherms at 77 K display no uptake (less than 5 cm^3/g). Surprisingly, $Zn_2(TPA)_{1.5}(2A\text{-}TPA)_{0.5}(bpAN)$ shows a sudden uptake of nitrogen at 0.33 p/p° (250 mbar): at this pressure the sample undergoes a phase change and adsorbs 140 cm^3/g in a single step process. Carbon dioxide adsorption isotherms display stepped behavior with a sudden uptake at pressures modulated by the amount of amino groups decorating the frameworks. Moreover, the amine functionalization modulates also the gate opening behavior at higher partial pressure. The selective introduction of functionalized organic linker can thus control the switching behavior and the gate-opening effect that govern the adsorptive properties of these materials.

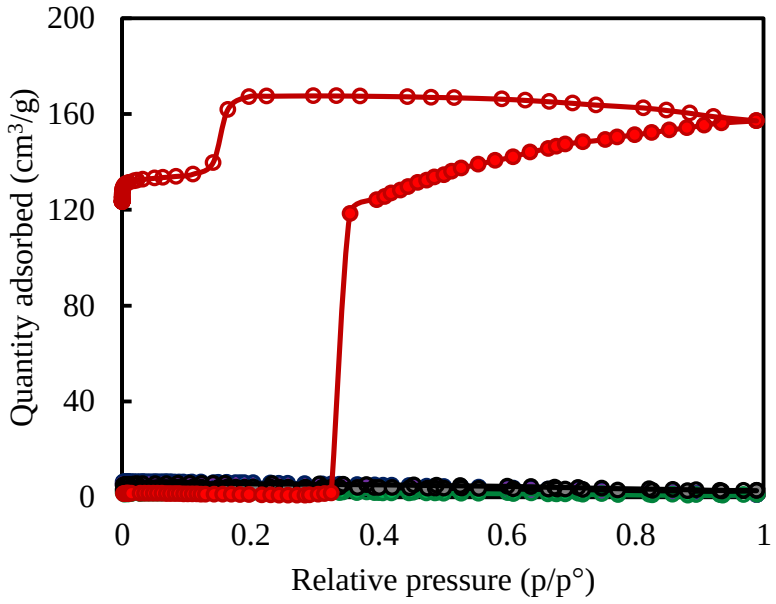

Figure 16. N_2 adsorption isotherms measured at 77 K of $Zn_2(TPA)_2(bpAN)$ (grey line), $Zn_2(TPA)_{1.5}(2A\text{-}TPA)_{0.5}(bpAN)$ (red line), $Zn_2(TPA)_1(2A\text{-}TPA)_1(bpAN)$ (green line), $Zn_2(TPA)_{0.5}(2A\text{-}TPA)_{1.5}(bpAN)$ (blue line) and $Zn_2(2A\text{-}TPA)_2(bpAN)$ (purple line).

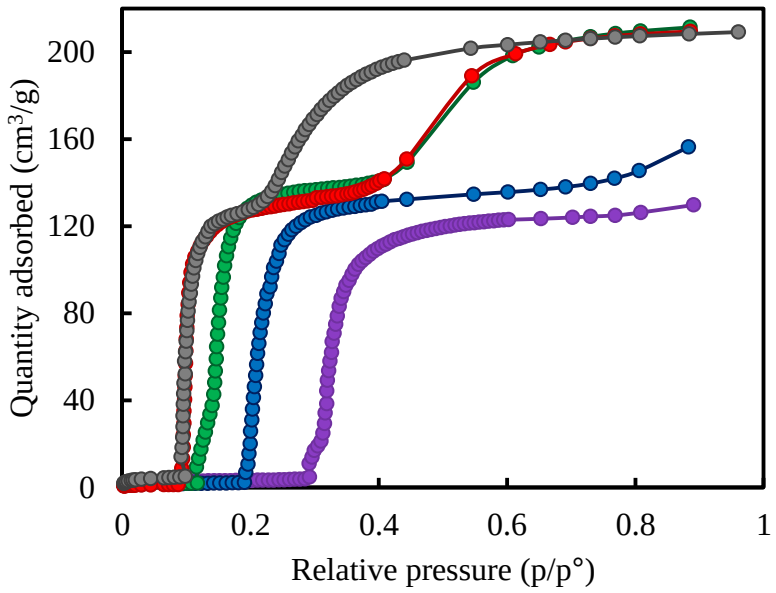

Figure 17. Adsorption branches of CO_2 adsorption isotherms measured at 195 K for $Zn_2(TPA)_2(bpAN)$ (grey line), $Zn_2(TPA)_{1.5}(2A\text{-}TPA)_{0.5}(bpAN)$ (red line), $Zn_2(TPA)_1(2A\text{-}TPA)_1(bpAN)$ (green line), $Zn_2(TPA)_{0.5}(2A\text{-}TPA)_{1.5}(bpAN)$ (blue line) and $Zn_2(2A\text{-}TPA)_2(bpAN)$ (purple line).

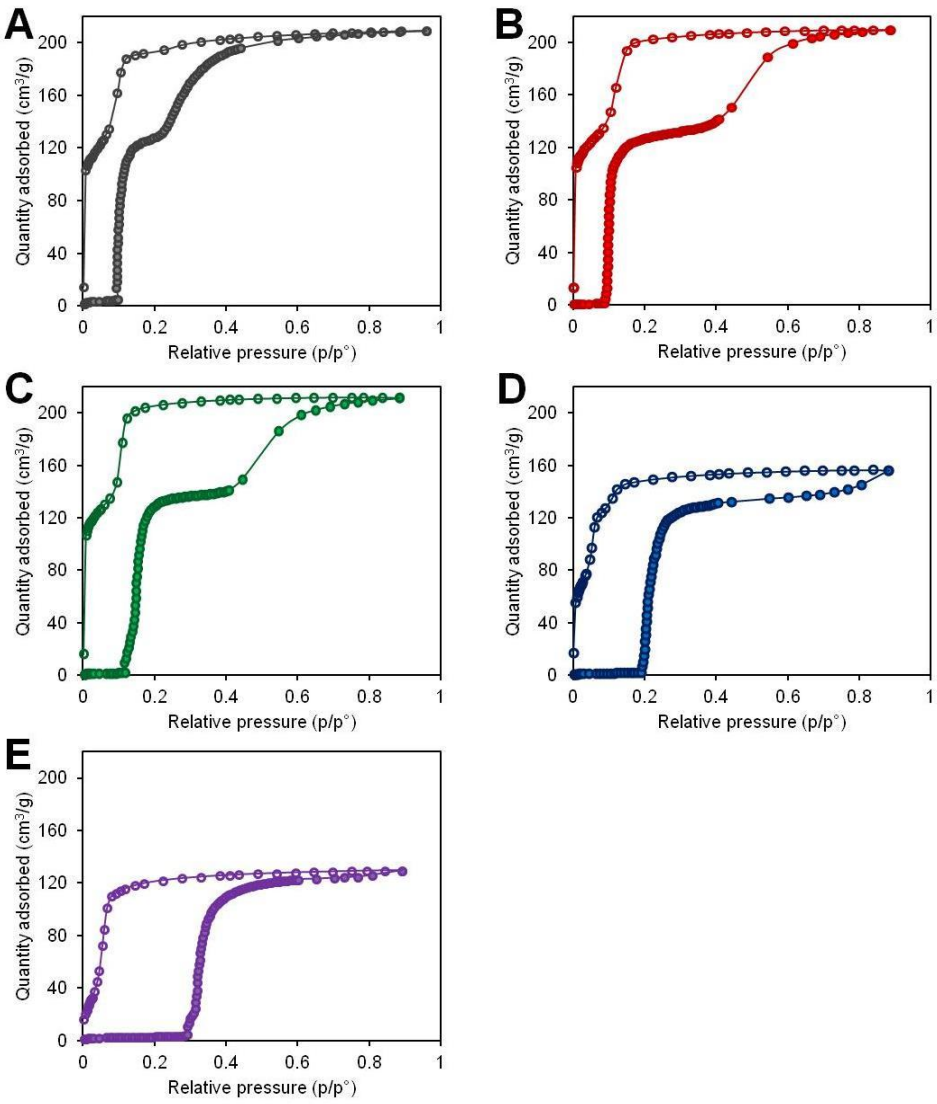

Figure 18. CO_2 adsorption isotherms measured at 195 K. A) $Zn_2(TPA)_2(bpAN)$ (grey line). B) $Zn_2(TPA)_{1.5}(2A\text{-}TPA)_{0.5}(bpAN)$ (red line). C) $Zn_2(TPA)_1(2A\text{-}TPA)_1(bpAN)$ (green line). D) $Zn_2(TPA)_{0.5}(2A\text{-}TPA)_{1.5}(bpAN)$ (blue line). E) $Zn_2(2A\text{-}TPA)_2(bpAN)$ (purple line).

Table 2. Switching threshold pressures and gate-opening pressures for MOFs with CO_2 at 195 K.

Sample	**Switching threshold pressure (mbar)**	**Gate-opening pressure (mbar)**
$Zn_2(TPA)_2(bpAN)$	70	170
$Zn_2(TPA)_{1.5}(2A\text{-}TPA)_{0.5}(bpAN)$	70	300

$Zn_2(TPA)_1(2A\text{-}TPA)_1(bpAN)$	90	300
$Zn_2(TPA)_{0.5}(2A\text{-}TPA)_{1.5}(bpAN)$	145	600
$Zn_2(2A\text{-}TPA)_2(bpAN)$	220	Not observed

5.1.4. Conclusion

Novel Flexible Metal Organic Frameworks (FMOFs) that exhibit a phase transition between a close and an open phase under gas adsorption stimuli have been developed during my research period abroad (6 months) at Bernal Institute in Limerick, Ireland, under the supervision of Prof. M. J. Zaworotko,. Single crystal x-ray technique (SC-XRD) of both the open and close phases highlighted the structural transformation during the phase change at the atomic level: during sample evacuation zinc-based nodes change their coordination environment from square-planar to tetrahedral coordination resulting in tightly packed structures (β phases). In presence of different gases as carbon dioxide (195 K) and nitrogen (77 K) the samples switched back to open phases and accommodate guest molecules inside the empty channels showing type F-IV adsorption isotherms. These samples have been fully characterized with thermal techniques, Infrared spectroscopy and powder x-ray diffraction. Upcoming adsorption measurement of methane at low temperature (195 K, 1 bar) and high pressures (35, 65 and 100 bar at or near room temperature) will assess the potential application of these materials for ANG. In situ powder x-ray diffraction, Raman spectroscopy and NMR will be performed to shed light on the kinetics and mechanism of phase change.

5.1.5. Experimental details

Linker synthesis (bpAN)

Briefly, 4-pyridineacetonitrile (118.1 mg; 1 mmol) is dissolved in EtOH (7 ml) and stirred. 4-pyridinecarboxyaldehyde (95 μL; 1 mmol) has been added. Then, 500 μL of a sodium hydroxide solution in ethanol prepared by dissolving 100 mg of NaOH in 10 mL of ethanol has been added dropwise over 10 minutes period. A white precipitate forms during the addition process. Agitation is stopped and the slightly pinkish

product has been filtered and washed with a 1 mL of ethanol. The solid has been further purified by crystallization in THF/Hexane to give an off-white microcrystalline solid. Yield: 106 mg; 55%.

MOFs preparation

General procedure.

The dicarboxylic acid linker (0.7 mmol, total) and bpAN (0.35 mmol) are dissolved in a 1:1 mixture of DMF and methanol at room temperature (28 ml, total). Zinc nitrate hexahydrate (0.7 mmol) is dissolved in 7 ml of DMF and the solution is added to the solution of the linkers. The mixture is briefly sonicated (1 minute) and then heated at 120°C for 11 hours. The vial is removed from the oven and cool down to room temperature. The crystals are collected by filtration and washed with a 3:2 mixture of DMF and methanol.

Crystallographic data

Table 3. Crystallographic data of α-$Zn_2(TPA)_2$(bpAN) (open phase)

Identification code	**α-$Zn_2(TPA)_2$(bpAN)**
Empirical formula	0.5(C29 H17 N3 O8 Zn2)(+ solvent)
Formula weight	1332.2
Temperature/K	N/A
Crystal system	triclinic
Space group	*P*-1
a/Å	10.8469
b/Å	10.8596
c/Å	16.2749
α/°	81.489
β/°	81.774
γ/°	71.162
Volume/$Å^3$	1785.08
Z	4
ρ_{calc}g/cm^3	1.239

Table 4. Crystallographic data of β-$Zn_2(TPA)_2$(bpAN) (close phase)

Identification code	**β-$Zn_2(TPA)_2$(bpAN)**
Empirical formula	0.5(C29 H17 N3 O8 Zn2)
Formula weight	1332.2
Temperature/K	N/A
Crystal system	triclinic
Space group	*P*-1
a/Å	9.7438
b/Å	10.4585
c/Å	12.8938
α/°	98.498
β/°	90.380
γ/°	99.233
Volume/$Å^3$	1282.07
Z	4
$\rho_{calc}g/cm^3$	1.725

5.1.6. References

[1] Schneemann, A., Bon, V., Schwedler, I., Senkovska, I., Kaskel, S. and Fischer, R. A.; Chem. Soc. Rev., **2014**, *43*, 6062 – 6096.

[2] Horike, S., Shimomura and S. and Kitagawa, S.; Nature Chem., **2009**, *1*, 695–704.

[3] Chang, Z., Yang, D.-H., Xu, J., Hu, T. L., Bu, X.-H.; Adv. Mater., **2015**, *27*, 5432-5441.

[4] Zhang, J.-P., Zhou, H.-L., Zhou, D.-D., Liao, P.-Q. and Chen, X.-M.; national science review, **2018**, *5*, 907-919.

[5] Coudert, F.-X.; Chem. Mater., **2015**, *27*, 1905 - 1916.

[6] Strutt, N. L., Fairen-Jimenez, D., Iehl, J., Lalonde, M. B., Snurr, R. Q., Farha, O. K., Hupp, J. T. and Fraser Stoddart, J.; J. Am. Chem. Soc., **2012**, *134*, 17436 – 17439.

[7] Llewellyn, P. L., Bourrelly, S., Serre, C., Filinchuk, Y. and Férey G.; Angew. Chem. Int. Ed., **2006,** *45 (46)*, 7751 - 7754.

[8] Chen, B., Liang, C., Yang, J., Contreras, D. S., Clancy, Y. L., Lobkovsky, E. B., Yaghi O. M. and Dai S.; Angew. Chem. Int. Ed., **2006,** *45(9)*, 1390 – 1393.

[9] Choi, H. J., Dincă, M., Long, J. R.; J. Am. Chem. Soc., **2008**, *130 (25)*, 7848-7850.

[10] Kondo, A., Noguchi, H., Ohnishi, S., Kajiro, H., Tohdoh, A., Hattori, Y., Xu, W. C., Tanaka, H., Kanoh, H. and Kaneko, K.; Nano Letters, **2006**, *6 (11)*, 2581 - 2584.

[11] Wang, S.-Q., Yang, Q.-Y. Mukherjee, S., O'Nolan, D., Patyk-Kaz´mierczak, E., Chen, K.-J., Shivanna, M., Murray, C., Tangb, C. C. and Zaworotko M. J.; Chem. Commun., **2018**, *54*, 7042 – 7045.

[12] Klein, N., Hoffmann, H. C., Cadiau, A., Getzschmann, J., Lohe, M. R., Paasch, S., Heydenreich, T., Adil, K., Senkovska, I., Brunner, E. and Kaskel, S.; J. Mater. Chem., **2012**, *22*, 10303-10312.

[13] Mason, J. A., Oktawiec, J., Taylor, M. K., Hudson, M. R., Rodriguez, J., Bachman, J. E., Gonzalez, M. I., Cervellino, A., Guagliardi, A., Brown, C. G., Llewellyn, P. L., Masciocchi, N. and Long, J. R.; Nature, **2015**, *527*, 357–361.

[14] Zhu, A.-X., Yang, Q.-Y., Kumar, A., Crowley. C., Mukherjee, S., Chen, K.-J., Wang, S.-Q., O'Nolan, D., Shivanna, M. and Zaworotko, M. J.; J. Am. Chem. Soc., **2018**, *140 (46)*, 15572-15576.

[15] Shivanna, M., Yang, Q.-Y., Bajpail, A., Sen, S., Hosono, N., Kusaka, S., Pham, T., Forrest, K. A., Space, B., Kitagawa, S. and Zaworotko, M. J.; Science Adv., **2018**, *4 (4)*, eaaq 1636.

[16] Taylor, M. K., Runčevski, T., Oktawiec, J., Gonzalez, M. I., Siegelman, R. L., Mason, J. A., Ye, ., Brown, C. M. and Long, J. R.; J. Am. Chem. Soc., **2016**, *138 (45)*, 15019-15026.

[17] Takashima, Y., Martínez Martínez, V., Furukawa, S., Kondo, M., Shimomura, S., Uehara, H., Nakahama, M., Sugimoto K. and Kitagawa, S.; Nature Commun., **2011**, *2*, 1170, 1 - 8.

[18] Chandler, B. D., Enright, G. D., Udachin, K. A., Pawsey, S., Ripmeester, J. A., Cramb, D. T. and Shimizu G. K.; Nature Mater., **2008**, *7 (3)*, 229 – 235.

[19] Horcajada, P., Serre, C., Maurin, G., Ramsahye, N. A., Balas, F., Vallet-Regí, M., Sebban, M., Taulelle, F. and Férey, G.; J. Am. Chem. Soc., **2008**, *130 (21)*, 6774 – 6780.

[20] Rice, A. M., Martin, C. R., Galitskiy, V. A., Berseneva, A. A., Leith, G. A. and Shustova, N. B.; Chem. Rev., **2019**, DOI: 10.1021/acs.chemrev.9b00350 (ASAP article).

[21] Uemura, T., Hiramatsu, D., Kubota, Y., Takata M. and Kitagawa, S.; Angew. Chem. Int. Ed., **2007**, *46*, 4987 – 4990.

[22] Seo, J., Bonneau, C., Matsuda, R., Takata, M. and Kitagawa, S.; J. Am. Chem. Soc., **2011**, *133 (23)*, 9005 - 9013.

6. Porous organic polymers for photonic applications

6.1. Porous emitting frameworks for sensitiet-triplet up-conversion

6.1.1. Summary

This chapter illustrates the development of optically emissive porous aromatic frameworks nanoparticles (*e*PAFs) as advanced materials for sensitized triplet-triplet annihilation up-conversion (sTTA-UC). After an insight into the photophysics of sensitized upconversion process and a general introduction on emerging fully-organic porous materials for optical and photonic applications, the design principles, synthesis and characterization of *e*PAFs materials will be presented. ePAFs are nanometer-sized porous aromatic frameworks generated from Yamamoto-type Ullmann coupling of emitting moieties (4,4'-dibromo-(9,10-diphenyl)antracene, DPA) and rigid tetrahedral nodes (tetrakis(4-bromo-phenyl)methane, TPM) that build up highly porous three dimensional frameworks. The structural and chemical features of these materials have been investigated in detail with physico-chemical and spectroscopic techniques. Due to the non-conjugated nature of the overall framework, *e*PAFs display optical properties similar to the isolated DPA molecule in solution: the absorption and emission spectra and the high photoluminescence quantum yield (QY) of the diphenylanthracene strut are preserved in the condensed state. The photophysical behaviour of *e*PAFs allows the investigation of these materials for sensitized triplet-triplet upconversion in presence of a suitable sensitizer (Platinum octaethylporphhyrin, PtOEP). An optimized system displays an up-conversion quantum yield up to 15%, a record efficiency for a solid-state annihilator. Moreover, due to the easily tunable nature of the organic struts and the highly accessible surface area, we developed a modified porous frameworks bearing hydroxyl group that can be covalently post-functionalized with a sensitizer (Palladium mesoporphyrin IX, PdmesoIX) in order to produce self-standing up-converting nanoparticles that can be integrated in a device.

Related paper:

"Engineering Porous Emitting Framework Nanoparticles with Integrated Sensitizers for Low-Power Photon Upconversion by Triplet Fusion",

Authors: Perego, J.; Pedrini, J.; Bezuidenhout, C. X.; Sozzani, P.; Meinardi, F.; Bracco, S.; Comotti, A. and Monguzzi, A.

Adv. Mater, **2019**, *31*, 1903309.

6.1.2. Sensitized triplet-triplet annihilation up-conversion (s-TTAUC)

Different physical processes allow anti-Stokes shift of the incoming radiation generating higher energy photons from lower energy radiation [1,2]. Up-conversion processes have long been investigated in both inorganic and organic materials: the former employs lanthanide co-doped inorganic nanoparticles, while organic materials use couples of organic cromophores to harvest and convert the incoming radiation. Since the physical processes that led to this wavelength shift process are different for organic and inorganic materials, I will focus on the mechanism of sensitized triplet-triplet up-conversion process typical of organic systems. Sensitized Triplet-Triplet Annihilation Up-Conversion (sTTA-UC) allows an anti-Stokes shift of an incoming radiation due to a bi-molecular process involving a sensitizer/donor molecule and an emitter/acceptor chemical entity. The up-conversion process can be easily splitted up in the following steps:

- Excitation of the sensitizer molecule from its ground state (S_g) to its singlet excited state (^1S) *via* light absorption.
- Intersystem crossing from the singlet excited state of the sensitizer/donor molecule (^1S) to the triplet excited state of the same molecule (^3S).
- Energy transfer between the ^3S state of the sensitizer to the triplet excited state of the emitter (^3E).
- Exciton diffusion and triplet-triplet annihilation process.
- Fluorescence from the excited singlet state of the emitter (^1E).

The following scheme displays each step involved in sTTA-UC.

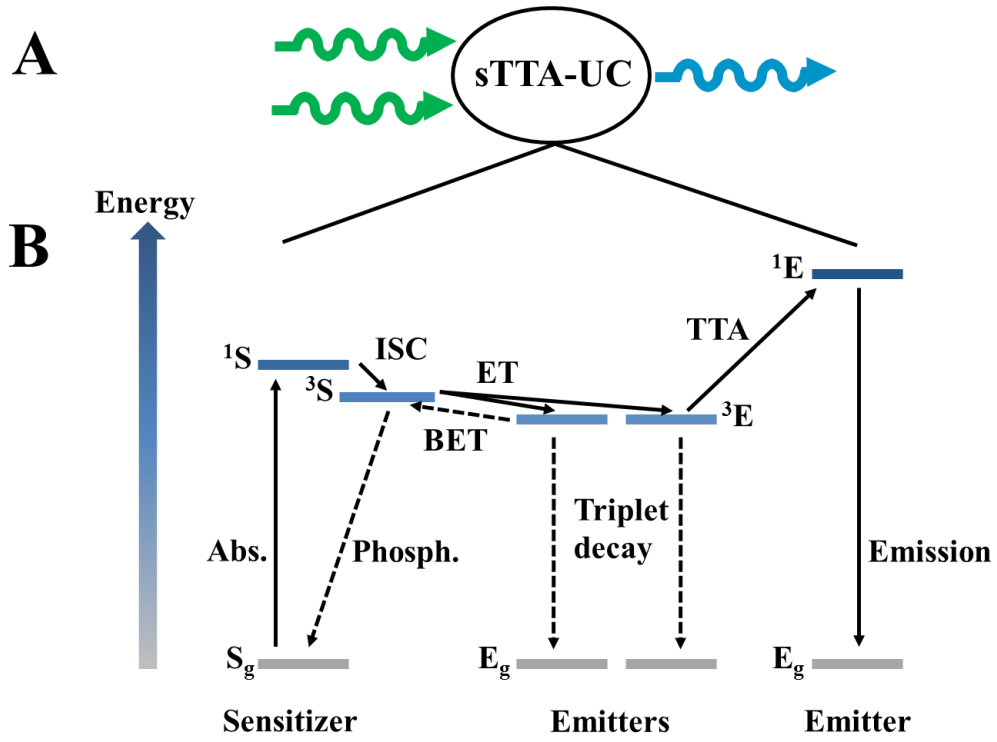

Scheme 1. A) Anti-Stokes conversion of two photons of low energy (green wavy arrows) in a higher energy photon (light blue wavy arrow). B) Simplified Jablonski diagram for sTTA-UC process.

The overall up-conversion quantum yield is related to the efficiency of each of the steps involved through the following equation[3]:

$$QY_{UC} = \frac{1}{2} f \varphi_A \varphi_{ISC} \varphi_{TTA} \varphi_{ET}$$

Where:

f = statistical parameter related to the probability to obtain a singlet state after the triplet-triplet annihilation process.

φ_A = Quantum efficiency of the emitter photoluminescence (PL).

φ_{ISC} = Quantum efficiency of sensitizer intersystem-crossing.

φ_{TTA} = Quantum efficiency of the triplet-triplet annihilation process.

φ_{ET} = Quantum efficiency of energy transfer between the sensitizer and the acceptor.

Parameters f and φ_{ISC} depend only on the chemical nature of the emitter and the sensitizer molecules, respectively. Instead, φ_A, φ_{TTA} and φ_{ET} depends also on the concentration and the chemical environment of the sensitizer and acceptor molecules.

s-TTAUC in solution is usually enabled by the high diffusivity of the molecular species that ensure the energy transfer between the sensitizer and the emitter molecules and the annihilation of two dark triplet generating the singlet excited state. In the solid state this process is slowed down for systems that feature a sensitizer/emitter couple dispersed in polymeric materials and it is suppressed inside rigid bulk materials. Thus, in the solid state, efficient triplet-triplet annihilation and high up-conversion yields can be obtained through an exciton diffusion mechanism, as discussed in more details in the next paragraph.

Sensitized triplet-triplet annihilation up-conversion allows photons wavelength shift even under low-power excitation and, possibly, under uncoherent solar irradiation. These properties are highly attractive in order to design passive optical materials that can increase solar power generation efficiency without changing the current leading technology of photovoltaic cells production (e.g. Silicon-based solar cells). It has been demonstrated that the Shockley-Quessier limit for single junction solar cells can be improved from 34 % up to 47.6 % by exploiting upconversion devices coupled with solar cells [4,5].

Low-power upconversion can easily be exploited in bioimaging and phototherapy. sTTA-UC allows the use of longer wavelengths in the NIR region that display higher penetration depth in human tissues. Up-converting nanoparticles can be exploited to obtain simultaneous imaging since they do not display any auto-fluorescence and phototherapy through light induced local production of reactive species or guest-release by drug loaded nano-carrier.[6,7]

Photocatalysis and photochemistry usually require U.V. light or high energy visible photons to work. Up-conversion can increase the yield of these processes by recovering the sub-bandgap photons that are usually lost during these processes or it can be employed to run these process under solar irradiation, without the need of particular excitation sources. [8]

6.1.3. S-TTAUC: towards solid state up-converters

The widespread use of up-conversion processes in photovoltaic, photocatalytic and photochemical applications relies mostly on the generation of suitable solid-state up-converting systems to overcome the major limitations related to the presence of a liquid phase. Moreover, the solid state can prevent effectively molecular oxygen diffusion that rapidly degrades the performance of materials since it quenches the triplet state involved in sTTA-UC process. The main limitation of solid-state up-converter devices is related to the poor diffusivity of molecules: while the excitation is generally transported by molecular motion in the liquid state, in solids this property must be replaced by the fast diffusion between different cromophoric units due to exciton diffusion. Many approaches have been exploited in the last years towards this goal and they are briefly summarized below.

Solvent-free up-converting systems can be generated by a proper design of the molecular units. For example, Kimizuka research group developed alkyl-functionalized acceptor molecules that are liquid at room temperature: the dissolution of suitable sensitizer generates highly efficient up-converting systems. [9,10]

Cromophoric pairs can be effectively put in close contact inside a gel formed by an external gelator (e.g. glutamic diamide LBG [11]) or they can be functionalized with side chains to build up a gel under suitable conditions [12].

A liquid phase environment can be maintained by encapsulating nano-droplets of a solution containing both the sensitizer and the acceptor molecules inside a rigid polymeric matrix. Vadrucci and coworkers showed that the radical polymerization of a miniemulsion containing a sensitizer/acceptor pair can generate bulk polymeric devices that enclose nanometer-sized droplets where the cromophoric units keep their diffusivity and allow the up-conversion process[13].

Sensitized triplet-triplet annihilation up-conversion has been realized in the solid state through different approaches. Molecular crystals of acceptor molecules can be doped with low concentration of sensitizer. However, this technique requires properly designed moieties to prevent segregation and phase separation of the two components in the solid solution. [14]. Metal organic frameworks provide a versatile platform for the development of up-converting materials since the different sensitizer/acceptor

pairs can be either introduced as structural elements that build up the structure of the material or the molecular species can be diffuse inside the pores of the material. Two main strategies have been developed. In 2015 Mahato et *al.* displayed the generation of up-converted emission from sensitizer-modified MOF nanocrystals. Three zinc-based MOFs with different spatial arrangement of the substituted diphenylanthracene ligand were synthetized and their optical properties were characterized. A fast dynamics of exciton diffusion inside the structures have been observed: this element is mandatory to obtain up-conversion processes in the solid state. Thus, a functionalized porphyrin has been covalently bounded at the surface to sensitize the up-conversion process: as expected the integrated system dispayed up-converted luminescence even if with low quantum yield. A similar approach have been recently reported for zirconium-based MOFs [15]. An alternative strategy have been developed by Zhou research group. The sensitizer presented carboxylic acid functionality that can compete with the linker during MOF synthesis and can be effectively included inside the defectual structure of the MOF. [7]

6.1.4. Porous organic frameworks for optical applications

Microporous polymers have been traditionally studied for applications related to their high surface area and microporosity as gas storage, separation and as inert substrate in heterogeneous catalysis. However, the high versatility of these materials provided by the rich synthetic chemistry that can be used to build their frameworks, and their possible post-synthetic modifications *via* chemical reactions, guest encapsulation and thermal treatment allow the design and synthesis of functional microporous polymers for advanced applications. In the last 10 years has been recognized and demonstrated that the aromatic backbone and the different degree of conjugation between monomeric units can be exploited to obtain favourable optical and photophysical properties. Some advances in the field of microporous polymers for optical application are summarized below.

Conjugated microporous polymers (CMPs) have fully-conjugated frameworks generated by the introduction of directly coupled aromatic or unsaturated bridges between conjugated building blocks. These structures can thus display extended

conjugation that led to interesting electronic and optical properties. An extensive work has been carried out by Cooper research group regarding the process of band-gap engineering in CMPs through different chemical strategies as co-monomer doping and the exploitation of these materials as hydrogen evolving catalysts[16,17,18].Jiang research group exploited CMPs for generating novel conducting frameworks for photonic and electrochemical applications [19,20].

To the best of my knowledge it is the first time that POFs have been designed and investigated for s-TTAUC.

6.1.5. Emitting porous organic frameworks for s-TTAUC

6.1.5.1. Synthesis and characterization of ePAFs

Fully-organic porous materials have been long studied as promising platforms to develop innovative optical and optoelectronic materials. Particularly, Conjugated Microporous Polymers (CMPs) have been intensively studied due to the possibility of fine-tuning optical and electronic properties due to their fully-conjugated aromatic backbone. CMPs allowed the control of energy bandgap due to the control of the spatial orientation of cromophores installed in their framework.

Instead, Porous Aromatic Frameworks (PAFs) have been less studied for potential optical applications, even if their potential in the field has been highlighted soon after the publication of the first example of this class of materials [21]. Due to the nature of their constituent building blocks and the coupling reactions that give raise to the 3D framework, PAFs contains electronically isolated aromatic building blocks due to the presence of sp^3 carbon atoms that disrupt the electronic conjugation. Due to this characteristic PAFs can be seen as a highly porous dielectric and insulating framework embedding cromophoric moieties electronically isolated one another that retain their distinctive optical properties, in stark contrast to CMPs, where the electronic conjugation between different building blocks defines the optical properties of the whole material. Moreover, the high surface area and micro- to mesopore range of pore size distribution allow the easy inclusion of a hosted phase by diffusion from

solution that can interact extensively with the functional moieties immobilized inside the framework.

Based on the above observation Porous Aromatic Frameworks have been designed for their application in sensitized Triplet-Triplet Annihilation Up-Conversion process (sTTA-UC). The polymeric nanoparticles comprise an extended three dimensional framework decorated with diphenylanthracene moieties (DPA) connected to four-branched rigid building blocks (tetraphenylmethane units, TPM). The materials have been synthetized through Yamamoto-type Ulmann coupling reaction in order to achieve high reaction yield and minimize the impurities and unreacted species in the solid material. Different monomeric feed ratios were employed to study how the density of cromophores inside the structure affects both the structural and optical properties of the material: three different samples (ePAF_1:1; ePAF_2:1 and ePAF_3:1) were synthetized with a molar ratio between the DPA and TPM moieties of 1:1, 2:1 and 3:1, respectively (see table 1 and experimental details at the end of the chapter). The two homo-polymers based on pure DPA (PolyDPA) and TPM (PAF-1) units have been synthetized in order to understand the different contribution due to the two different molecular struts inside the structures.

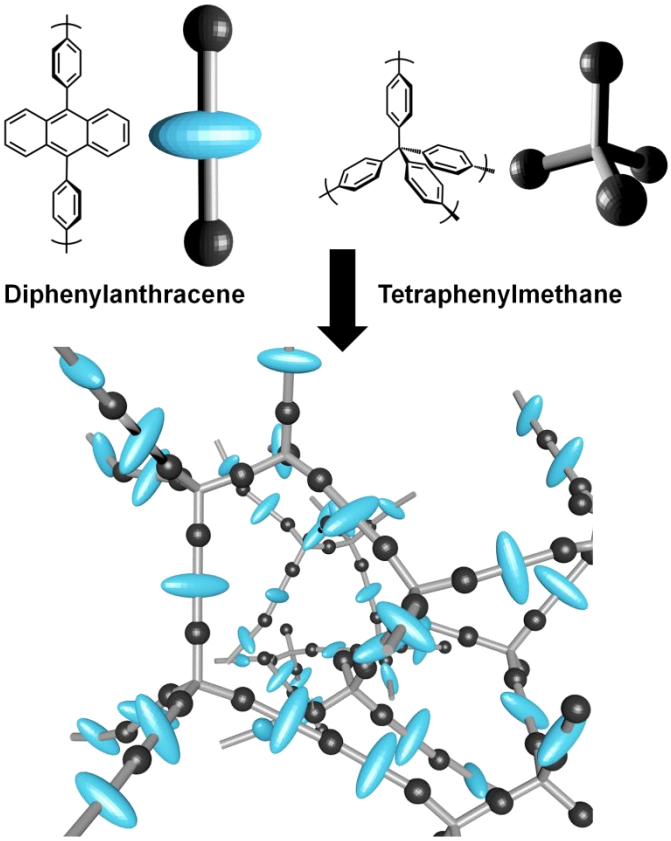

Scheme 2. Schematic representation of emitting porous aromatic frameworks. Diphenylanthracene moieties and tetraphenylmethane units are covalently bonded in an amorphous framework.

Table 1. Feed composition of materials described along this chapter (molar ratio between monomers).

Sample	**4,4' dibromo 9,10diphenylanthracene**	***tetrakis*- 4,4',4'',4'''-tetrabromophenylmethane**
PAF-1	-	1
*e*PAF_1:1	1	1
*e*PAF_2:1	2	1
*e*PAF_3:1	3	1
polyDPA	1	-

All materials have been characterized with multiple analytical techniques.

Nitrogen adsorption isotherms recorded at 77 K assess the porosity of the *e*PAFs: Langmuir and BET surface areas increase along with the amount of TPM moieties inside the structure up to values of 1140 and 1010 m^2/g, respectively (Table 2). All isotherms display a steep rise at low pressure due to microporosity and a constant increase of the gas uptake at higher pressures (> 0.05 p/p^o) related to mesoporous channels inside the structure. The hysteresis loop could be ascribed to a partial swelling of the framework and to the presence of constricted mesopores. Helium picnometry provides useful information since it allows the determination of skeletal density: this value can be exploited for total density calculations and it's fundamental for simulating amorphous structures.

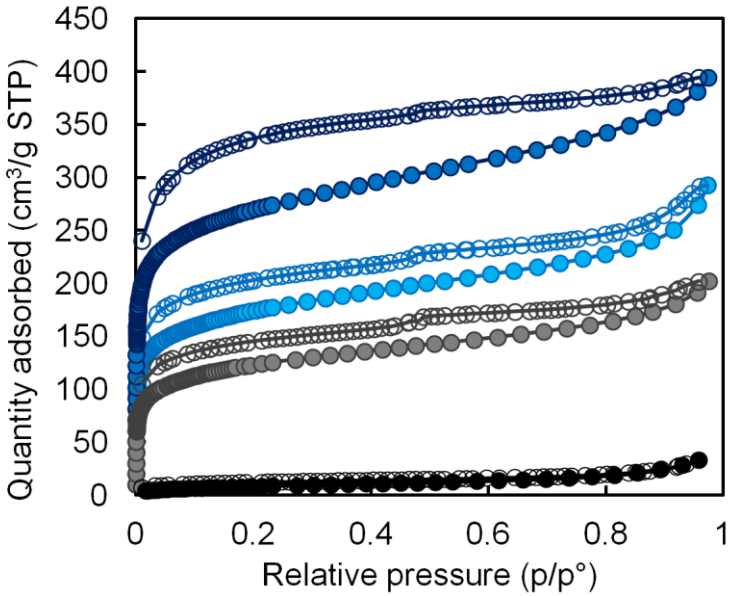

Figure 1. N_2 adsorption isotherms collected at 77 K of polyDPA (black), *e*PAF_3:1 (grey), *e*PAF_2:1 (light blue) and *e*PAF_1:1 (dark blue).

Table 2. BET and Langmuir surface areas of *e*PAFs calculated from nitrogen adsorption isotherms at 77 K and total pore volume calculated according to NL-DFT theory and carbon slit pore model. Experimental values of the density measured with helium-pycnometry and total density calculated from pore walls density and pore volume determined from nitrogen adsorption data.

Sample	BET surface area (m^2/g)	Langmuir surface area (m^2/g)	Total pore volume (cm^3/g)	Density (He pycnometry) (g/cm^3)	Density (total) (g/cm^3)
***e*PAF_1:1**	1010	1140	0.57	1.226	0.722
***e*PAF_2:1**	620	730	0.43	1.273	0.823
***e*PAF_3:1**	460	515	0.29	1.309	0.949
PolyDPA	30	30	0.05	1.310	1.230

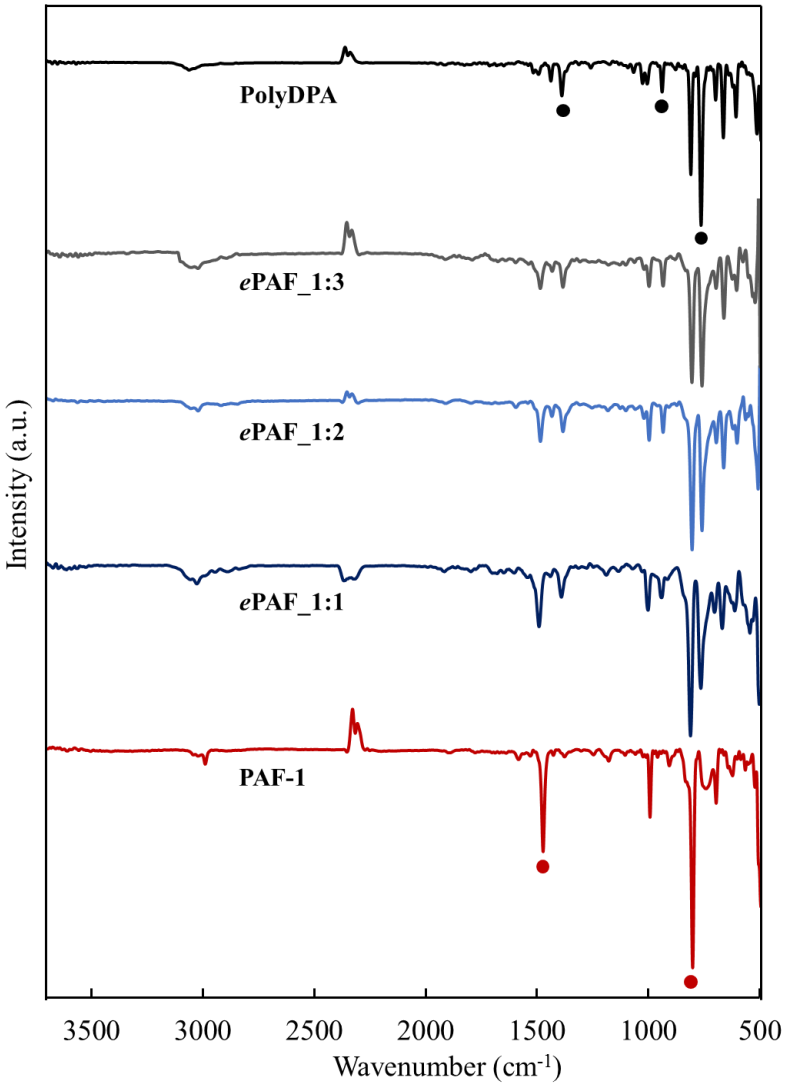

Figure 2. Infrared spectra of PAF-1 (pure tetraphenylmethane homopolymer, red), *e*PAF_1:1 (dark blue), *e*PAF_2:1 (light blue), *e*PAF_3:1 (grey), polyDPA (black).

Different spectroscopic techniques have been applied to assess the chemical purity and to determine the properties of these materials. Infrared spectroscopy allows to

qualitatively account for the composition of solids and confirms the success of Yamamoto coupling reaction (Figure 2). TPM units displays characteristic vibrational bands at 1492 cm^{-1}, 1005 cm^{-1} and 810 cm^{-1}. The vibration bands at 1492 cm^{-1} are due to semicircle stretching pair modes of the aromatic ring; the band at 1005 cm^{-1} is assigned to C-C and C-H bending, while the strong band at 810 cm^{-1} is due to ring and C-H out-of-plane bend (red dots). The vibration bands at 769 cm^{-1}, 942 cm^{-1} and 1391 cm^{-1} have been assigned to the C-H bending and C=C stretching vibrations of the anthracene ring (black dots). The relative intensities between the vibrational bands of DPA and TPM moieties increase with the increasing of DPA molar ratio in the feed composition of the coupling reaction.

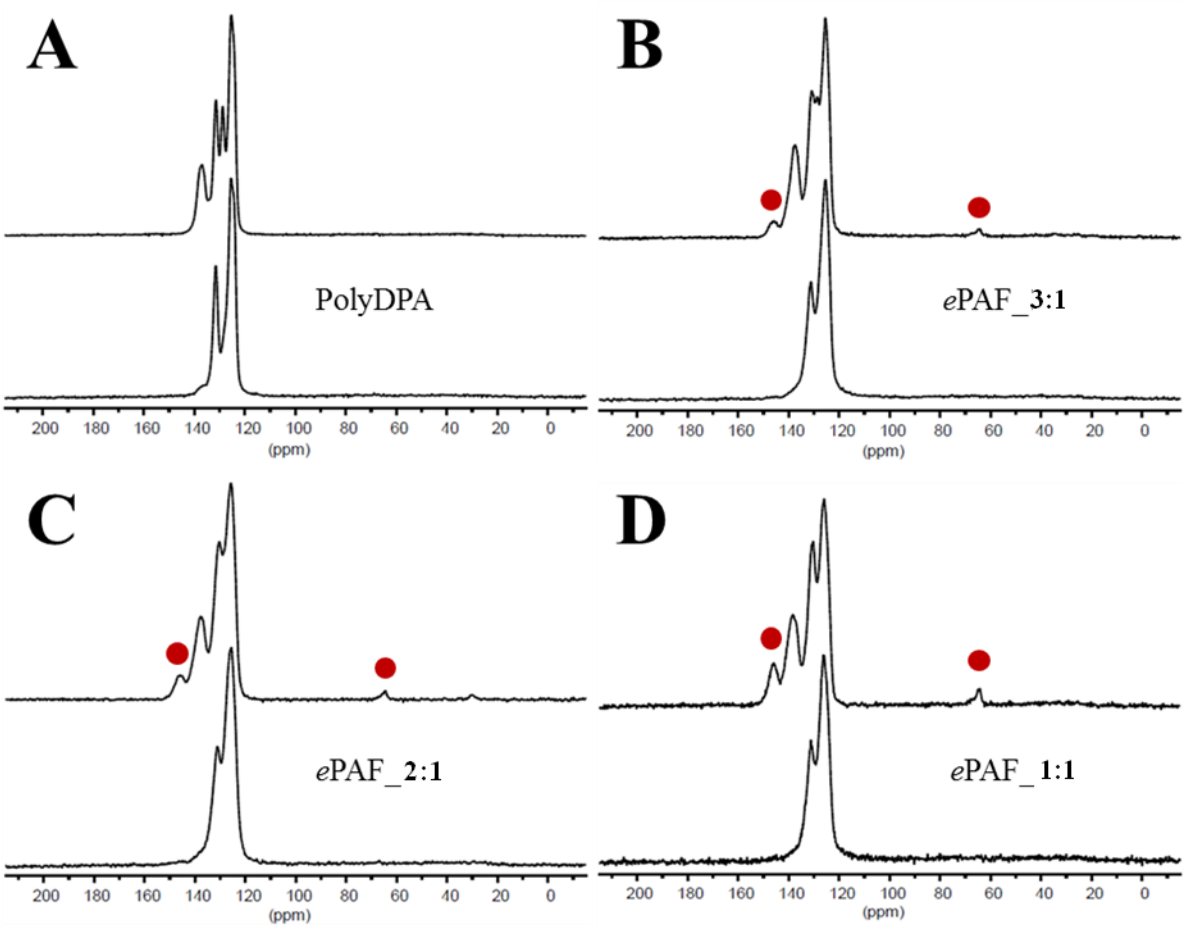

Figure 3. ^{13}C CP MAS solid state NMR spectra of A) PolyDPA, B) *e*PAF_3:1, C) *e*PAF_2:1 and D) *e*PAF_1:1 at different contact time (top: 2 ms; bottom: 50 µs). The characteristic peaks of tetraphenylmethane moiety are marked by red dots: their intensity qualitatively increase with the percentage of TPM in the feed ratio.

Solid state NMR spectroscopy is a powerful tool to study the composition and microstructure of porous aromatic polymers. ^{13}C CP MAS spectra for all the four sample have been measured at different contact time, 50 μs and 2 ms, respectively (Figure 3). At lower contact time the cross coupling between hydrogen and carbon nuclei is not effective for quaternary carbon atoms, thus the intensity of signals belonging to this atoms is strongly suppressed. The analysis of the spectra of polyDPA and PAF-1 allows for the identification and the assignement of characteristic peaks in the ^{13}C ss-NMR spectra. Specifically, the signals at 64.5 ppm and 146 ppm are due to the central quaternary carbon in TPM and the carbon that connects different TPM monomeric unit: due to their isolated position they can be used to quantify the composition of the final materials. Moreover, all samples display high chemical purity since no peaks belonging to other chemical species or impurities can be detected.

The samples were analysed with powder x-ray diffraction. All samples display common features: one broad peak around 25º 2θ degree typical of amorphous materials superimposed to a crystalline pattern that resembles the shape of the pattern from pure DPA homopolymer. Further discussion is presented later in the text.

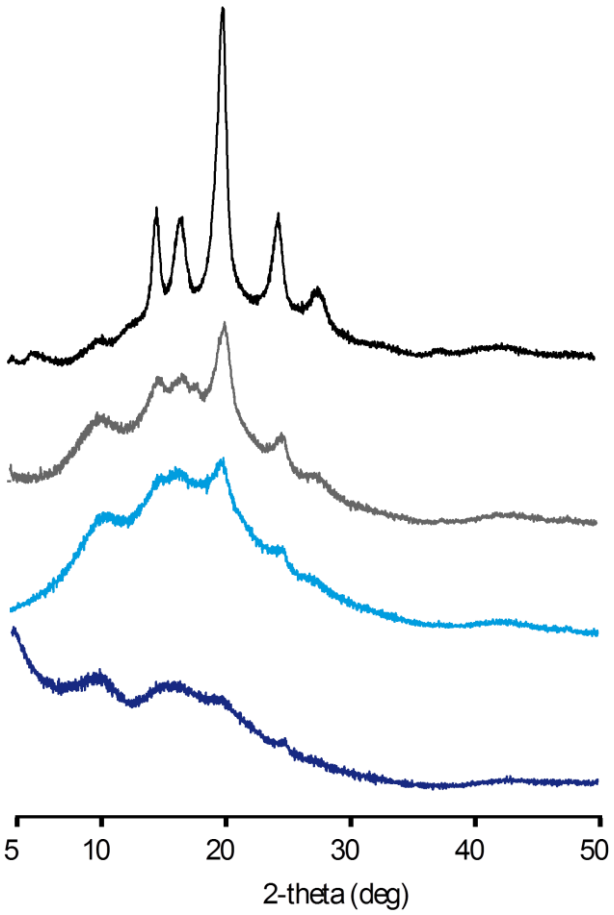

Figure 4. Powder x-ray diffraction patterns of polyDPA (black), *e*PAF_3:1 (grey), *e*PAF_2:1 (light blue) and *e*PAF_1:1 (dark blue).

Finally, all samples display high thermal stability proved by thermogravimetric analysis: under oxidative conditions (dry air) less than 5% weight loss takes place up to 400°C, while at higher temperature complete combustion of the organic frameworks leaves no residual mass (Figure 5).

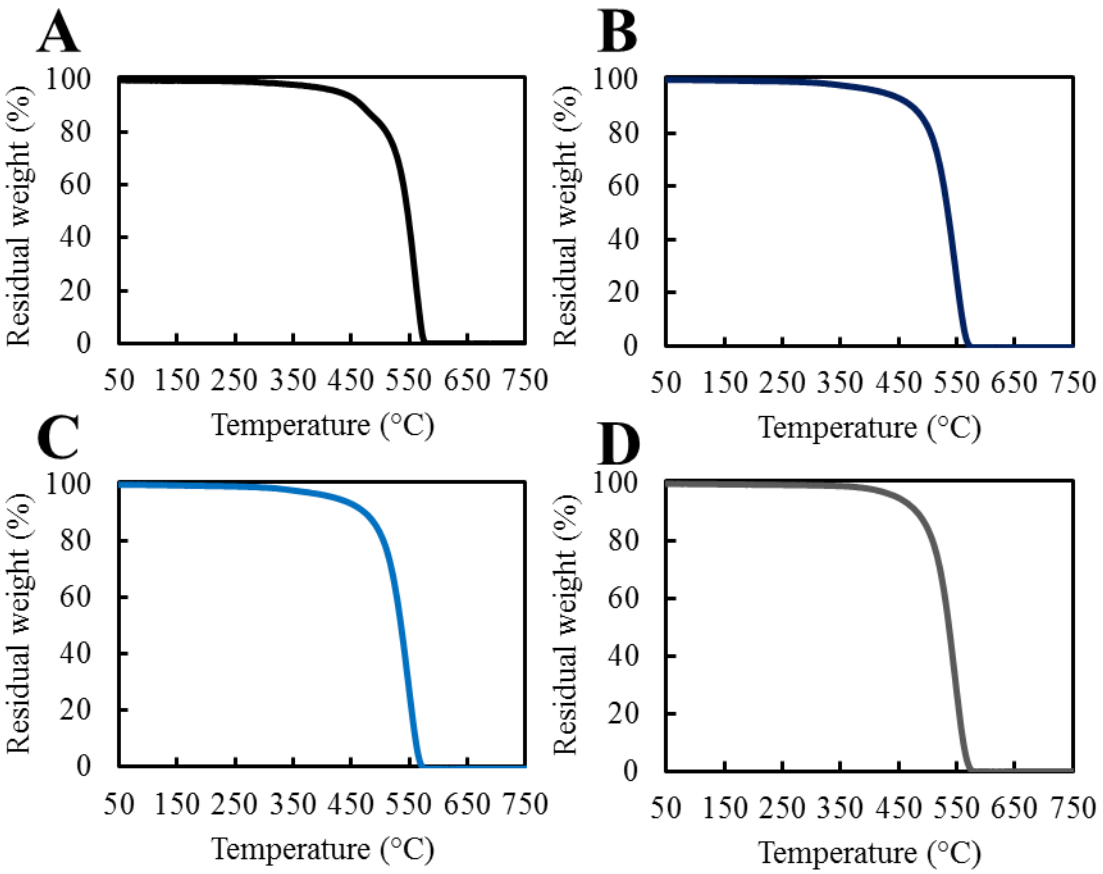

Figure 5. Thermogravimetric analysis of A) PolyDPA (black), B) *e*PAF_1:1 (dark blue), C) *e*PAF_2:1 (light blue) and D) *e*PAF_3:1 (grey) (10 K/min in dry air).

All samples have been preliminary characterized with optical measurements thank to a fruitful collaboration with Prof. A. Monguzzi research group at University of Milan-Bicocca. Dilute dispersion of ePAFs display optical absorption and emission spectra similar to the free diphenylanthracene molecule in solution. Time-resolved photoluminescence highlights lower radiative lifetime of ePAFs than for diphenylanthracene molecules in solution pointing at the effective inclusion of DPA moieties in a stable framework.

6.1.5.2. ePAF_2:1. Optical properties and sensitized up-conversion

In order to study the upconversion properties of these materials we selected the sample *e*PAF_2:1 since it displayed higher photoluminescence quantum yield. The deconvolution of ^{13}C MAS NMR spectrum recorded with long recycle time (100s) allows to calculate the relative molar ratio between DPA and TPM moieties (0.66 : 0.34 ratio) that is in excellent agreement with the feed composition of the Yamamoto coupling (2 : 1 ratio) (Figure 7). The morphology of the sample has been studied with scanning electron microscopy (SEM) and the particle size has been independently evaluated *via* dynamic light scattering (DLS) measurement to confirm the homogeneity of the entire sample and the even particle distribution. SEM analysis revealed nanometer-sized spherical particles with a sharp distribution peaked at about 145 nm (Figure 8), a value similar to the one obtained from DLS measurement (142 nm). The broader tail in the DLS peak around hundreds of nanometers is due to the presence of small aggregates of nanoparticles inside the dispersion.

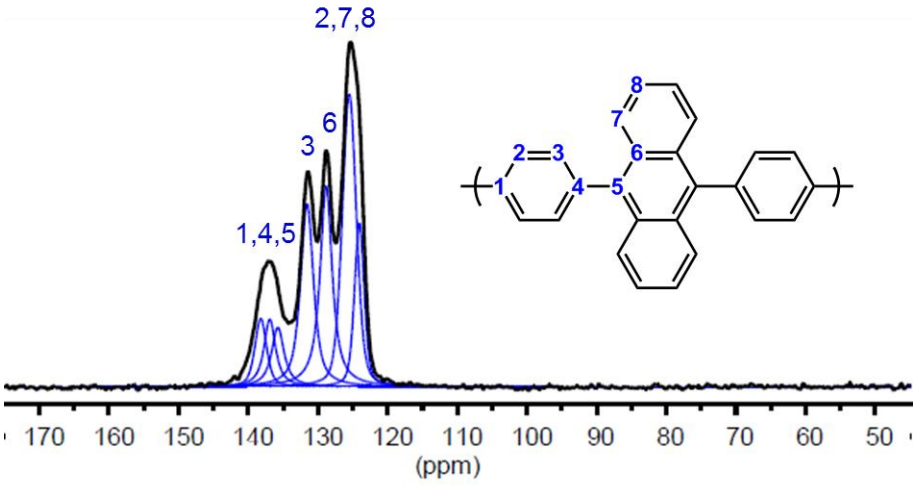

Figure 6. ^{13}C MAS spectrum of polyDPA. The peaks has been assigned according to literature data and deconvoluted using Gaussian and Lorentzian line shapes.

Carbon	Chemical shift (ppm)
C_8	124.4
C_2 C_7	125.4
C_6	128.8
C_3	131.5
C_5 C_4 C_1	134-136

Carbon	Chemical shift (ppm)
C_9	64.3
C_{10}	125.2
C_{11}	131.3
C_{12}	139.8
C_{13}	146.2

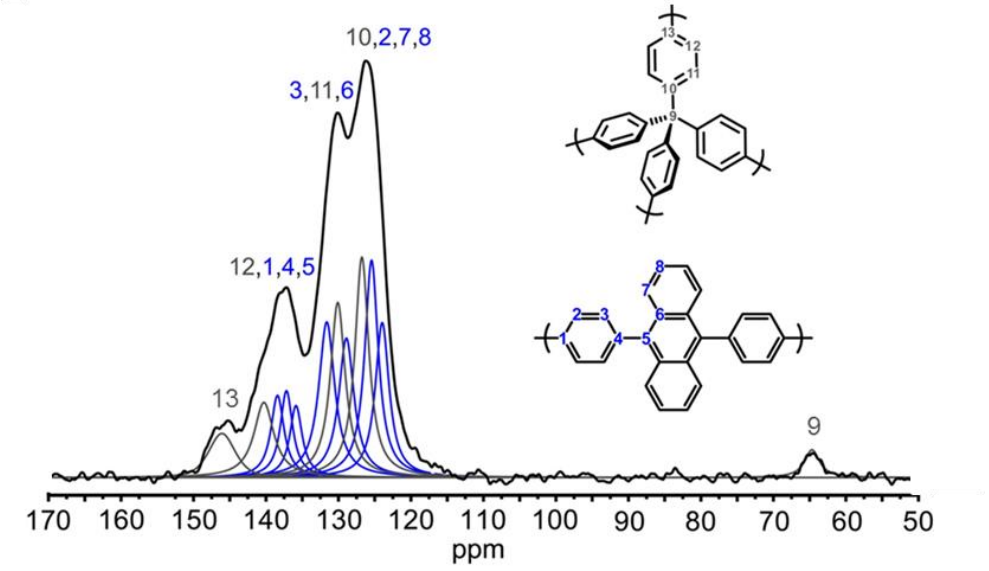

Figure 7. ^{13}C MAS solid state NMR spectrum of *e*PAF_2:1. The spectrum has been deconvoluted using Lorentzian and Gaussian lineshapes.

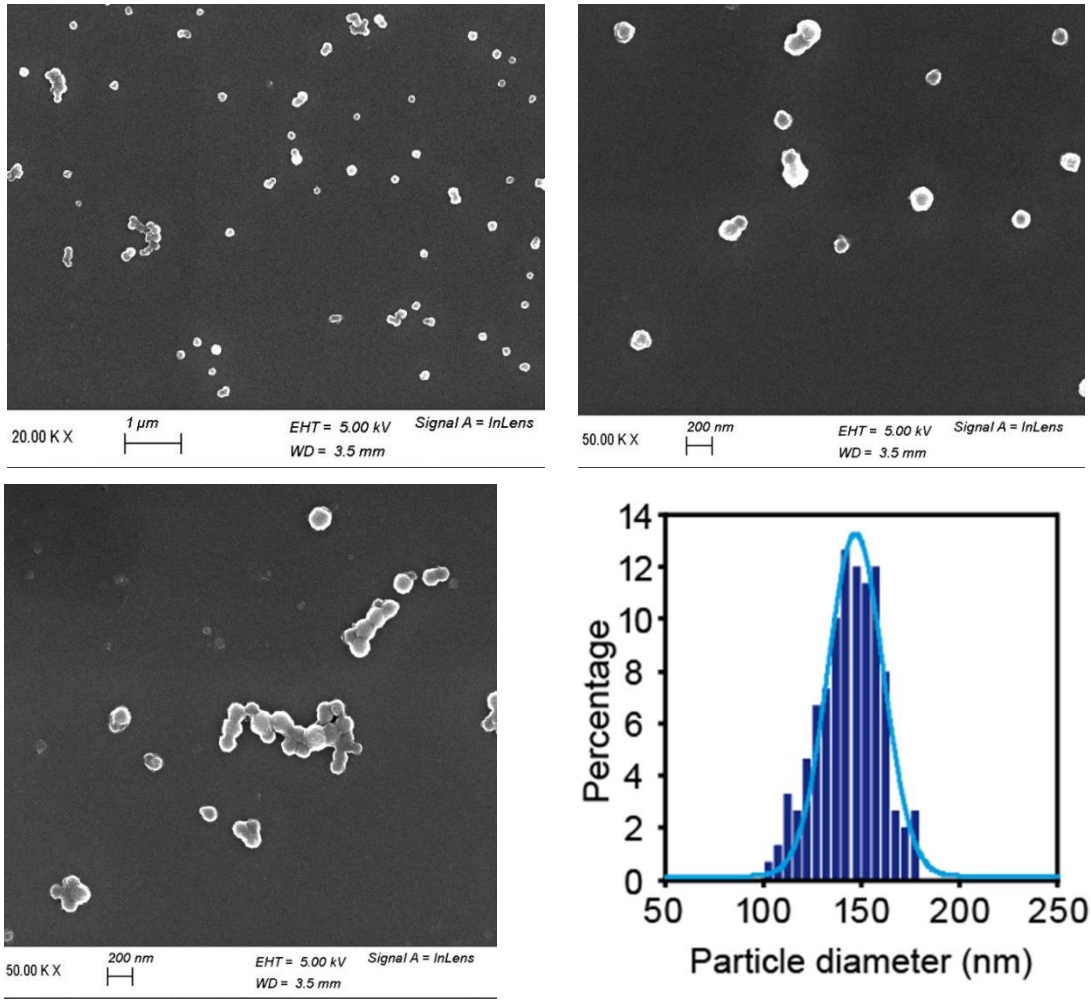

Figure 8. Scanning electron microscopy images of *e*PAF_1:2 at different magnification. The particle size distribution has been calculated by measuring around 150 particles from different images.

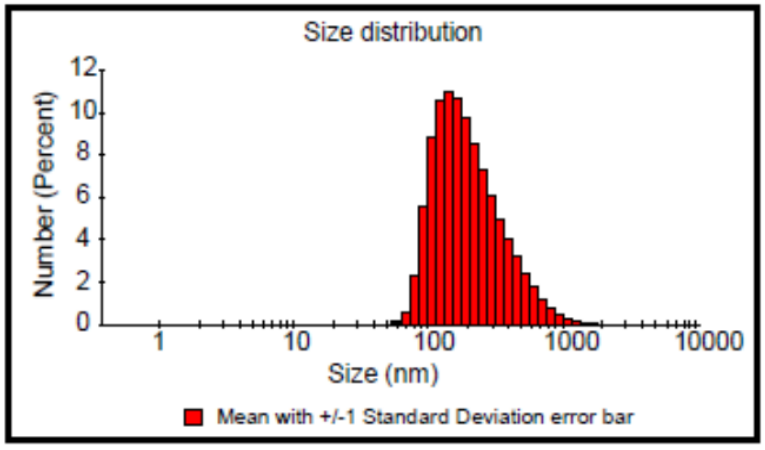

Figure 9. Particle size distribution of a dispersion of *e*PAF_1:2 in THF measured by DLS.

In order to understand the microstructure of the material we perform powder x-ray diffraction and simulate the pattern by means of a superposition of an amorphous phase and a crystalline phase. The ratio between the integrals relative to the amorphous and crystalline phase can be used as a rough indication of the relative percentage of the two phases inside the sample: from this calculation the crystalline phase content account for about 10% of the material or less. Peaks associated with the crystalline phase matches the powder diffraction pattern of the pure homopolymer sample (polyDPA): starting from this experimental pattern the structure of the material has been successfully modelled by Dr. Charl X. Bezuidenhout. The refined structure of the homopolymer has been showed in the Experimental details at the end of the chapter.

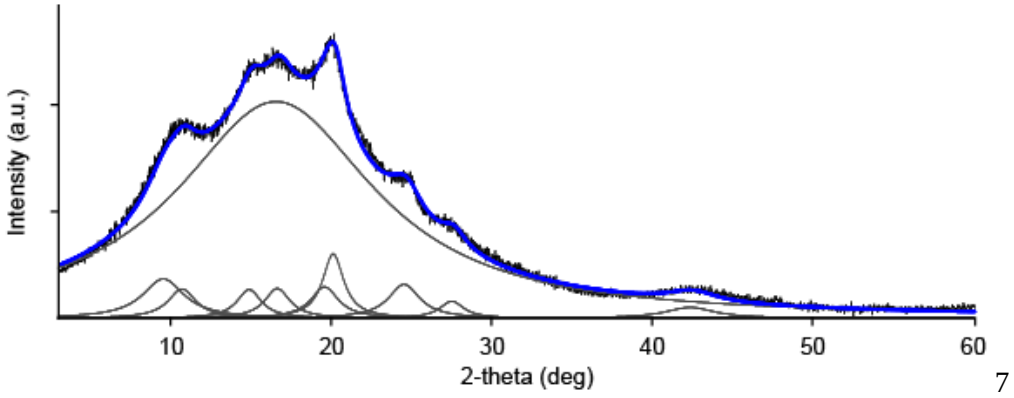

7

Figure 10. Experimental (black) and simulated (blue) powder x-ray diffraction pattern of *e*PAF_2:1. The amorphous and crystalline simulated peaks are shown in grey.

The photophysical properties of *e*PAF_2:1 have been investigated by suspending the material in benzene. The U.V.-visible absorption spectrum perfectly matches the spectrum of diphenylanthracene molecules dissolved in the same solvent: they are both peaked at 375 nm and exhibit the same vibronic structure, excluding the presence of any aggregated species. The emission spectrum measured under continuous wave excitation at 340 nm displays a bright luminescence centered at 435 nm, similar to isolated DPA molecules. Time-resolved photoluminescence spectrum shows a single exponential decay with a lifetime of 3.9 ns, comparable to that of isolated DPA and the photoluminescence quantum yield is 66 ± 7 %, very promising for a solid state

material. All these observation demonstrate that the electronic properties and the photoluminescence of emitters required for up-conversion are preserved in the rigid framework.

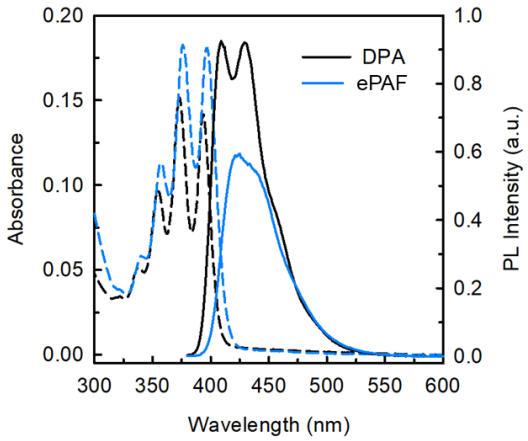

Figure 11. Absorption (dashed lines) and fluorescence (solid lines, measured with excitation wavelength of 340 nm) spectra for a 10^{-4} M DPA solution (black lines) and an ePAFs dispersion (blue lines).

ePAFs have been tested as annihilator for sTTA upconversion. It has been suspended in de-oxygenated benzene and the triplet sensitizer platinum octaethylporphyrin (PtOEP) has been added: the sensitizer can diffuse within the porous structure and experience energy transfer (ET) towards the framed emitters. Excitation with a 532 nm continous wavelength produces the clear blue luminescence of DPA moieties and proves the effective energy transfer between the sensitizer and the annihilator embedded inside the porous framework. No emission is detected in an *e*PAF dispersion without PtOEPs.

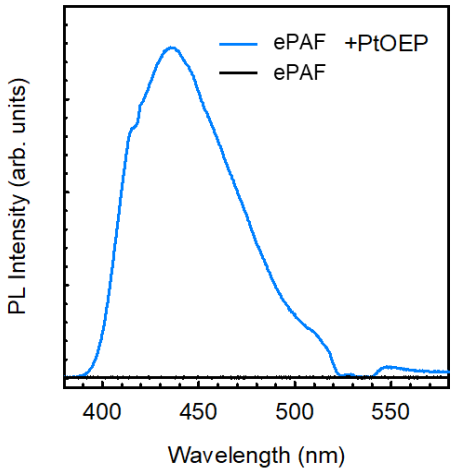

Figure 12. Photoluminescence spectrum of the *e*PAFs dispersion in benzene with and without PtOEP sensitizers, under continous wave excitation at 532 nm.

The efficiency of *e*PAFs as upconverters is further supported by plotting the upconversion quantum yield (QY) as a function of excitation intensity. Since s-TTAUC is a bimolecular process the power dependence display of up-converted emission against the excitation intensity displays a complex behaviour: the emission increases along with the excitation power until it reaches a plateaux value when the triplet-triplet annihilation rate is maximized. The increase in up-converted emission with excitation power and the increase in up-conversion efficiency are reported below.

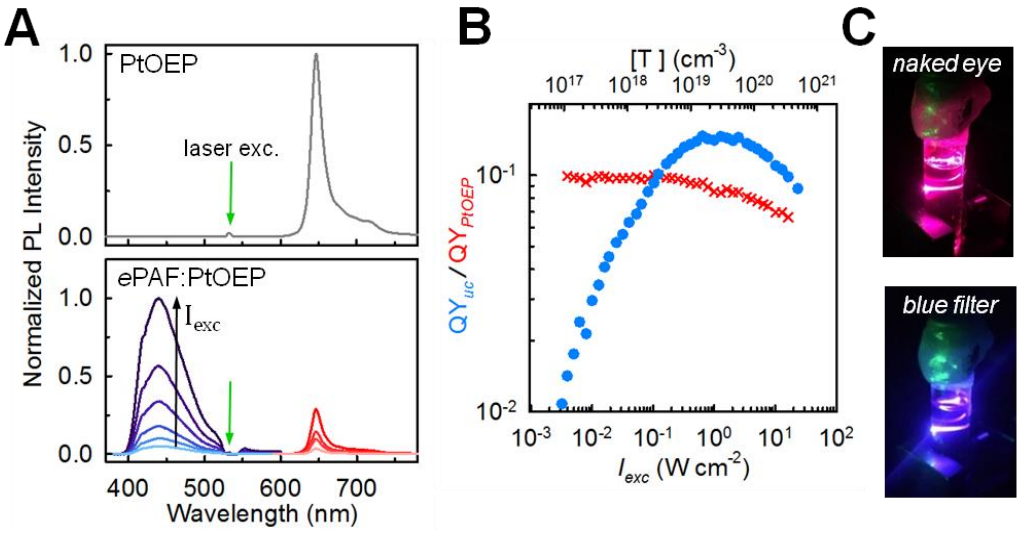

Figure 13. A) Photoluminescence (PL) spectrum of a benzene solution of PtOEP (10^{-4} M) under 532 nm laser excitation without (top) and with (bottom) ePAFs. B) Upconversion

quantum yield (dots) and residual phosphorescence yield of PtOEP (crosses) as function of the excitation intensity (532 nm). C) Images of the sample under laser excitation at 532 nm with and without a blue optical filter.

The maximum achievable quantum yield of up-conversion is 15 %: this is a record value for *s*TTA up-conversion obtained using solid state emitters as annihilators and it is comparable to that of the optimized free-molecule based solution up-converters.

6.1.5.3. i-ePAF_OH. Self-standing up-converting nanoparticles

Since *e*PAF_2:1 displayed high up-conversion efficiency in dispersion in presence of the sensitizer PtOEP, we designed a porous material containing DPA units and a different pore generating building block, tris(4-bromo-phenyl)methanol (TPMOH). This building block provides a three dimensional node that ensures the formation of an extended, cross-linked and porous framework and contains a reactive hydroxyl group on the ternary carbon atom suitable for post-synthetic functionalization reaction. We synthetized a porous framework with a 2:1 ratio of DPA and TPMOH building blocks (*e*PAF_OH) and then we functionalized it with PdmesoIX exploiting an estherification reaction (see Experimental details) to obtain self-standing up-converting nanoparticles containing both the sensitizer and the emitter tethered one another (*i*-*e*PAF_OH).

*e*PAF_OH has been extensively characterized with different techniques. Nitrogen adsorption isotherms at 77 K were collected and a Langmuir and BET surface areas of 480 m^2/g and 420 m^2/g were calculated.

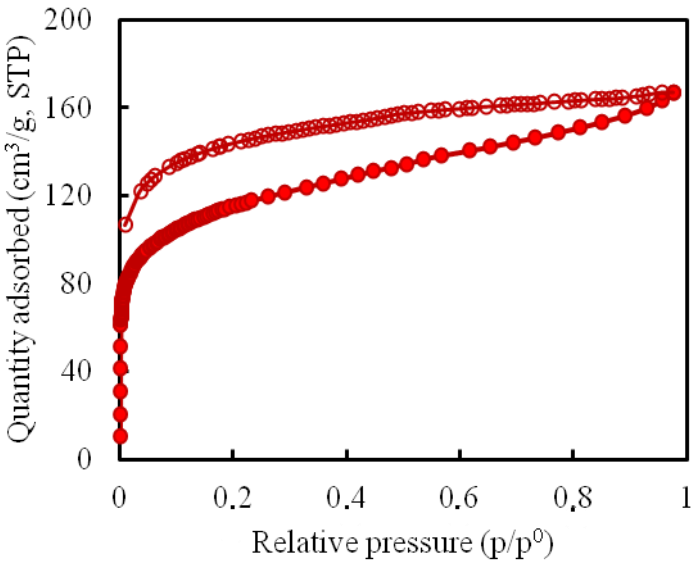

Figure 14. Nitrogen adsorption isotherm of *e*PAF_OH measured at 77 K.

The chemical purity and the structure of the material have been studied by means of solid state NMR spectroscopy and p-XRD. ^{13}C CP MAS solid state NMR spectroscopy proved the chemical purity of the material and highlighted the retainment of the hydroxyl units inside the porous framework.

Carbon	Chemical shift (ppm)
C_8	124.4
C_2 C_7	125.4
C_6 (q)	128.8
C_3	131.5
C_5 C_4 C_1 (q)	134-136

Carbon	Chemical shift (ppm)
C_{13}	81.3
C_{10}	126.3
C_{11}	128.1
C_9 (q)	140.1
C_{12} (q)	146.1

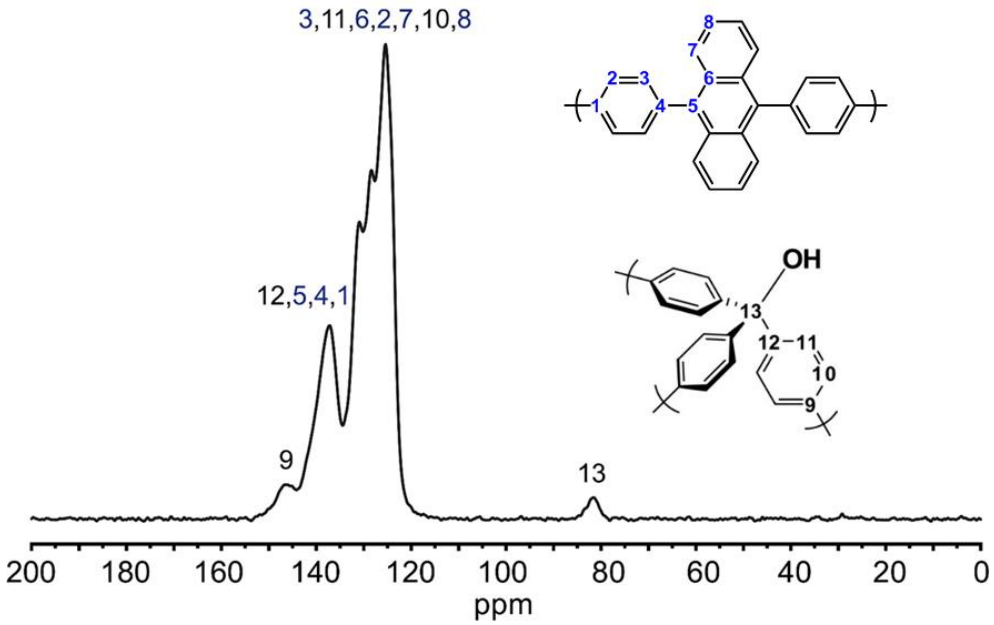

Figure 15. ^{13}C CP MAS solid state NMR spectrum of *e*PAF_OH. The signal at 81.3 ppm is due to the central carbon of the triphenylmethanol unit.

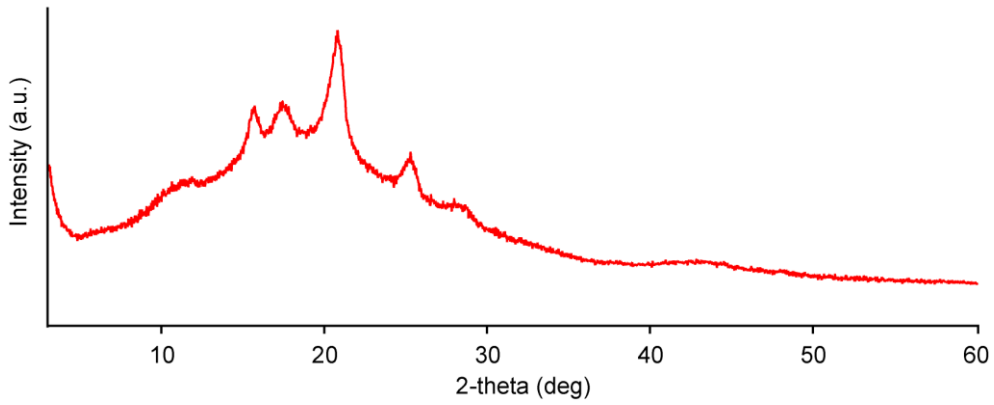

Figure 16. Powder x-ray diffraction pattern of *e*PAF_OH measured from 3 to 60 2θ degrees.

Bi-molecular nanoparticles containing both the emitter (DPA) and the sensitizer moiety (PdmesoIX) have been obtained *via* a post-synthetic reaction. Briefly, *e*PAF_OH has been treated with thionyl chloride to generate highly reactive trityl chloride sites inside the porous framework; then, the solid sample has been suspended with Pd mesoporphyrin IX and stirred for 16 hours after 3 freeze-pump and thaw cycles to allow the diffusion of the sensitizer inside the pores of the 3D framework

(See Experimental details). Thus, we obtained self-standing up-converting nanoparticles with a tethered sensitizer inside the pores and on the external surface of the material (*i-e*PAF_OH) . The success of the post-synthetic functionalization reaction has been proved with infrared spectroscopy monitoring the variation of the vibrational band of carboxylic acid moieties of Pd mesoporphyrin IX from 1705 cm^{-1} in the free acid to 1730 cm^{-1} after the esterification reaction. Moreover, elemental analysis highlighted the increase in nitrogen content related to the pyrrole moieties of porphyrin and SEM-EDX analysis showed the effective incorporation of palladium.

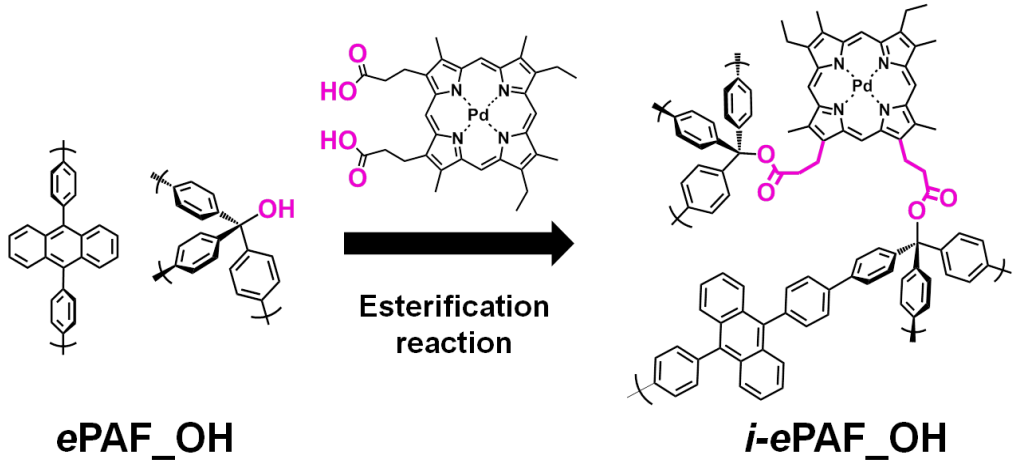

Figure 17. Scheme of the post-synthetic functionalization of *e*PAF_OH with Pd Mesoporphyrin IX *via* esterification reaction.

In the U.V.-visible range *i-e*PAF_OH shows a multiband absorption profile, with an intense band that peaks at 400 nm, due to the overlap of DPA and PdMesoIX absorption bands and a weaker band centered at 550 nm due to the characteristic absorption *Q*-band of PdMesoIX. From the molar exciton coefficient of dyes the amount of PdMesoIX can be extimated to a porphyrin/DPA molar ratio of 0.13, in excellent agreement with the elemental analysis results.

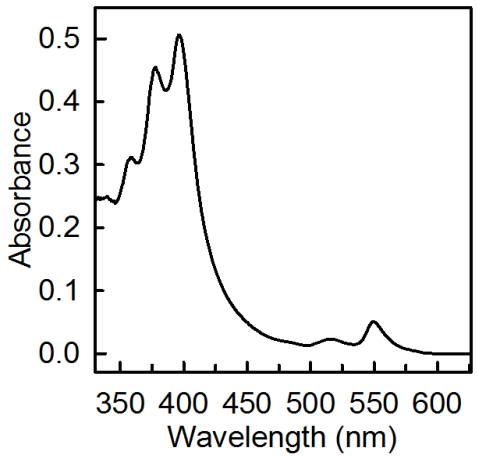

Figure 18. Absorption spectrum of *i*-*e*PAF_OH dispersion in benzene.

The up-conversion properties of *i*-*e*PAF_OH has been studied in benzene dispersion. The dispersion shows a power-dependent upconverted emission peaked at 435 nm under 532 nm continous wave laser excitation. No emission from PdMesoIX is detectable, suggesting a quantitative ET to DPA triplets due to the close distance between the two moieties. Plotting the quantum yield of up-conversion against the excitation power in a log-log scale shows again the typical behaviour of *s*TTA-upconversion in bulk. The efficiency increases until a saturation plateau is reached at quantum yield = 0.7%. Moreover, up-conversion measurements at different *i*-*e*PAF_OH concentrations provide further evidence of the stable link between sensitizers and emitters: a linear dependence between the up-converted emission and the nanoparticles concentration has been observed in a range of two order of magnitudes pointing at the formation of a self-standing integrated up-converting material.

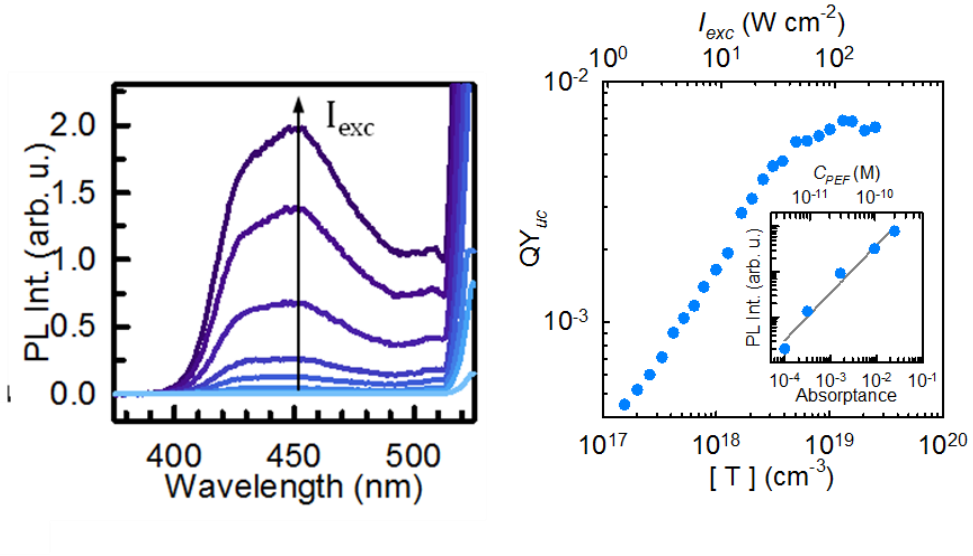

Figure 19. Left: up-converted photoluminescence spectrum as a function of the excitation intensity (excitation wavelength = 532 nm). Right: up-conversion efficiency versus excitation intensity of *i*-*e*PAF_OH. Inset: Integrated up-converted photoluminescence intensity as a function of the *i*-*e*PAF_OH concentration: a linear dependence can be extrapolated.

6.1.6. Conclusion

In summary, fully organic nanosized fluorescent porous emitting frameworks built up of covalently bonded emitter ligands have been designed and synthesized to host low power up conversion based on triplet–triplet annihilation (TTA). The synthetic route developed exploited optically active moieties as building blocks for fabricating a homogeneous covalent organic network without affecting the electronic properties of the individual emitters. This enabled the diffusion and annihilation of triplet excitons, both pivotal for the TTA process that produces high-energy photons. The upconverted emission has been generated upon sensitization of triplet excitons through a molecular light harvester diffused into the pores (PtOEP) achieving a record conversion efficiency of 15% in a covalently linked framework of emitters. Moreover, exploiting the great accessibility of the framework we could intimately link the sensitizer by tethering it to the framed emitters. This allowed to achieve the final goal to engineer a bicomponent fluorescent porous emitting framework. Proper covalent bonds enabled both the insertion of the emitters in the framework and a stable incorporation of the sensitizer molecules into the nanoparticle architecture, without segregation or

aggregation, resulting in nanosized individual upconverters. The possibility to host secondary active species in the pores and, importantly, by tailoring the framework composition through primary or post-synthetic approaches strongly support the potential of these novel nanomaterials as benchmark emitters, whose optical and photoluminescence properties can be tuned to fit the specific demands of applications such as imaging, photocatalysis, and photon managing.

6.1.7. Experimental details

Synthetic procedure

Solvents and reagents were purchased by Sigma-Aldrich and used without any purification. Dry tetrahydrofuran was distilled from sodium/benzophenone in a continuous distillation apparatus. The synthetic procedures for p-dibromo-(9,10-diphenyl)antracene, tetrakis(4-bromo-phenyl)methane and tris(4-bromo-phenyl)methanol were reported in literature. The synthetic schemes for the monomers were reported below.

Synthesis of ePEFs and ePEF-OH. Nanosized porous organic frameworks were synthetized through a Nickel activated Yamamoto coupling reaction. Bis(1,5-cyclooctadiene)nickel(0) ($Ni(COD)_2$) (2g; 7.27 mmol) was added to a solution of cis,cis-1,5-cyclooctadiene (COD) (1.1ml; 8.97 mmol) and 2,2'-bipyridine (1.1g; 7.04 mmol) in a dry THF/DMF mixture (120ml/180ml) under nitrogen atmosphere. The resulting mixture was stirred for 15 minutes in an ice/water bath. Then, the brominated monomers were dissolved in dry THF (60 ml) and added dropwise over 20 minutes under vigorous stirring (the feed compositions for *e*PEFs and *e*PEF-OH are reported in the table below). The dark purple solution was stirred in the dark for 72 h and then quenched by adding 30 ml of a 3 M aqueous HCl solution. After 4 hours the solid materials was filtered on a 0.1 μm PTFE filter and washed with THF (3x50ml), water (3x50ml), dichloromethane (3x50ml) and acetone (50 ml). The solid material was recovered and dried at first at room temperature and then at 120°C overnight. To obtain a homogeneously dispersed sample of PEF nanoparticles in THF,

the dispersion was filtered through a 0.45 µm PTFE filter. This procedure allowed the isolation of nanoparticles with a sharp particle size distribution and ensure a homogeneous dispersion.

Table 3. Monomeric feed composition of *e*PEF and *e*PEF-OH.

PAF-1	**Quantity (mmol)**	**Molar ratio**
9,10-di(4-bromophenyl)anthracene	-	-
Tetrakis-(4-bromophenyl)methane	1.50	-
***e*PAF_1:1**	**Quantity (mmol)**	**Molar ratio**
9,10-di(4-bromophenyl)anthracene	0.97	1
Tetrakis-(4-bromophenyl)methane	0.97	1
***e*PAF_2:1**	**Quantity (mmol)**	**Molar ratio**
9,10-di(4-bromophenyl)anthracene	1.46	2
Tetrakis-(4-bromophenyl)methane	0.73	1
***e*PAF_3:1**	**Quantity (mmol)**	**Molar ratio**
9,10-di(4-bromophenyl)anthracene	1.75	3
Tetrakis-(4-bromophenyl)methane	0.58	1
PolyDPA	**Quantity (mmol)**	**Molar ratio**
9,10-di(4-bromophenyl)anthracene	2.92	-
Tetrakis-(4-bromophenyl)methane	-	-
***nano*PEF-OH**	**Quantity (mmol)**	**Molar ratio**
9,10-di(4-bromophenyl)anthracene	1.46	2
tris(4-bromo-phenyl)methanol	0.73	1

Synthesis of modified *i-e*PEF. *e*PEF-OH was evacuated overnight at 100°C. The solid ePEF-OH (25 mg) was dispersed in 5 ml of dry dichloromethane and cooled to 0°C. Then, 15 µL of thionyl chloride ($SOCl_2$) were added to the dispersion followed by 3 freeze-pump-thaw cycles to increase the diffusion of the molecular species inside the pores. The mixture was stirred for 8h at room temperature before solvent removal and the solid PEF was activated overnight at room temperature in high vacuum. Pd(II) mesoporphyrin IX (7 mg) was dissolved in a mixture of THF/MeOH (20 ml) and treated with a stoichiometric amount of sodium hydroxide to obtain its disodium salt. The precipitate was filtered and washed with THF and few drops of methanol. The porphyrin disodium salt and the activated *e*PEF-OH were dispersed in dry THF (30 ml), are subjected to 3 freeze-pump-thaw cycles and stirred for 16 hours at 50°C. At last, the dispersion was cooled down to room temperature, the solid was filtered under nitrogen and washed with dry THF (300 ml) before drying under vacuum.

Crystal structure of PolyDPA.

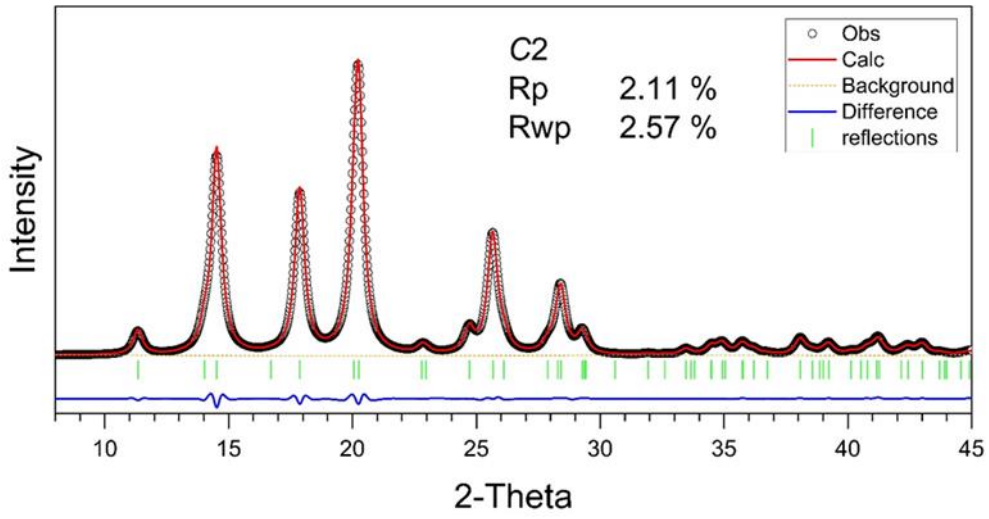

Figure 20. Rietveld refinement of powder x-ray diffraction pattern of polyDPA. The pattern was refined using the TOPAS-Academic-64 V6 software package S5. The black and red lines represent the experimental and calculated traces, respectively. The green lines indicates HKL indices.

Table 4. Crystallographic data for the PXRD Rietveld refinement of activated PolyDPA.

Identification code	**PolyDPA**
Empirical formula	$C_{16}H_8$
Formula weight	200.22
Temperature/K	293(2)
Crystal system	Monoclinic
Space group	*C*2
a/Å	10.200
b/Å	12.608
c/Å	6.269
α/°	90
β/°	76.43
γ/°	90

Volume/$Å^3$	783.7
Z	4
$\rho_{calc}g/cm^3$	1.697
Rp	2.11 %
Rwp	2.57 %

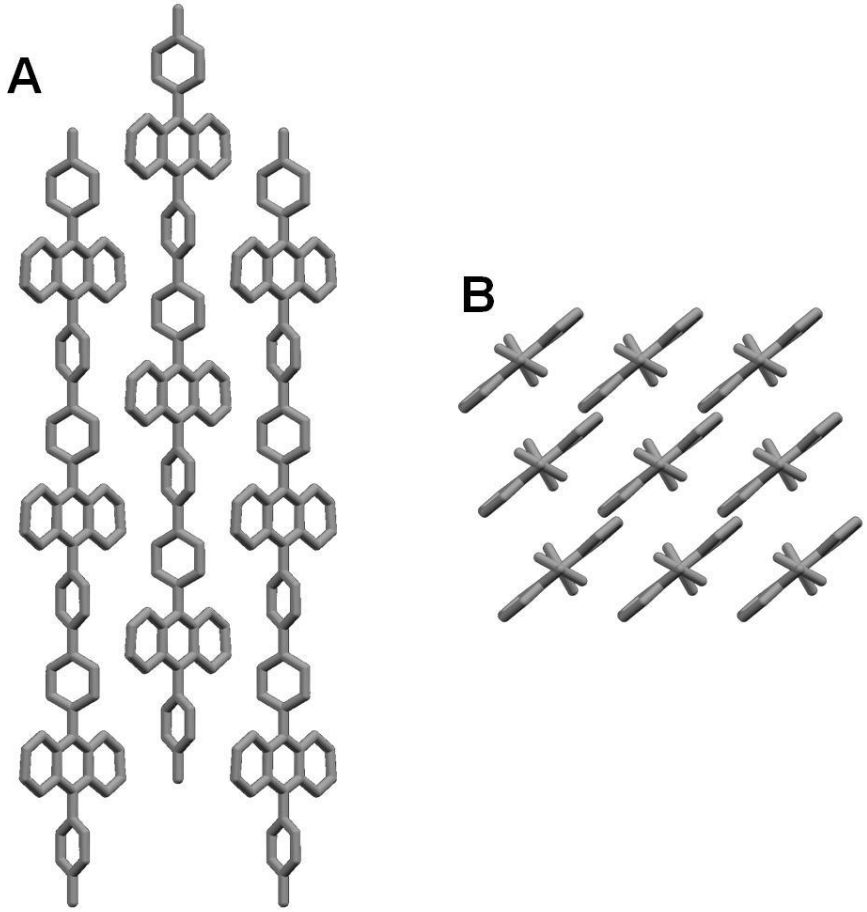

Figure 21. A) Refined structure of polyDPA viewed along c axis. B) Refined structure of polyDPA viewed along b axis. The anthracene moieties are not closely packed in the homopolymer structure and no excimers are generated confirming spectroscopic measurements.

6.1.8. References

[1] Ye, C., Zhou, L., Wang, L. and Liang, Z.; Phys. Chem. Chem. Phys., **2016**, *18*, 10818 – 10835.

[2] Zhou, J., Liu, Q., Feng, W., Sun, Y. and Li, F.; Chem. Rev., **2015**, *115*, 395 – 465.

[3] Monguzzi, A.,Tubino, R., Hoseinkhani, S., Campione, M. and Meinardi, F.; Phys. Chem. Chem. Phys., **2012**, *14*, 4322 - 4332.

[4] Pedrini, J. and Monguzzi, A.; J. Photon. Energy, 2017, 8(2), 022005.

[5] Goldschmidt, J. C. and Fisher, S.; Adv. Optical. Mater., **2015**, *3*, 510 – 535.

[6] Zhu, X., Su, Q., Feng, W. and Li, F.; Chem. Soc. Rev., **2017**, *46*, 1025 – 1039.

[7] Park, J., Xu, M., Li, F. and Zhou, H.-C.; J. Am. Chem. Soc., 2018, *140 (*16), 5493 – 5499.

[8] Monguzzi, A., Oertel, A., Braga, D., Riedinger, A., Kim, D. K., Knüsel, P. N., Bianchi, A., Mauri, M., Simonutti, R., Norris, D. J. and Meinardi, F.; ACS Appl. Mater. Interfaces, 2017, *9*, 40180 - 40186.

[9] Duan, P., Yanai, N. and Kimizuka, N.; J. Am. Chem. Soc., **2013**, *135 (51)*, 19056 – 19059.

[10] Hisamitsu, S., Yanai, N. and Kimizuka, N.; Angew. Chem. Int. Ed., **2015**, *54*, 11550 – 11554.

[11] Duan, P., Yanai, N., Nagatomi, H. and Kimizuka, N.; J. Am. Chem. Soc., **2015**, *137*, 887 – 1894.

[12] Ogawa, T., Yanai, N., Monguzzi, A. and Kimizuka, N.; Scientific Reports, **2015**, *5*, Article number: 10882.

[13] Vadrucci, R. Monguzzi, A., Saenz, F., Wilts, B. D., Simon, Y. C. and Weder, C.; Adv. Mater., **2017**, *29 (41)*, 1702992.

[14] Hosoyamada, M., Yanai, N., Ogawa, T. and Kimizuka, N.; Chem.Eur.J., **2016**, *22*, 2060 – 2067.

[15] Rowe, J. M., Zhu, J., Soderstrom, E. M., Xu, W., Yakovenko, A. and Morris, A. J.; Chem. Commun., **2018**, *54*, 7798 – 7801.

[16] Jiang, J.-X., Trewin, A., Adams, D. J. and Cooper, A. I.; Chem. Sci., **2011**, *2*, 1777 – 1781.

[17] Bonillo, B., Sprick, R. S. and Cooper, A. I.; Chem. Mater, **2016**, *28*, 3469 - 3480.

[18] Sachs, M., Sprick, R. S., Pearce, D., Hillman, S. A. J., Monti, A., Guilbert, A. A. Y., Brownbill, N. J., Dimitrov, S., Shi, X., Blanc, F., Zwijnenburg, M. A., Nelson, J., Durrant, J. R. and Cooper, A. I.; Nature Commun., **2018**, *9*, 4968.

[19] Xu, Y. and Jiang, D.; Chem. Commun., **2014**, *50*, 2781 – 2783.

[20]Gu, C., Huang, N., Chen, Y., Qin, L., Xu, H., Zhang, S., Li , Ma, Y. and Jiang, D.; Angew.Chem. Int. Ed., **2015**, *54*, 13594 – 13598.

[21] Patra, A. and Scherf, U.; Chem. Eur. J., **2012**, *18*, 10074 – 10080.

7. Radioluminescent MOFs and nanocomposites

7.1. Nanocrystalline MOFs and nanocomposites for luminescence and radioluminescence

7.1.1. Summary

Metal organic frameworks are composed of organic ligands and inorganic building blocks (metal cations or clusters based on metal ions). Their hybrid nature can be exploited to obtain a synergistic effect between the organic and the inorganic components. Highly efficient catalysts and photo-catalysts [1,2,3.4], sensitive and specific sensors [5,6,7] and advanced materials for imaging and bio-imaging [8,9] can be designed and developed thanks to the improved performances guaranteed by the nanometric distance between different building blocks inside the framework. Specifically, it has been shown that MOFs can be employed for scintillating applications and their performance are comparable or superior to benchmark reference materials [10,11].

In this section different samples of nanocrystalline fluorescent MOFs have been synthetized through a modulated approach (ZrDPAX; X=1,2,3,4) to control the size of the resulting crystals. The MOF itself is based on highly emissive ligands (4,4'-carboxylphenyl-(9,10)anthracen-dioic acid) connected by zirconium-based secondary building units ($Zr_6(\mu_3\text{-}O)_4(\mu_3\text{-}OH)_4(CO_2)_{12}$) [10]. Acetic acid inside the reaction mixture control the nucleation and growth processes of MOFs synthesis allowing to obtain nanosized crystals with sharp particle size distributions between 70 and 360 nm. All samples have been characterized in order to assess the high porosity and high chemical purity and the optical and radioluminescence properties have been tested. All samples display high fluorescence quantum yield (up to 70%) and display a bright emission under X-ray irradiation that matches the photoluminescence emission spectrum.

To develop self-standing bulk materials that can be employed efficiently as scintillator for ionizing radiation detection, MOFs nanocrystals have been embedded in two different commercial polymeric matrixes, PMMA and PDMS, respectively (ZrDPA@polymer). Two nanocomposites containing 0.5 $\%_{wt}$ of MOFs have been

tested under X-rays and γ-rays irradiation and display fast radioluminescence. This work opens the opportunity towards further development of MOF nanocomposites with higher nanocrystals loading and better optical properties for radiation detection, specifically towards γ-ray.

7.1.2. High energy radiation and particles detection

The detection and identification of high energy radiation is a relevant challenge in different branches of physics, from biochemical and medical devices to particle physics and astrophysics [12,13,14,15]. Moreover, it is widely employed in relation to the fields of nuclear power and national security. Different technologies allow the detection and identification of high energy radiation, mainly gas ionization, semiconductor detectors and scintillating detectors. In the following paragraph only the latter approach will be investigated.

A scintillator detector is usually generated by the coupling of an active material (scintillating material) with a photomultiplier tube (PMT) and a suitable electronics for data collection and analysis. The scintillating material is any material capable of converting part of the energy of an incoming high energy particle that interacts with the material in low energy photons usually in the U.V. or visible range. Then, the low energy radiation is collected by the PMT and the resulting electrical signal processed and stored. Since the scintillating material plays a key role in the detection processes, great efforts have been spent to develop engineered material with favourable properties: in the following it will be illustrated the requirements that a material must possess for scintillating applications.

- **High stopping power**. The incoming radiation or high energy particles (x and γ-ray, fast electrons (β particles), α particles or fast protons) that travel at or near the speed of light must release its energy through interactions with the solid material. γ-rays mainly interact with matter due to the photoelectric effect or Compton scattering. The interaction probability *via* the photoelectric effect scales as a power law of the atomic number of the elements inside the

materials with a coefficient of 4 to 5 depending on the energy of the incoming radiation. Instead, Compton scattering display a probability proportional to the atomic number of the elements in the material and is thus more effective for light elements. As it will be discussed later, scintillating materials often contain heavy elements to increase the radiation-matter interaction rate and the stopping power.

- **High light yield**. The light output for unit energy interacting on the scintillator is a fundamental parameter in scintillation technology since it determines the sensitivity of the detector. The light yield is defined in the following equation.

$$Light\ Yield = \frac{Number\ of\ scintillating\ photons}{Energy\ of\ incoming\ radiation\ (MeV)}$$

  Depending on the composition of the scintillating material light yield of $10^3/10^5$ photons for a 1 MeV γ-ray can be achieved.
- **Rise time.** The rapid detection of high energy radiation is another important feature of a scintillating material and it is a fundamental property in order to detect and separate different events.
- **Compatibility with the PMT and the electronic readout.**
- **Ease processability, scalability and low cost.**

Many different materials have been developed for scintillating applications and each one possesses advantages and drawbacks. Currently state of the art technologies are summarized below.

- **Inorganic scintillating materials.**
- **Organic scintillators.**
- **Polymeric or plastic scintillators.**

7.1.3. Radioluminescent metal-organic frameworks

In 2009 Allendorf et *al.* proposed the exploitation of Metal-Organic Frameworks as scintillating materials in high energy radiation detection technologies [16]. As reported in literature, MOFs offer clear advantages over traditional and other nanostructured materials:

- MOF structure tunability allows for the formation of controlled and defined structures at the atomic scale. The orientation and spatial disposition of ligands in space can be controlled in order to tune the electronic and hence the optical properties of cromophores inside the framework.
- Radiation resistance increases compared to standard organic materials.
- Photo- and radioluminescence quantum yields are already at the level of commercial scintillation materials.

7.1.4. Zirconium-based MOFs for radiation detection

7.1.4.1. Nanocrystalline ZrDPAX MOFs

Metal organic frameworks based on zirconium oxo-hydroxy clusters and the linker (4,4'-carboxylphenyl-(9,10)anthracen-dioic acid) (figure 2) have been reported first in 2014 by Lin research group [10] and interesting photo and radioluminescent properties have been measured. Thus, we decided to employ the same MOF to produce self-standing polymeric nanocomposites by embedding MOF nanocrystals in a suitable matrix. To develop composites with good optical properties the scattering due to the dispersed nanoparticles must be minimized in order to collect the light emission under the irradiation process. Thus, we developed a synthetic procedure to produce nanometer-sized crystal of MOF. The nucleation and growth process of zirconium-ions based metal organic frameworks can be controlled by systematic changing of experimental conditions. Modulation approach has been proved to be very effective to control the size, shape and crystallinity of the resulting MOF [17,18,19]. During the synthesis the modulator competes with linkers coordinating the oxy-hydroxo clusters slowing down the crystallization process and generating highly crystalline products. An acetic acid modulated synthesis has been developed: low

acetic acid concentration produces smaller crystals as evidenced by Debye-Scherrer analysis of the experimental PXRD data and proved by SEM images. Four different samples have been synthetized under the experimental conditions illustrated in the table below.

Table 1. Reagents and solvents employed in MOF synthesis.

ZrDPAX	**$ZrCl_4$ (mmol)**	**$DPA(COOH)_2$ (mmol)**	**Acetic acid (mmol)**	**DMF + H_2O**
ZrDPA1	0.5	0.5	25	50 mL + 50 µL
ZrDPA2	0.5	0.5	35	50 mL + 50 µL
ZrDPA3	0.5	0.5	45	50 mL + 50 µL
ZrDPA4	0.5	0.5	55	50 mL + 50 µL

Powder x-ray analysis displays sharp diffraction peaks even in the presence of low concentration of acetic acid and the decrease of the full width at height medium as the modulator concentration used during the synthesis is increased. Since all the attempt to growth a single crystal failed, the structure has been simulated and refined by Dr. C. X. Bezouidenhout using an isostructural material as reference. The position of the DPA units have been modeled over 3 positions of which one comprises an anthracene moiety that lies within a mirror plane. The remaining two disordered positions has the DPA moieties tilted 18.6°, clockwise and anticlockwise, respectively. A tetrahedral and an octahedral cavities in a 2:1 ratio are present inside the structure. The MOF exhibits a nearest-neighbour anthracene center-to-center distance of 11.7 Å.

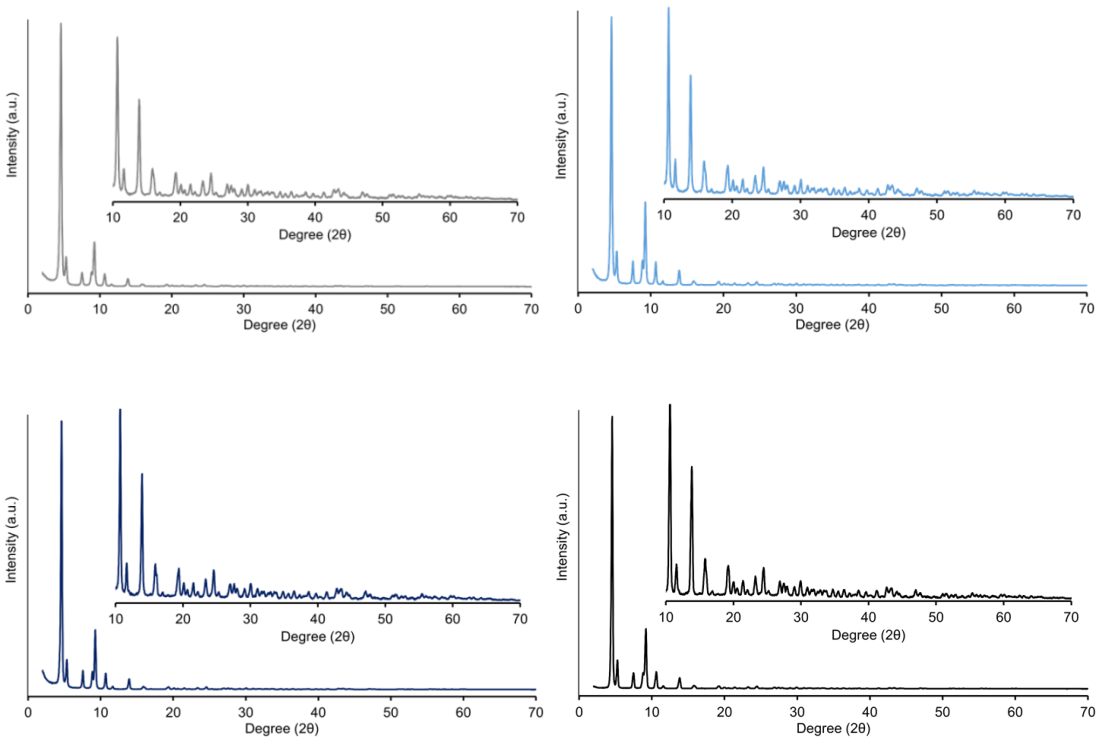

Figure 1. Powder x-ray diffraction patterns of ZrDPA1 (grey), ZrDPA2 (light blue), ZrDPA3 (blue) and ZrDPA4 (black). Insets: enlargement from 10 to 70 2θ degree.

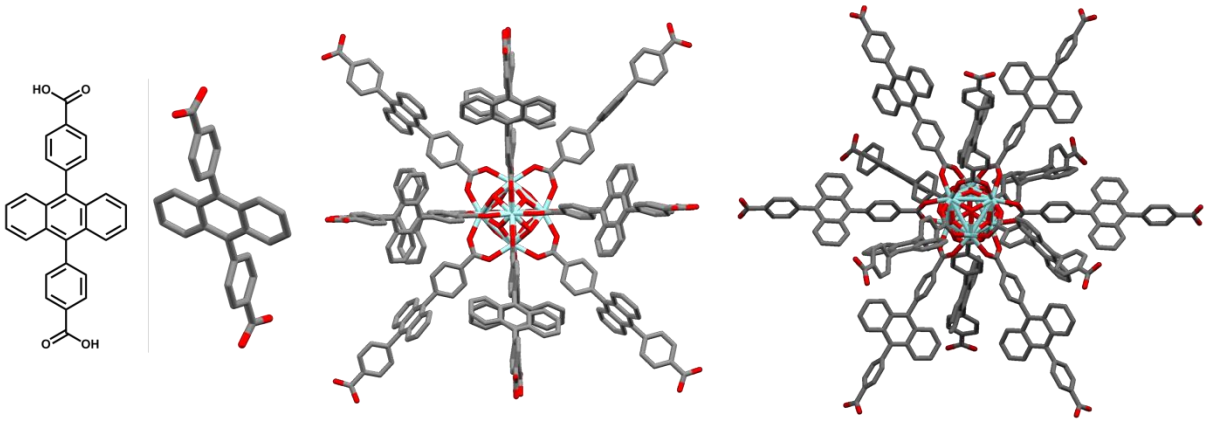

Figure 2. From left to right: 4,4'-carboxylphenyl-(9,10)anthracen-dioic acid molecule; zirconium oxo-hydroxo cluster and twelve connected ligands viewed along different orientations.

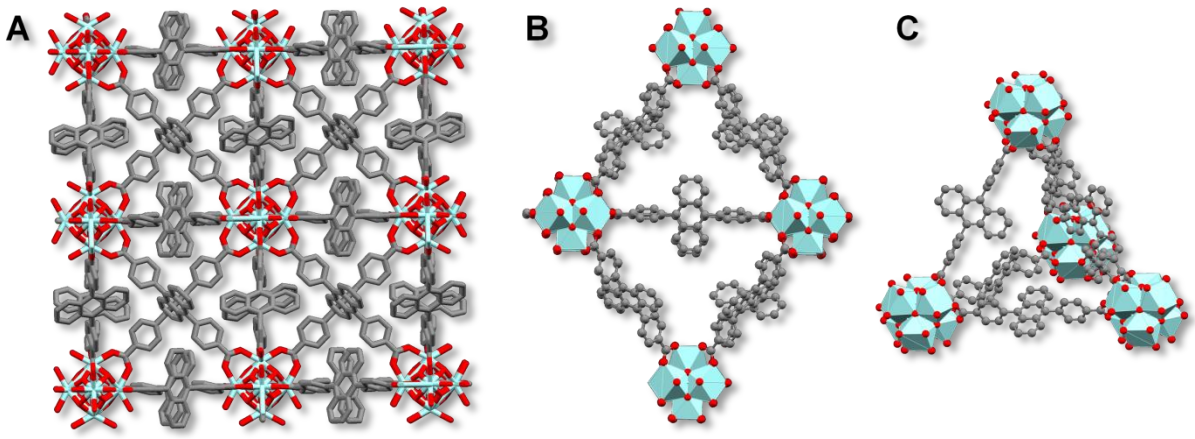

Figure 3. A) Refined crystal structure of ZrDPA MOF. The anthracene units have been fixed in one position for clarity. B) Octahedral cavity inside the structure of ZrDPA MOF. C) Tetrahedral cavity in the structure of ZrDPA MOF.

Scanning electron microscope images allow an in-depth investigation of MOF nanocrystals size and shape: to collect the image the powder has been casted from an isopropanol dispersion, dried and sputtered with a thin film (5 nm) of chromium. All samples are homogeneous and composed of single particles or small clusters of nanometer-sized crystals. Particles size distribution have been measured with the software ImageJ and a statistical distribution have been built on the basis of multiple images.

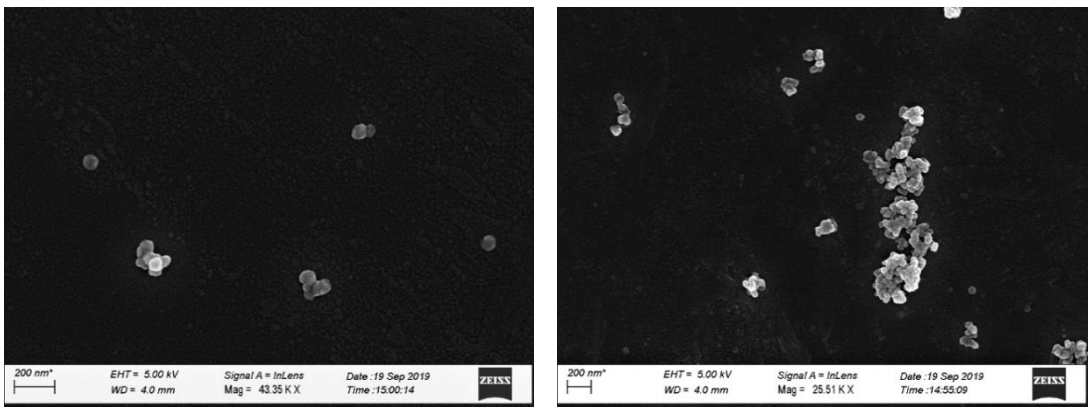

Figure 4. SEM images of ZrDPA1 at different magnifications.

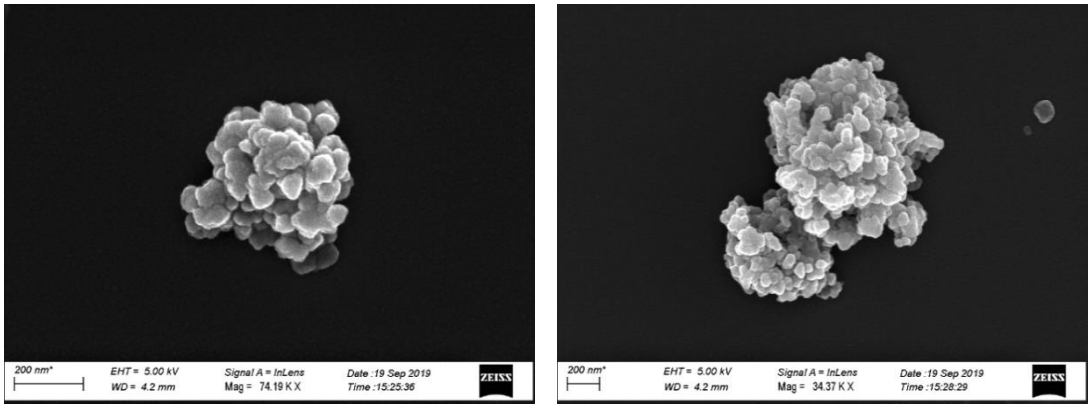

Figure 5. SEM images of ZrDPA2 at different magnifications.

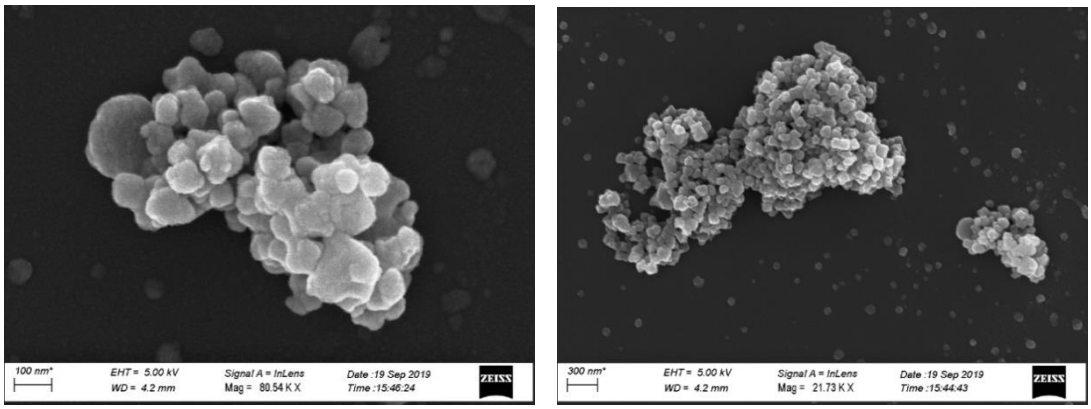

Figure 6. SEM images of ZrDPA3 at different magnifications.

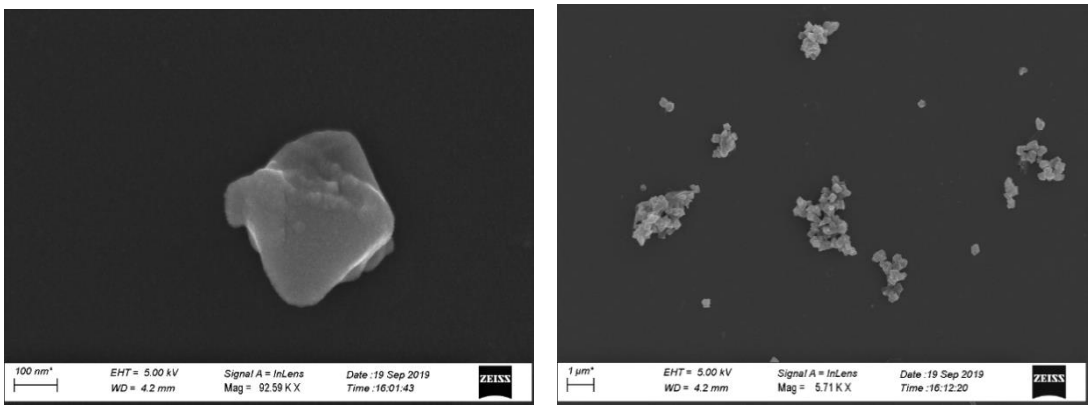

Figure 7. SEM images of ZrDPA4 at different magnifications.

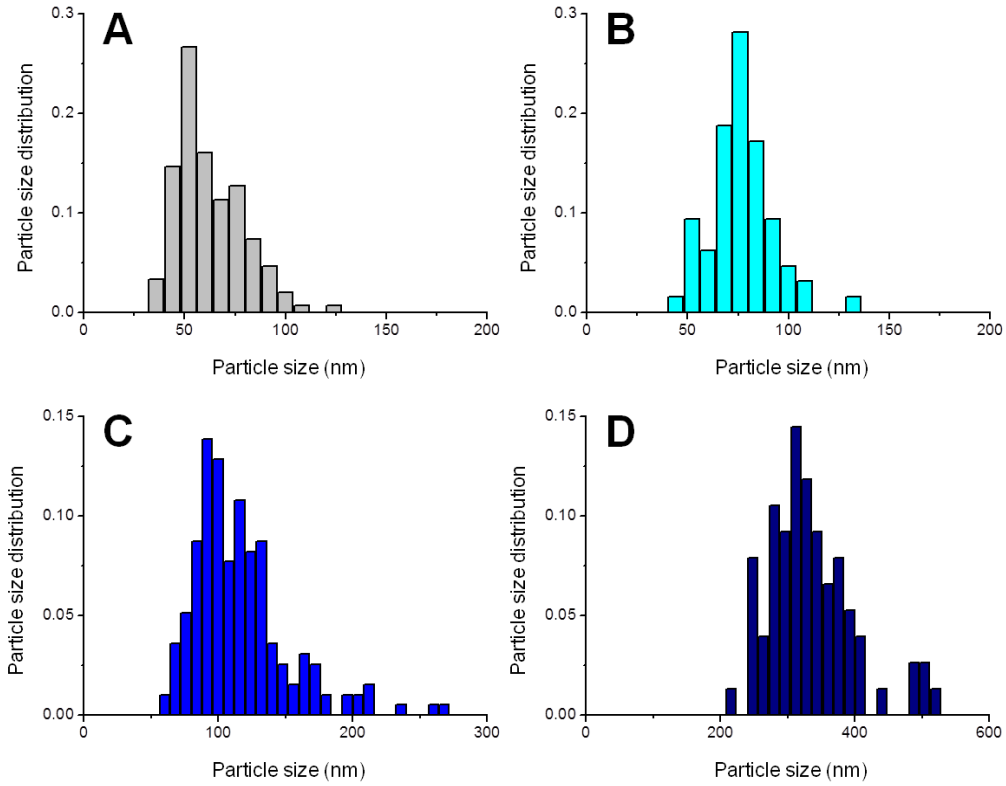

Figure 8. Particle size distribution calculated from SEM images of A) ZrDPA1 (grey) B) ZrDPA2 (light blue). C) ZrDPA3 (blue). D) ZrDPA4 (dark blue). SEM images are processed with ImageJ software and the resulting distributions are calculated on a minimum base of 100 particles.

Table 2. Particles size distributions calculated from SEM images.

Sample	Mean particle size (nm)	Standard deviation (nm)
ZrDPA1	60	20
ZrDPA2	85	20
ZrDPA3	130	40
ZrDPA4	350	60

Nitrogen adsorption isotherms measured at 77 K assessed the porosity of samples. Adsorption isotherms display two different slopes at pressures below 0.05 p/p° as suggesting the presence of different pores inside the structure according to the refined crystal structure. The increase in adsorption values at high loadings it's probably due to the formation of free space between clustered particles with dimensions around 10-100 nm. Carbon dioxide adsorption isotherms collected at 195 K display a small uptake at low pressure

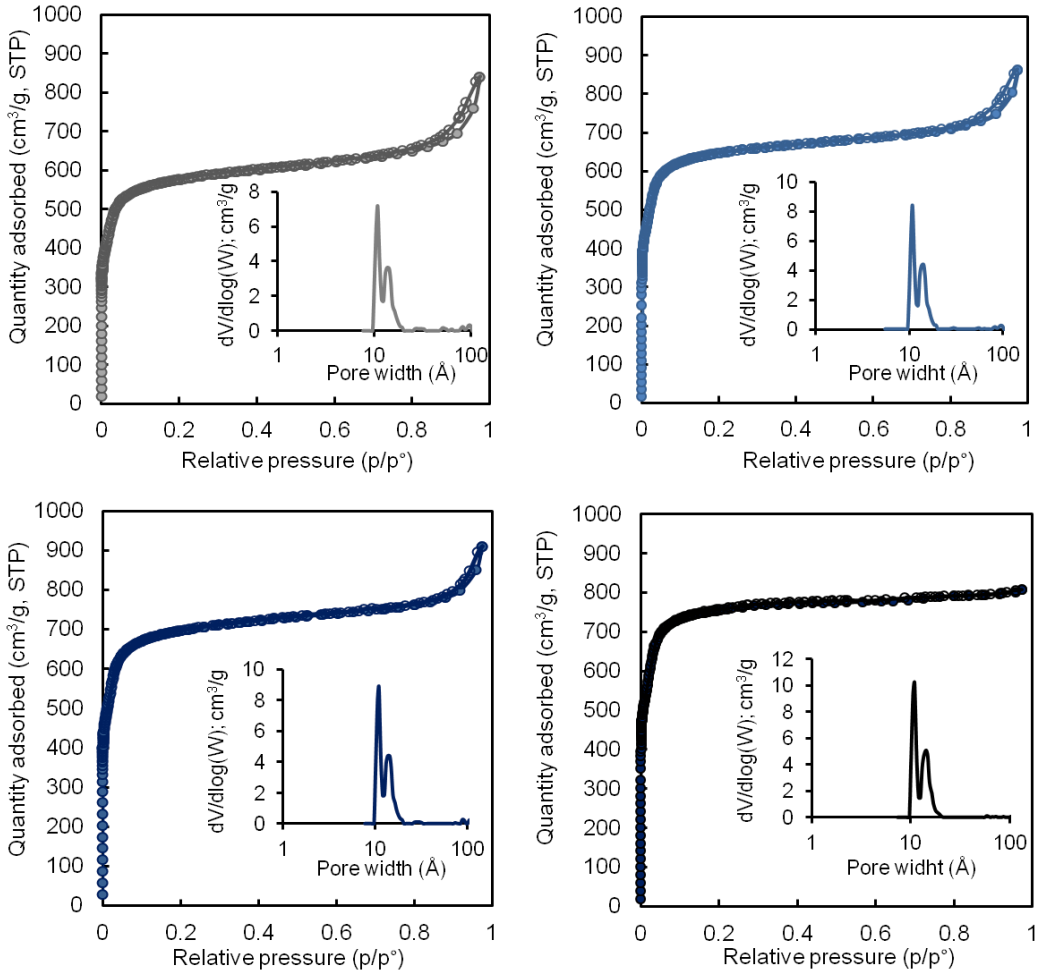

Figure 9. Nitrogen adsorption isotherms measured at 77 K of ZrDPA1 (grey), ZrDPA2 (light blue), ZrDPA3 (blue) and ZrDPA4 (dark blue). Insets: differential pore size distribution calculated according to NLDFT theory.

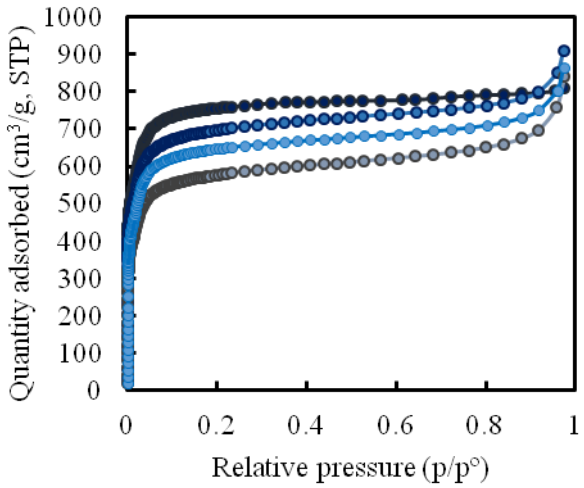

Figure 10. Nitrogen adsorption branches measured at 77 K of ZrDPA1 (grey), ZrDPA2 (light blue), ZrDPA3 (blue) and ZrDPA4 (dark blue). Insets: differential pore size distribution calculated according to NLDFT theory.

Table 3. Langmuir surface area, BET surface area and total pore volume calculated from nitrogen adsorption isotherms at 77 K.

Sample	**Langmuir surface area (m^2/g)**	**BET surface area (m^2/g)**	**Pore volume (cm^3/g)**
ZrDPA1	2560	2250	1.01
ZrDPA2	2900	2550	1.07
ZrDPA3	3100	2740	1.10
ZrDPA4	3410	3010	1.11

Helium-picnometry allowed the measurement of pore wall density and can be combined from the data of total pore volume calculated from nitrogen adsorption isotherms to compute the total density value: experimental data between 0.622 and 0.581 are in good agreement with the value calculated from the refined structure of 0.591 cm^3/g.

Table 4. Helium picnometry density, total pore volume and calculated total density for MOFs.

Sample	Helium picnometry density (cm^3/g)	Total density (cm^3/g)
ZrDPA1	1.676	0.622
ZrDPA2	1.617	0.592
ZrDPA3	1.607	0.581
ZrDPA4	1.634	0.581

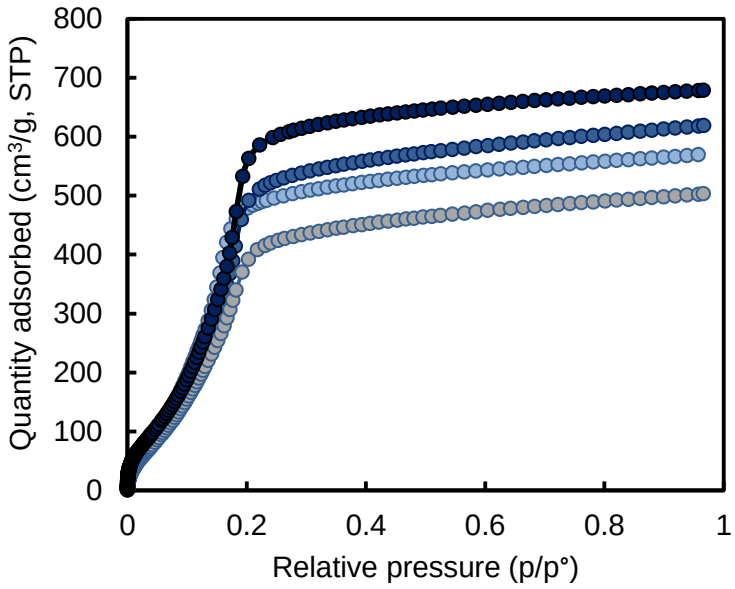

Figure 11. Adsorption branches of the carbon dioxide isotherms measured at 195 K of ZrDPA1 (grey), ZrDPA2 (light blue), ZrDPA3 (blue) and ZrDPA4 (dark blue).

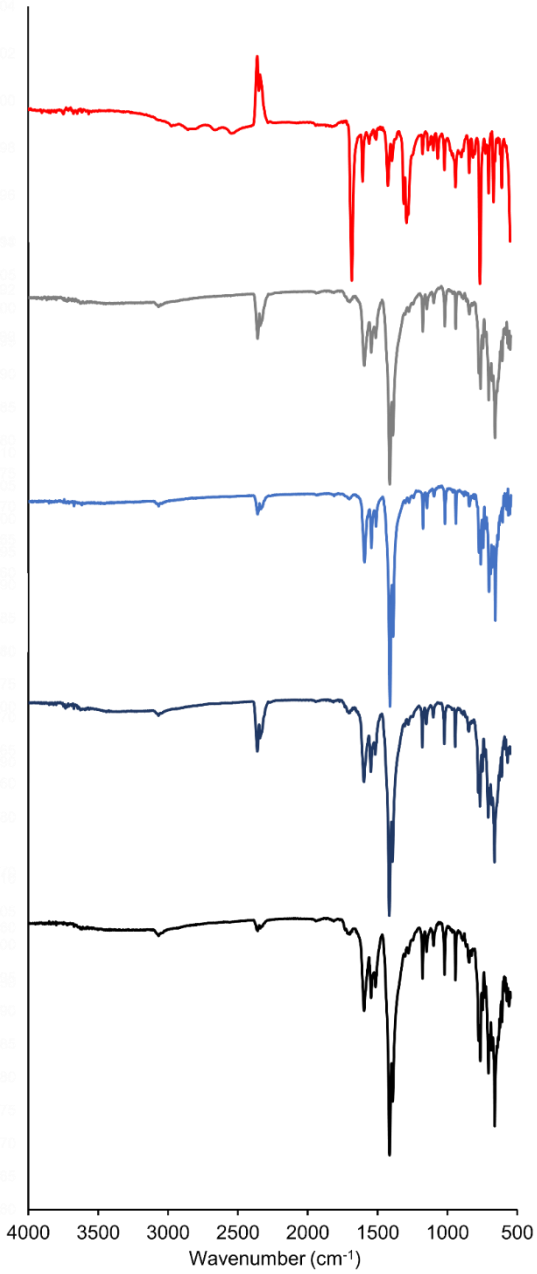

Figure 12. Infrared spectra of ligand (4,4'-carboxylphenyl-(9,10)anthracen-dioic acid; red, top), ZrDPA1 (grey), ZrDPA2 (light blue), ZrDPA3 (blue) and ZrDPA4 (black, bottom).

Infrared spectra adsorption bands analysis:

- 1690-1580 cm^{-1} region. The diacid ligand displays a strong C=O stretching band at 1683 cm^{-1}; ZrDPAX infrared spectra shows a shift to lower wavenumber due to coordination with the zirconium ions-based cluster (1596 cm^{-1}).

- All MOF samples display a broad signals between 770 cm^{-1} and 640 cm^{-1} due to the superposition of many bands due to the mixing of C-H and O-H bending modes with Zr-O modes. [20].

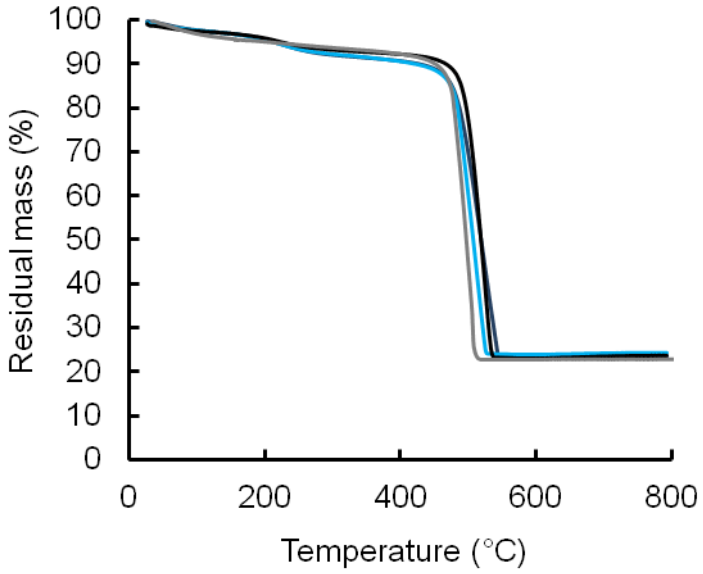

Liquid ^{1}H NMR analyses have been performed to investigate the chemical composition of the resulting MOF and quantify the concentration of defects. ZrDPAX have been digested with deuterated trifluoroacetic acid (TFA_d; 0.15 mL); then deuterated DMSO (DMSO_d_6; 0.8 mL) has been added to obtain a clear solution.

All ^{1}H liquid NMR spectra of digested ZrDPAX display signals that could be attributed to the ligand DPA$(COOH)_2$, acetic acid and formic acid. Peaks at 2.50 ppm and 15.4 ppm were due to residual signal of DMSO and TFA, respectively. Acetic acid is extensively incorporated in ZrDPAX structure: ZrDPA4 clearly displays a lower amount of acetic acid, while all the other sample contains similar amount. Formic acid is also incorporated in the frameworks in low amount (formic acid / DPA$(COOH)_2$ molar fraction of less than 0.02) due to its *in situ* generation from DMF decomposition. The molar ratios between acetic acid and the linker is calculated by integrating the spectra accounting for the multiplicity of hydrogens in each molecules and are reported in the table below.

Table 5. Molar ratio between residual acetic acid (modulator) and DPA after dissolution measured by ^{1}H liquid NMR spectroscopy.

ZrDPAX	$\frac{\boldsymbol{Acetic\ Acid}}{\boldsymbol{DPA(COOH)_2}}\boldsymbol{molar\ fraction}$
ZrDPA1	0.14
ZrDPA2	0.14
ZrDPA3	0.19
ZrDPA4	0.05

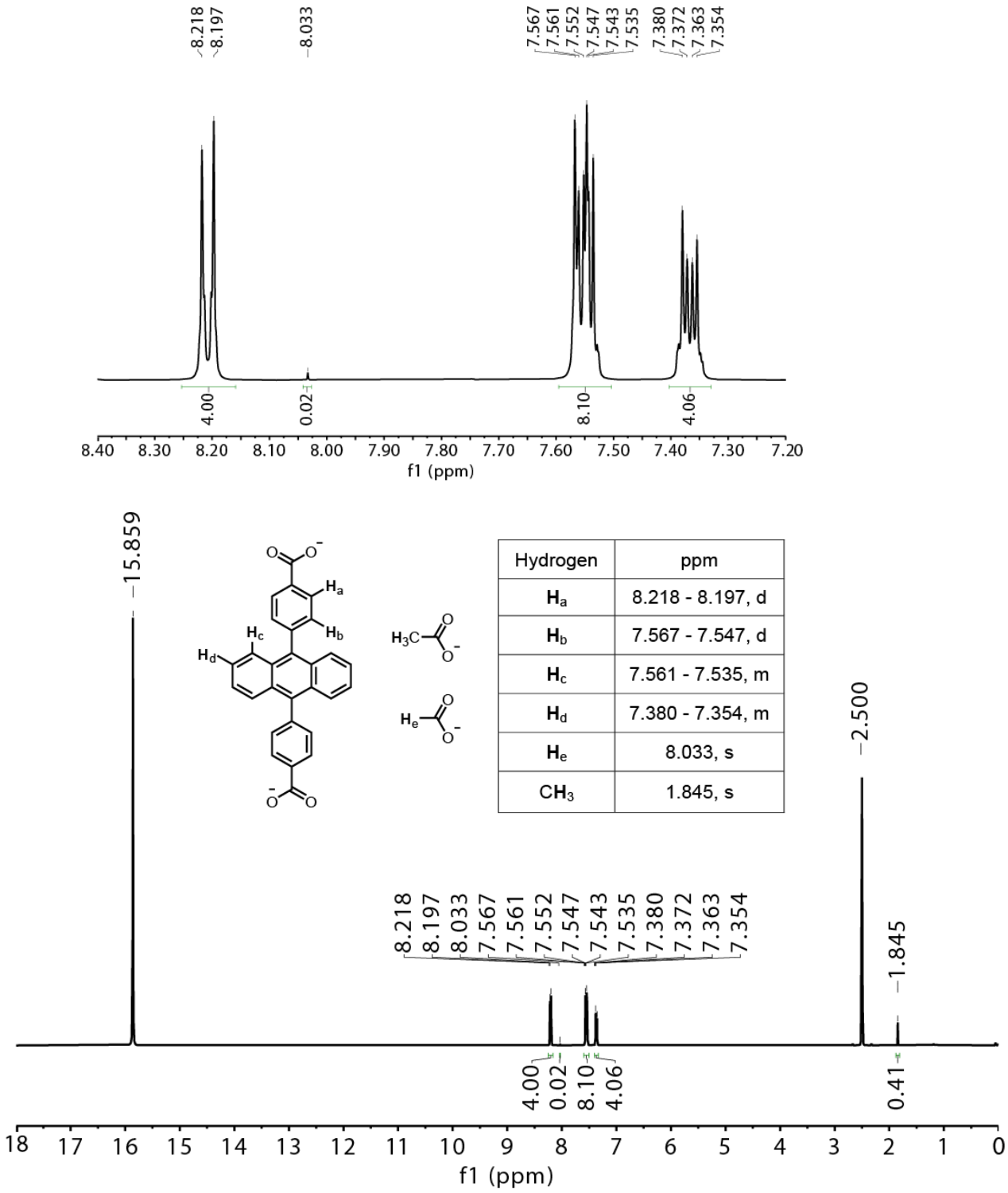

Figure 13. Top: zoom between 7.20 and 8.40 ppm of ^{1}H-NMR spectrum of ZrDPA1 after digestion with DMSO_d_6/TFA_d mixture. Bottom: ^{1}H-NMR spectrum of ZrDPA1 after digestion with DMSO_d_6/TFA_d mixture from 0 to 18 ppm.

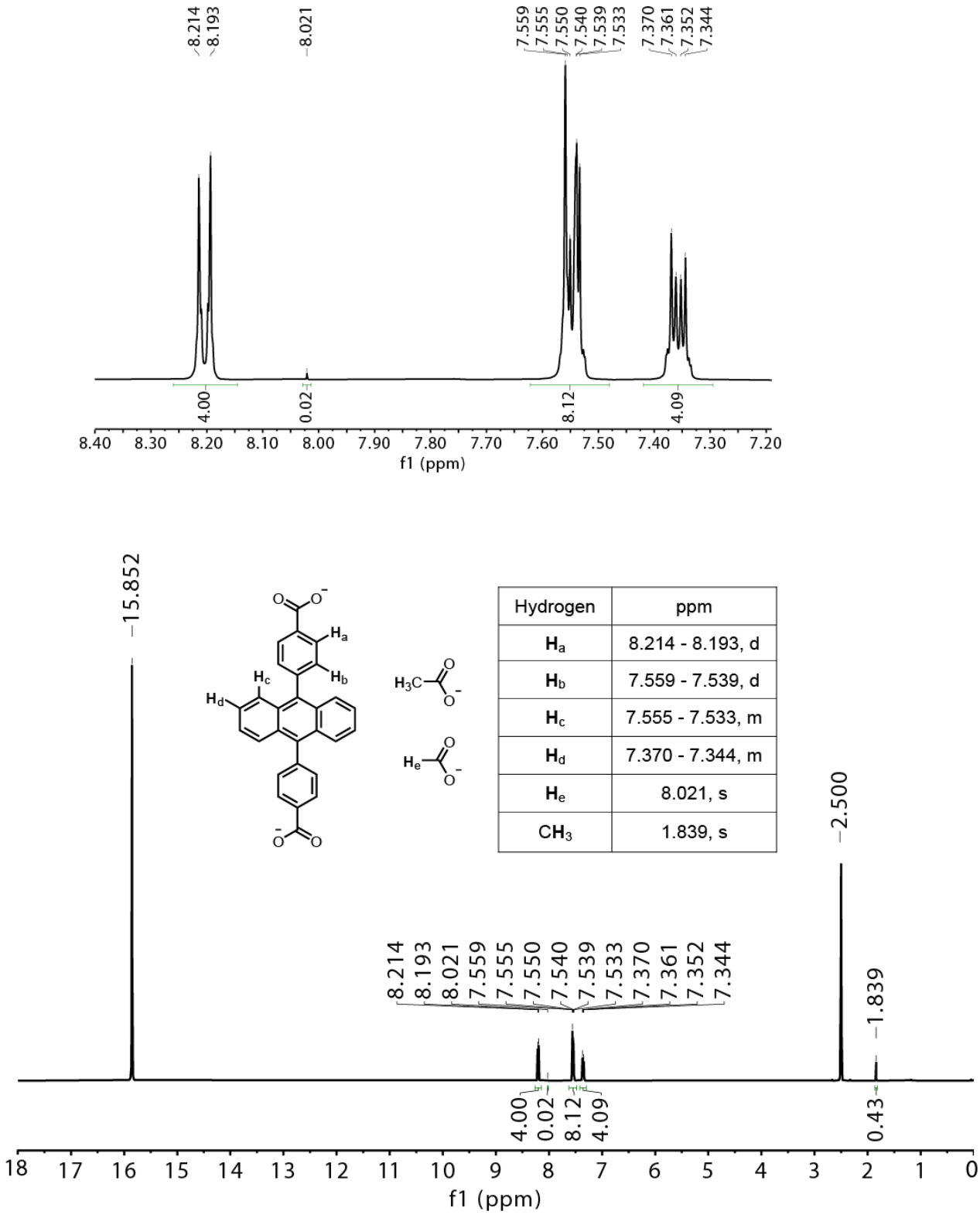

Figure 14. Top: zoom between 7.20 and 8.40 ppm of ^{1}H-NMR spectrum of ZrDPA2 after digestion with DMSO_d_6/TFA_d mixture. Bottom: ^{1}H-NMR spectrum of ZrDPA2 after digestion with DMSO_d_6/TFA_d mixture from 0 to 18 ppm.

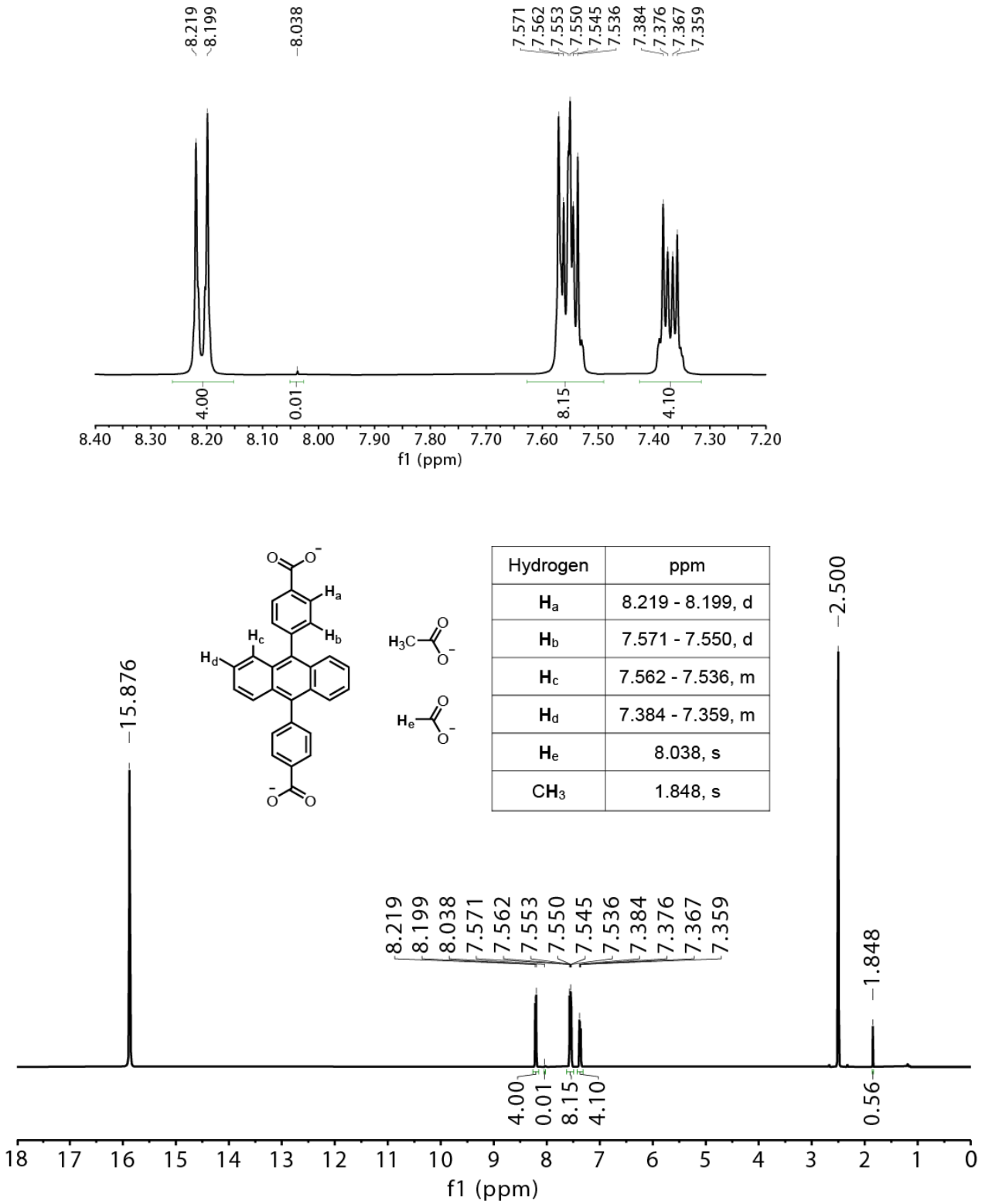

Figure 15. Top: zoom between 7.20 and 8.40 ppm of ^{1}H-NMR spectrum of ZrDPA3 after digestion with DMSO_d_6/TFA_d mixture. Bottom: ^{1}H-NMR spectrum of ZrDPA3 after digestion with DMSO_d_6/TFA_d mixture from 0 to 18 ppm.

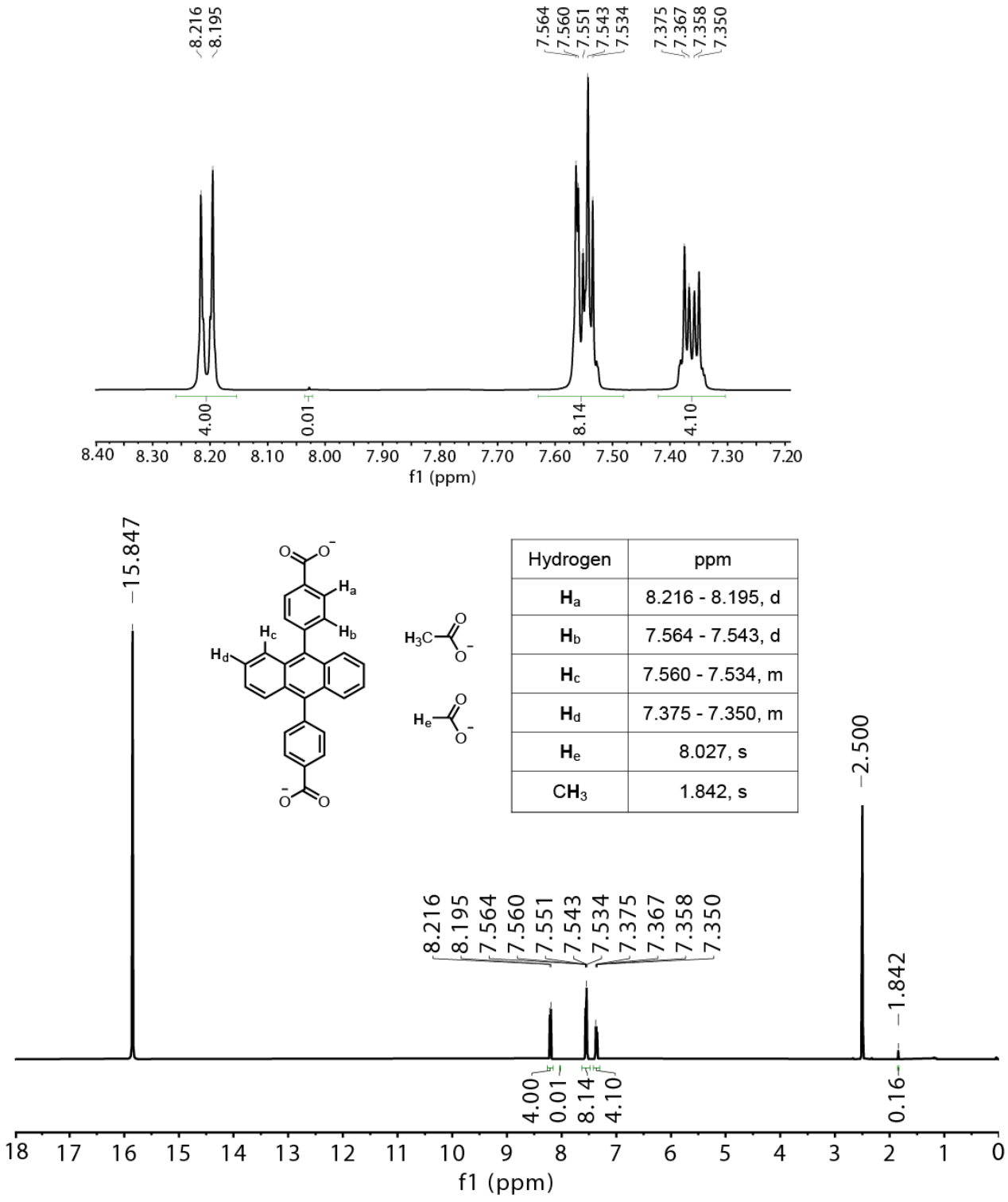

Figure 16. Top: zoom between 7.20 and 8.40 ppm of ^{1}H-NMR spectrum of ZrDPA4 after digestion with DMSO_d_6/TFA_d mixture. Bottom: ^{1}H-NMR spectrum of ZrDPA4 after digestion with DMSO_d_6/TFA_d mixture from 0 to 18 ppm.

Table 6. Molar ratio between residual acetic acid (modulator) and DPA after dissolution measured by ^{1}H liquid NMR spectroscopy.

ZrDPAX	$\frac{Acetic\ Acid}{DPA(COOH)_2}$ **molar fraction**
ZrDPA1	0.14
ZrDPA2	0.14
ZrDPA3	0.19
ZrDPA4	0.05

The optical and photophysical properties of ZrDPA samples have been tested in dispersion. All samples display an absorption spectrum similar to the free diphenylanthracene molecule in solution with a well-defined vibronic structure. The photoluminescence spectrum is slightly red-shifted and shows a maximum at 440 nm. Different techniques have been employed to determine the photoluminescence quantum yield: all MOF display a good quantum yield that increase with the particle size from 45 to 64 %. This effect can be related to the presence of defective sites and optical traps at surfaces: since excitations inside MOF crystals can diffuse for characteristic lengths, they have higher probability of reaching surfaces and thus be quenched in smaller crystals.

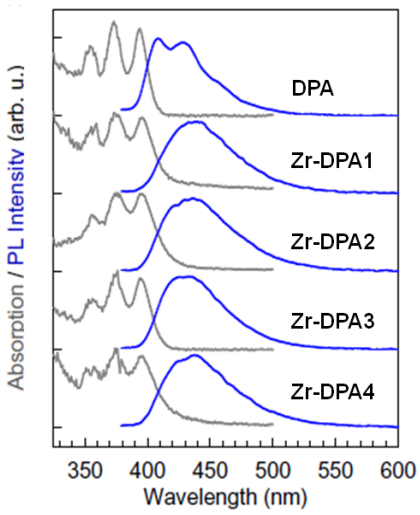

Sample	Quantum Yield (%)
Zr-DPA1	45
Zr-DPA2	56
Zr-DPA3	59
Zr-DPA4	64

Figure 17. Optical absorption and emission spectra of diphenylanthracene (DPA) and MOF nanocrystals dispersion. Mean photoluminescence quantum yields for each samples calculated from different independent measurements have been reported in the table on the left.

All powder samples reveal radioluminescnece under x-ray excitation and display a quantum yield of the same order of magnitude of a reference inorganic material employed in scintillation technology, Bismuth germinate ($Bi_4Ge_3O_{12}$, BGO).

7.1.4.2. MOF embedded scintillating nanocomposites

The development of a novel scintillating material requires the generation of a self-standing bulk object that can be fitted and coupled with a photomultiplier tube and a proper optical system. Thus we decide to embed MOF nanocrystals inside polymeric matrixes. Small size MOF nanocrystals (ZrDPA1) have been employed for the synthesis of bulk scintillators to reduce scattering effects related to the nanoparticles dispersion and to avoid aggregation and sedimentation problems related to the handling of bigger particles. Two polymer matrixes have been tested to generate nanocomposites that can be readily applied for radioluminescent sensing. Polymethyl methacrylate (PMMA) and polydimethylsiloxane (PDMS) have been chosen to investigate the different behaviour of MOF nanocrystals embedded in matrixes with different polarity, chemical environment and mechanical properties. PMMA has been prepared by thermal initiated radical polymerization reaction of freshly distilled methyl methacrylate with 2-2'-azobisisobutirronitrile (AIBN) to obtain a polymer of molecular weight around 50000 Da and the nanocomposites have been obtained by hot-pressing in a stainless steel mold a dispersion of MOF nanocrystals inside the polymer matrix. A commercial product has been used for the preparation of MOF nanocomposites with PDMS (RTV615; Elantas). After the dispersion of MOF nanocrystals inside the pre-polymer, a second component has been added and the well-mixed dispersion have been cured at low temperature overnight to induce the cross-linking reaction (see Experimental Details for further details).

A blank sample and two different nanocomposites have been prepared with each polymer. The composition of the samples are reported below. Since the transparency degraded with increasing the MOF percentage the nanocomposites have been prepared with only $0.05\%_{wt}$ and $0.5\%_{wt}$ of dispersed MOF.

Sample	MOF $\%_{wt}$
Blank, PMMA	-
$C_{LOW,PMMA}$	0.05
$C_{HIGH,PMMA}$	0.5
Blank, PDMS	-
$C_{LOW,PDMS}$	0.05
$C_{HIGH,PDMS}$	0.5

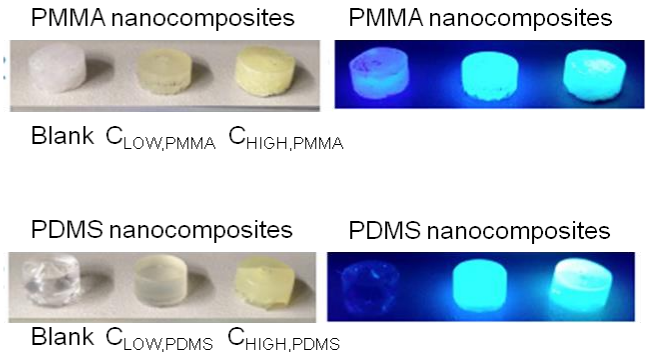

Figure 18. Left: table of blank samples and nanocomposites prepared for radioluminescence experiments. Right: digital pictures of nanocomposites under daylight and U.V. light.

Nanocomposites have been characterized with infrared and solid state NMR spectroscopy, DSC analysis and TEM.

Infrared spectroscopy and DSC analysis display that the chemical nature and the thermal properties of the polymeric matrixes are not altered by embedding MOFs probably due to the low concentrations employed. Transmission electron microscopy images obtained on thin sections of the polymethyl methacrylate nanocomposites reveal the formation of aggregates with diameter around 1 μm. This observation agrees with the measurements of optical properties that display a red-shifted spectrum, more similar to the spectrum of solid MOF powder than MOF dispersion.

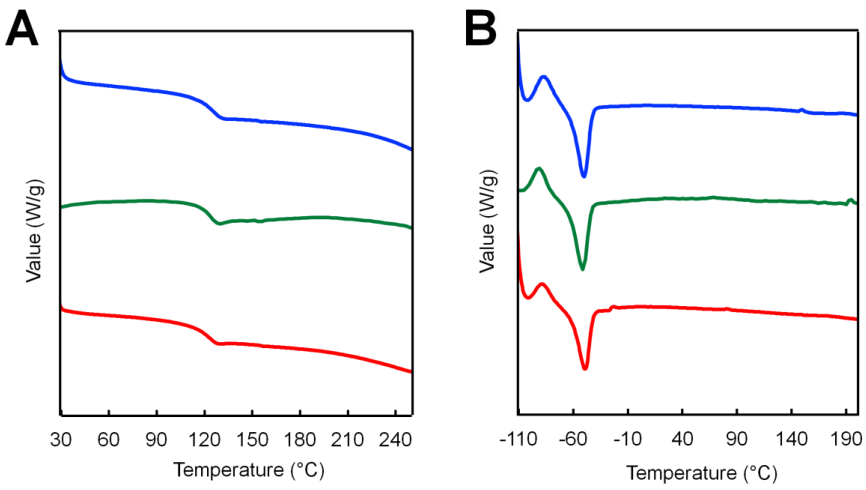

Figure 19. A) DSC traces of blank PMMA sample (blue line),MOFs nanocomposite (low concentration, 0.05$\%_{wt}$ green line) and high concentration (0.5 %, blue line). B) DSC traces of

blank PDMS sample (blue line) and MOFs nanocomposite (0.05%$_{wt}$ green line and 0.5% red line).

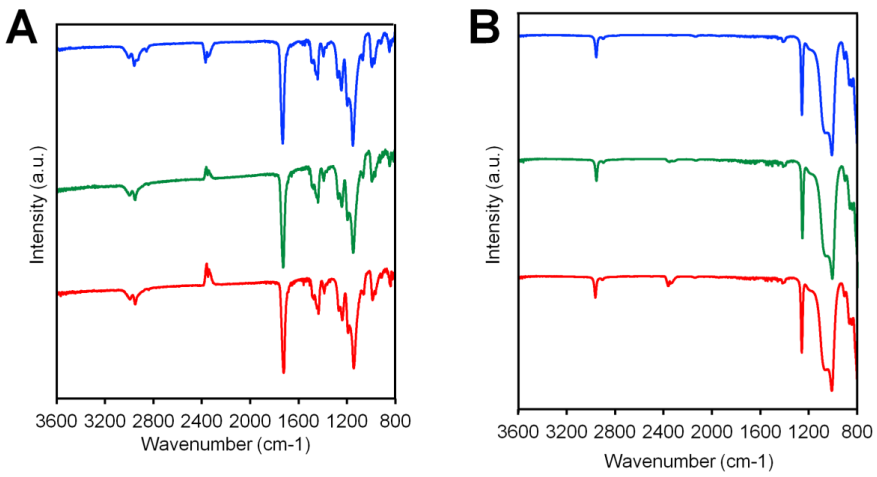

Figure 20. Left: infrared spectra of blank PMMA sample (blue line) and MOFs nanocomposites: low concentration (0.05%$_{wt}$, green line) and high concentration (0.5%$_{wt}$, red line). Right: Infrared spectra of blank PDMS sample (blue line) and MOFs nanocomposites: low concentration (0.05%$_{wt}$, green line) and high concentration (0.5%$_{wt}$, red line).

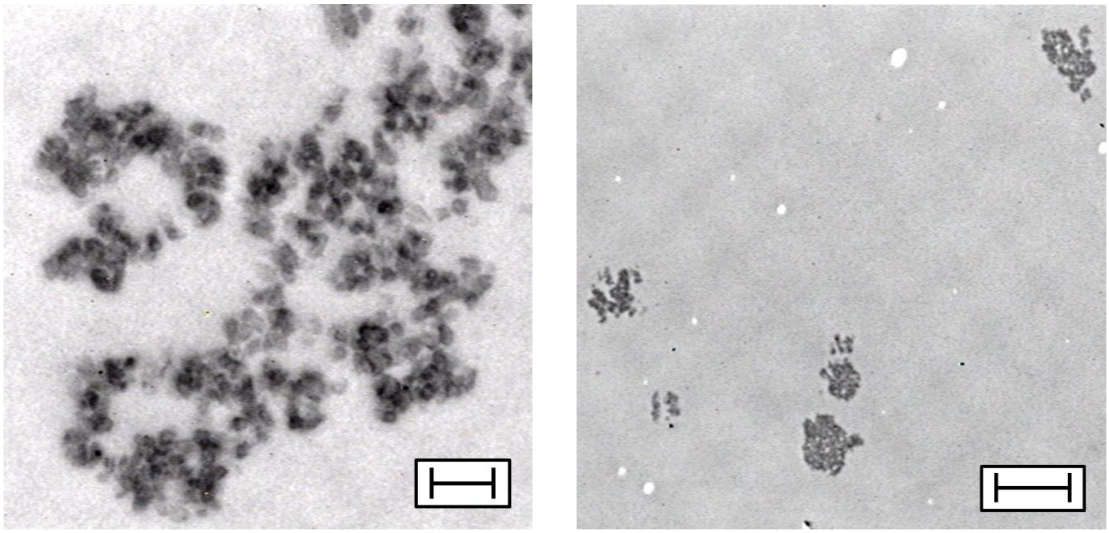

Figure 21. TEM images of MOF nanocrystals embedded inside PMMA matrix. The sample has been prepared by cutting a slice of 80 nm height with a ultramicrotome and then positioned on a copper grid. The material has been sputtered with a 5 nm layer of chromium before measurements.

The effect of the embedding of MOF nanocrystals in a polymer matrix on their photoluminescence properties is depicted below. Under 405 nm excitation, the C_{LOW} samples show a bright blue photoluminescence peaked at 450 nm and 464 nm for PMMA and PDMS composite, respectively, slightly red shifted with respect the diluted nanocrystals dispersion case due to partial re-absorption of the emitted light. On the other hand, in both polymers the C_{HIGH} samples display a greenish photoluminescence peaked at 485 nm. Considering that the photoluminescence spectra shapes are similar to that one of the bare MOF powder, we ascribe these effects to the presence of nanocrystals aggregates. The presence of aggregates is further advised also by the multi-exponential character of the emission intensity decay with time (not shown), which indicates that at the employed concentration the proper dispersion of MOFs in the matrix is more difficult partially thus avoiding the effective surface passivation on individual nanocrystals observed in the C_{low} case.

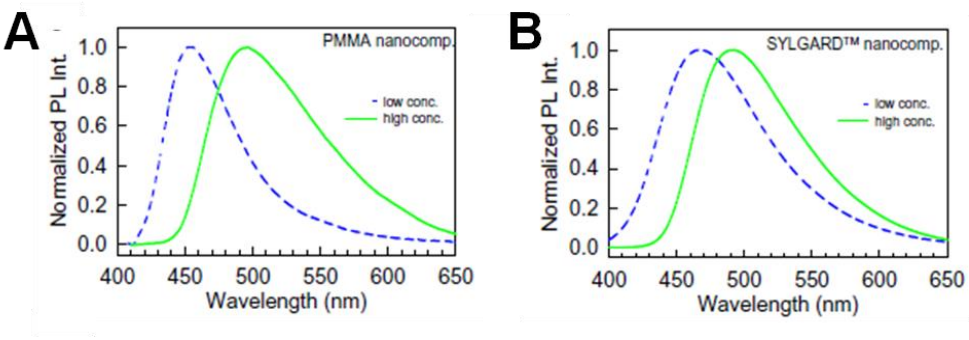

Figure 22. Photoluminescence spectra of MOF nanocomposites. A) PMMA nanocomposites ($C_{LOW,PMMA}$, dashed blue line; $C_{HIGH,PMMA}$, green line). B) PDMS nanocomposites ($C_{LOW,PDMS}$, dashed blue line; $C_{HIGH,PDMS}$, green line).

Finally, the radioluminescence properties of the nanocomposites have been tested under continous irradiation. The radioluminescence spectra of the C_{HIGH} nanocomposites show a bright greenish radioluminescence with a shape matching the photoluminescence profile, a hint that emitted photons are produced by radiative recombination of singlet excitons on the MOF ligands.

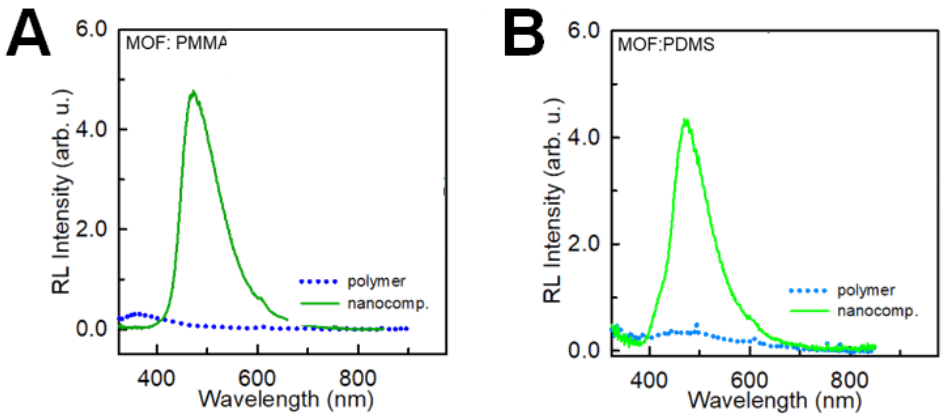

Figure 23. Radioluminescence spectra of polymers and MOF nanocomposites. A) PMMA (dashed blue line) and nanocomposite $C_{HIGH,PMMA}$ (green line). B) PDMS (dashed blue line) and $C_{HIGH,PDMS}$ (green line).

7.1.5. Conclusion

Metal organic frameworks based on zirconium ions oxo-hydroxy clusters and highly fluorescent ligand 4,4'-carboxylphenyl-(9,10)anthracen-dioic acid (DPA) have been engineered to generate 5 samples of nanometer-sized crystals with sharp particle size distributions peaked between 70 and 360 nm as determined from SEM images (Zr-DPAX) through a modulated approach. The samples have been extensively characterized with N_2 and CO_2 adsorption isotherms, infrared and solid-state NMR spectroscopy and thermogravimetric analyses. Optical spectroscopic techniques revealed high photoluminescence quantum yield that increased along with crystal sizes dimensions up to 64% due to decrease in number of surface-related defects and radioluminescence properties under x-ray irradiation. In order to obtain a scintillating solid-state device, nanocrystals of MOFs have been embedded in two different polymeric matrixes, polymethyl methacrylate and polydimethyl siloxane. These nanocomposites display photoluminescence quantum yield up to 70% and display a high radioluminescence quantum yield and a fast response in the nanosecond domain under irradiation with soft x-rays. Moreover, they were suitable for the fast detection of γ–rays.

7.1.6. Experimental details

Scheme 1. Synthetic scheme for ligand 4,4'-carboxylphenyl-(9,10)anthracen-dioic acid.

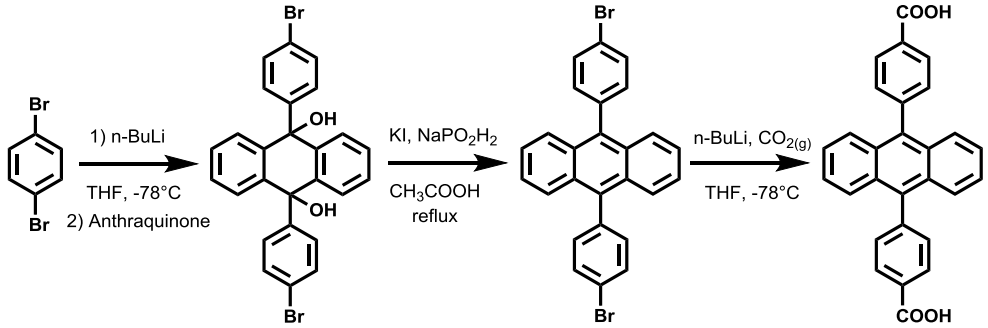

Synthesis of 9,10-bis(4-bromophenyl)-9,10-dihydroanthracene-9,10-diol

n-BuLi (4.8 mL; 2.5 M in hexane) was added dropwise to a solution of 1,4-dibromobenzene (2.83 g; 12.00 mmol) in THF (100 mL) at -78 °C under nitrogen atmosphere. The resulting solution was stirred for 30 minutes at the same temperature and then a dispersion of anthraquinone (1.19 g; 5.70 mmol) in 150 mL of THF was added *via* cannula. The resulting dispersion was left at -78 °C for 2 hours and allowed to warm to room temperature overnight. The solvent was removed by rotatory evaporation and the solid was recovered with diethylether and washed with water. The organic fractions were collected and the solvent was removed under vacuum to yield an off-white powder. The product was recrystallized from hot toluene to give clear crystals (2.11g). Yield: 34%. ^{1}H NMR (DMSO_d_6): δ (ppm) = 7.74 (4H, d), 7.41 (4H, m), 7.08 (4H, d), 6.65 (4H, m), 6.38 (2H, s).

Synthesis of 9,10-bis-(4-bromophenyl)anthracene

The diol (2.1 g; 4 mmol) was added to a round bottom flask containing KI (4.1g; 24.7 mmol), $NaPO_2H_2 \cdot H_2O$ (4.6 g; 52.3 mmol) and 40 mL of acetic acid and the mixture was heated to reflux for 2 hours. The precipitation of a yellow powder was observed. The dispersion was cooled down to room temperature and the solid was collected by filtration and washed with acetic acid (20 mL) and water (50 mL) and dried in air overnight. The product was recrystallized from dichloromethane to obtain slightly

greenish crystals (1.67 g). Yield: 85%. ^{1}H NMR ($CDCl_3$): δ (ppm) = 7.75 (4H, d), 7.66 (4H, m), 7.35 (8H, m).

Synthesis of 4,4'-carboxylphenyl-(9,10)anthracen-dioic acid

9,10-bis(4-bromophenyl) anthracene (0.7 g; 1.43 mmol) dissolved in 70 mL dry THF and the solution was cooled to -78 °C. *n*-BuLi (1 mL ; 2.5 M in hexane) was added dropwise under inert atmosphere and the solution is further stirred for 45 minutes at -78 °C. Gaseous carbon dioxide was bubbled in the resulting solution while the mixture was slowly allowed to warm to room temperature. After 3 hours the bubbling was stopped, THF (40 mL) and 1M HCl aqueous solution (20 mL) added to precipitate the solid as an off-white powder (pH ~ 1). The powder was filtered and washed with water. The product is further crystallized from THF/hexane to give off-white crystals (0.5 g). Yield: 84%. ^{1}H NMR (DMSO_d_6): δ (ppm) = 13.15 (2H, s), 8.23 (4H, d), 7.61 (4H, d), 7.55 (4H, m), 7.45 (4H, m).

General procedure for MOF synthesis (ZrDPAX)

$ZrCl_4$ (116.5 mg; 0.50 mmol) and 4,4'-carboxylphenyl-(9,10)anthracen-dioic acid (209 mg; 0.50 mmol) were dispersed in a mixture of dry DMF (50 mL) and deionized water (50 µL) in a 100 mL glass vial and a proper amounts of acetic acid was added (see Table S1). The mixture was sonicated for 1 minutes at room temperature and then heated at 120 °C for 22 hours. The vial was cooled down to room temperature and the slightly yellowish solid was separated by centrifugation, washed with DMF (5 times) and THF (5 times) and dried. The sample was activated at 140 °C overnight under high vacuum.

Table 7. Reagents and solvents employed in MOF synthesis.

ZrDPAX	**$ZrCl_4$ (mmol)**	**$DPA(COOH)_2$ (mmol)**	**Acetic acid (mmol)**	**DMF + H_2O**
ZrDPA1	0.5	0.5	25	50 mL + 50 µL
ZrDPA2	0.5	0.5	35	50 mL + 50 µL
ZrDPA3	0.5	0.5	45	50 mL + 50 µL

ZrDPA4	0.5	0.5	55	50 mL + 50 µL

General procedure for PMMA nanocomposite preparation

PMMA (5.0 g) was dissolved in dichloromethane (70 ml) and ZrDPA1 (20 mg) was dispersed in the resulting solution. The homogeneous dispersion was poured in a proper stainless steel mold and degassed at 60°C under vacuum to remove the solvent. After 6 hours the material was heated up to 200°C, pressed at high pressure of 10000 psi for 30 s, then annealed for 2 hours at 200°C. The sample was cooled down to room temperature and removed from the mold to obtain well defined cylindrical nanocomposites.

General procedure for PDMS nanocomposite preparation

PDMS prepolymer RTV 615 base (2.0 g) was poured to a 25 mL centrifuge tube (polypropylene, PP) and a 0.2 mL of a dispersion of ZrDPA1 (10 mg) in THF was added. The mixture was homogenized under stirring and successively RTV 615 curing agent (0.2 g) was added. After a careful mixing, the homogenous mixture was degassed under vacuum for 2 hours and poured onto a proper PP mold. A second degassing was performed, and the sample was heated under a vacuum oven at 60 °C for 16 hours. The specimen was slowly cooled to room temperature and removed from the mold.

Rietveld refinement and crystallographic data of ZrBCP

Powder x-ray diffraction patterns have been refined by Dr. C. X. Bezuidenhout using the TOPAS-Academic-64 V6 software package.

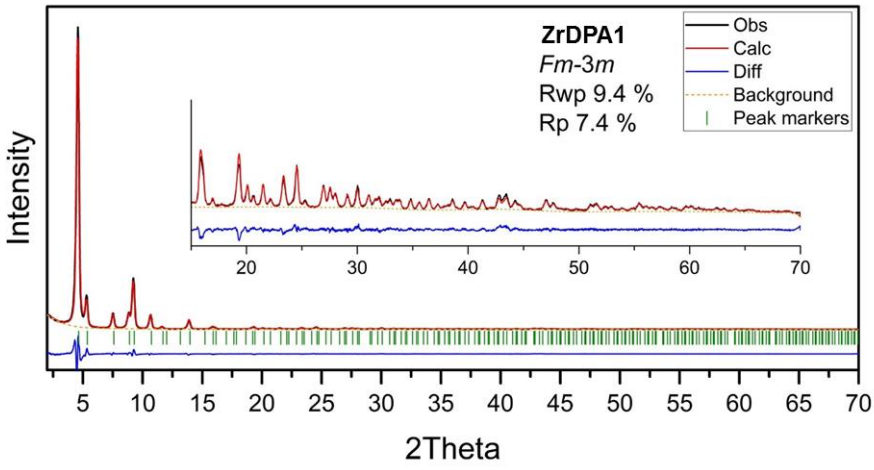

Figure 24. Rietveld fits of X-ray data for ZrDPA1.

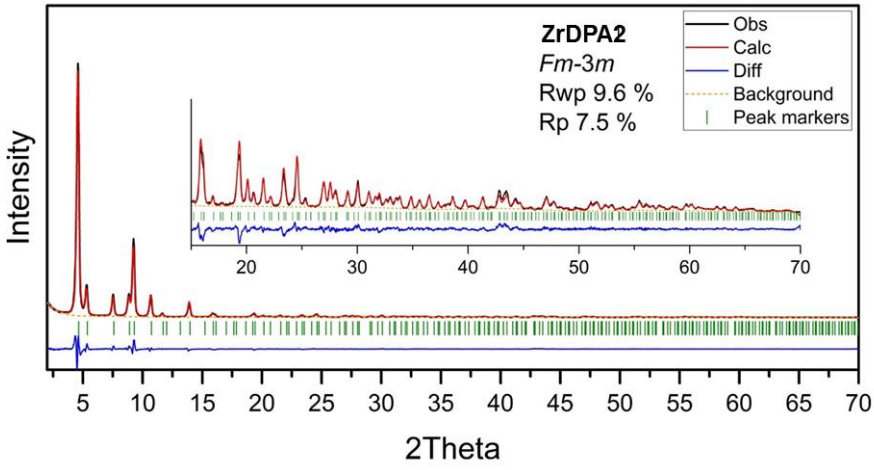

Figure 25. Rietveld fits of X-ray data for ZrDPA2.

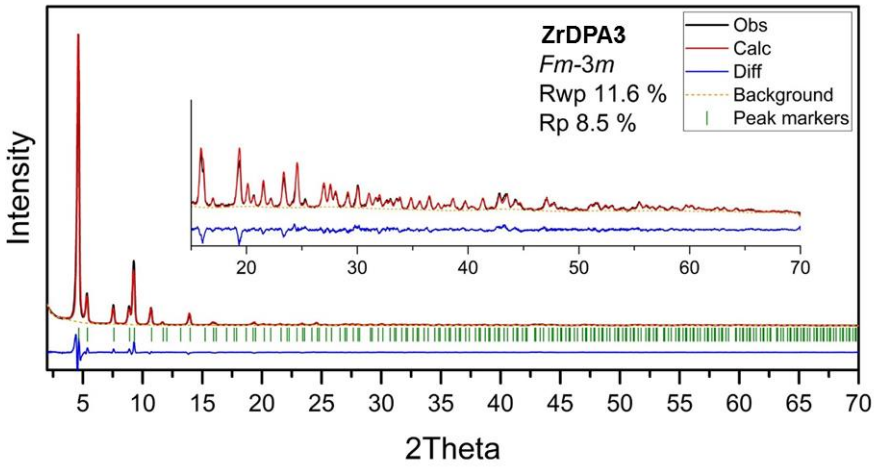

Figure 26. Rietveld fits of X-ray data for ZrDPA3.

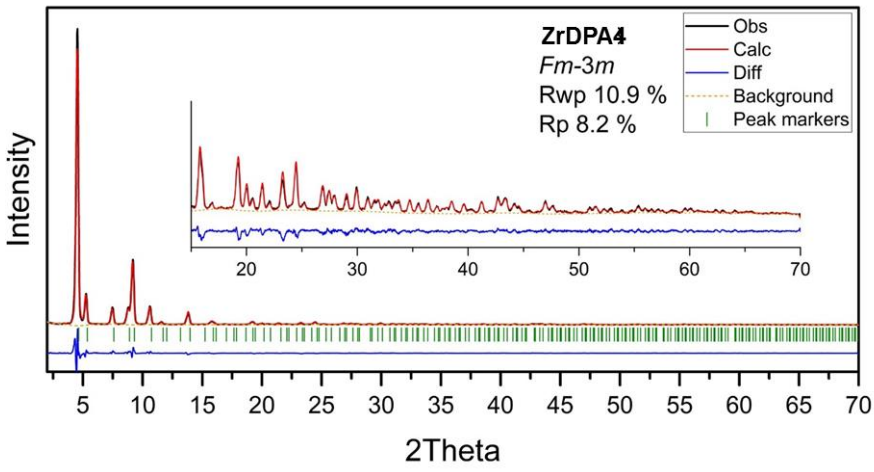

Figure 27. Rietveld fits of X-ray data for ZrDPA4.

Table 8. Crystallographic data for the PXRD Rietveld refinement of ZrDPAX MOFs.

Identification code	**ZrDPA1**	**ZrDPA2**	**ZrDPA3**	**ZrDPA4**
Empirical formula	$C_{3.5}H_2O_{0.67}Zr_{0.125}$	$C_{3.5}H_2O_{0.67}Zr_{0.125}$	$C_{3.5}H_2O_{0.67}Zr_{0.125}$	$C_{3.5}H_2O_{0.67}Zr_{0.125}$
Formula weight	66.12	66.12	66.12	66.12
Temperature/K	N/A	N/A	N/A	N/A
Crystal system	cubic	cubic	cubic	cubic
Space group	*Fm*-3*m*	*Fm*-3*m*	*Fm*-3*m*	*Fm*-3*m*
a=b=c/Å	32.915	32.909	32.870	32.894
Volume/$Å^3$	35659.07	35639.90	35514.01	35593.23
Z	192	192	192	192
$\rho_{calc}g/cm^3$	0.59119	0.59151	0.59361	0.59229
Rp	7.4 %	7.1 %	8.5 %	8.2 %

Rwp	9.4 %	9.2 %	11.6 %	10.9 %

7.1.7. References

[1] Laurier, K. G. M., Vermoortele, F., Ameloot, R., De Vos, D. E., Hofkens, J. and Roeffaers, M. B. J.; J. Am. Chem. Soc., **2013**, *135*, 14488 – 14491.

[2] Comito, R. J., Fritzsching, K. J., Sundell, B. J., Schmidt-Rohr, K. and Dincă, M.; J. Am. Chem. Soc., **2016**, *138*, 10232 – 10237.

[3] Amador, R. N., Carboni, M. and Meyer, D.; Materials Letters, **2016**, *166*, 327 – 338.

[4] Zhang, T. and Lin, W.; Chem. Soc. Rev., **2014**, *43*, 5982 – 5993.

[5] Hu, Z., Deibert, B. J. and Li, J.; Chem. Soc. Rev., **2014**, *43*, 5815 – 5840.

[6] Lustig, W. P., Mukherjee, S., Rudd, N. D., Desai, A. V., Li, J. and Ghosh, S. K.; Chem. Soc. Rev., **2017**, *46*, 3242 – 3285.

[7] Stassen, I., Burtch, N., Talin, A., Falcaro, P., Allendorf, M. and Ameloot, R.; Chem. Soc. Rev., **2017**, *46*, 3185 - 3241.

[8] Lu K., He, C., Guo, N., Chan, C., Ni, K., Lan, G., Tang, H., Pelizzari, C., Fu, Y.-X., Spiotto, M. T., Weichselbaum, R. R. and Lin, W.; Nature Biomedical Engineering, **2018**, *2*, 600 – 610.

[9] Ni, K., Aung, T., Li, S., Fatuzzo, N., Liang, X. And Lin, W.; Chem, 2019, *5*, 1892 – 1913.

[10] Wang, C., Volotskova, O., Lu, K., Ahmad, M., Sun, C., Xing, L. and Lin, W.; J. Am. Chem. Soc., **2014**, *136*, 6171 – 6174.

[11] Perry IV, J. J., Feng, P. L., Meek, S.T., Leong, K., Dotya, F. P. and Allendorf, M. D.; J. Mater. Chem., **2012**, *22*, 10235 – 10248.

[12] Dujardin, C., Auffray, E., Bourret-Courchesne, E., Dorenbos, P., Lecoq, P., Nikl, M., Vasil'ev, A. N., Yoshikawa, A. and Zhu, R.-Y.; IEEE TRANSACTIONS ON NUCLEAR SCIENCE, **2018**, *65*, 1977 – 1997.

[13] Lecoq, P.; Nuclear Instruments and Methods in Physics Research A, **2016**, *809*, 130 – 139.

[14] Hajagos, T. J., Liu, C., Cherepy, N. J. and Pei, Q.; Adv.Mater., **2018**, *30*, 1706956, 1 – 13.

[15] L. Cerrito, Radiation and Detectors, Graduate Texts in Physics, Chapter 9, Springer International Publishing AG **2017**.

[16] Doty, F. P., Bauer, C. A., Skulan, A. J., Grant, P. G. and Allendorf, M. D.; Advanced Materials, **2009**, *21*, 95 - 101.

[17] Tsuruoka, T., Furukawa, S., Takashima, Y., Yoshida, K., Isoda, S. and Kitagawa, S.; Angew. Chem. Int. Ed., **2009**, *48*, 4739 – 4743.

[18] Schaate, A., Roy, P., Godt, A., Lippke, J., Waltz, F., Wiebcke, M. and Behrens, P.; Chem. Eur. J., **2011**, *17*, 6643 – 6651.

[19] Yuan, S., Qin, J.-S., Lollar, C. T. and Zhou, H.-C.; ACS Cent. Sci., **2018**, *4*, 440 – 450.

[20]Valenzano, L., Civalleri, B., Chavan, S., Bordiga, S., Nilsen, M. H., Jakobsen, S., Lillerud, K. P. and Lamberti, C.; Chem. Mater., **2011**, *23 (7)*, 1700 – 1718.